ADVERTIMENT. L'accés als continguts d'aquesta tesi doctoral i la seva utilització ha de respectar els drets de la persona autora. Pot ser utilitzada per a consulta o estudi personal, així com en activitats o materials d'investigació i docència en els termes establerts a l'art. 32 del Text Refós de la Llei de Propietat Intel·lectual (RDL 1/1996). Per altres utilitzacions es requereix l'autorització prèvia i expressa de la persona autora. En qualsevol cas, en la utilització dels seus continguts caldrà indicar de forma clara el nom i cognoms de la persona autora i el títol de la tesi doctoral. No s'autoritza la seva reproducció o altres formes d'explotació efectuades amb finalitats de lucre ni la seva comunicació pública des d'un lloc aliè al servei TDX. Tampoc s'autoritza la presentació del seu contingut en una finestra o marc aliè a TDX (framing). Aquesta reserva de drets afecta tant als continguts de la tesi com als seus resums i índexs.

ADVERTENCIA. El acceso a los contenidos de esta tesis doctoral y su utilización debe respetar los derechos de la persona autora. Puede ser utilizada para consulta o estudio personal, así como en actividades o materiales de investigación y docencia en los términos establecidos en el art. 32 del Texto Refundido de la Ley de Propiedad Intelectual (RDL 1/1996). Para otros usos se requiere la autorización previa y expresa de la persona autora. En cualquier caso, en la utilización de sus contenidos se deberá indicar de forma clara el nombre y apellidos de la persona autora y el título de la tesis doctoral. No se autoriza su reproducción u otras formas de explotación efectuadas con fines lucrativos ni su comunicación pública desde un sitio ajeno al servicio TDR. Tampoco se autoriza la presentación de su contenido en una ventana o marco ajeno a TDR (framing). Esta reserva de derechos afecta tanto al contenido de la tesis como a sus resúmenes e índices.

WARNING. Access to the contents of this doctoral thesis and its use must respect the rights of the author. It can be used for reference or private study, as well as research and learning activities or materials in the terms established by the 32nd article of the Spanish Consolidated Copyright Act (RDL 1/1996). Express and previous authorization of the author is required for any other uses. In any case, when using its content, full name of the author and title of the thesis must be clearly indicated. Reproduction or other forms of for profit use or public communication from outside TDX service is not allowed. Presentation of its content in a window or frame external to TDX (framing) is not authorized either. These rights affect both the content of the thesis and its abstracts and indexes.

Control of Optical Fields and Single Photon Emitters by Advanced Nanoantenna Structures

Lars Neumann

ICFO - Institut de Ciències Fotòniques
Barcelona 2012

Control of Optical Fields and Single Photon Emitters by Advanced Nanoantenna Structures

Lars Neumann

Thesis Director: Niek F. van Hulst

Submitted in partial fulfillment
of the requirements for the degree of

Doctor

by the

Universitat Politècnica de Catalunya
Barcelona 2012

Abstract

A central topic in science and technology is the exploration and exploitation of smaller and smaller systems by optical techniques. Often, the wavelength is dictated by the system of interest: Biological systems emit and absorb visible light, or photovoltaic devices convert from the solar spectrum. For a long time, the achievable optical resolution has seemed principally bound by the diffraction limit.

However, the advances in nanoscience and nanotechnology have led to the fabrication of structures with ever smaller feature sizes, such that the length scale of fabricable features has reached dimensions far below the wavelength of visible light.

Visible light interacts resonantly with metallic structures that have characteristic dimensions of around 100 nm. A strong resonant interaction of light with appropriately designed structures presents a manifold of new tools for the study of new optical phenomena in science and technology, for which the tight control of optical fields is a prerequisite. Plasmonic nanostructures strongly confine, enhance and thus control light on the nanometre scale.

This thesis centres around the precise control of optical fields on the nanoscale. An overview of near-field optics, its methods and challenges is presented in Chapter 1.

Nanotechnology relies largely on nanofabrication, which is a continuously developing topic. The feature size of under 100 nm required for optically resonant nanostructures is within the range of the resolution of state-of-the-art nanofabrication tools. The fabrication of such nanostructures using Focused Ion Beam technology is discussed in Chapter 2.

Optical antennas have proven to efficiently link free radiation to objects through localised fields. The object can be a single molecule, a non-linear medium or a semiconductor, depending on the purpose of the device. With increasing complexity of optical antennas the need arises to precisely investigate and control their modal local field distribution. In Chapter 3, I present the investigation of local antenna fields by deterministic control of a nanometric fluorescent bead as the local field probe. The bead accurately maps the optical modes of an antenna, for the first time optically resolving modal features of 35 nm FWHM. Moreover, the antenna resonance is revealed.

A critical point in the interaction of light with matter is the matching of the impedance of all components involved in the interaction. Chapter 4 demonstrates how intrinsically very different structures, a tapered waveguide and a sub-wavelength aperture, are impedance-matched at the wavelength of operation to improve the transmission of the aperture.

Near-field Scanning Optical Microscopy is a standard tool to image a variety of samples with nanometric resolution. The low transmissivity of conventional probes with sub-wavelength apertures imposes a strong limitation to its popularity. As reported in Chapter 5, a redesign of the probe removes the lossy sub-wavelength components and improves the feed to the aperture. The throughput increases by 100× and the damage threshold by 40×. As this increase in brightness allows to employ smaller apertures, single molecules are imaged with a true optical resolution of as good as 60 nm FWHM. No fitting algorithms are required.

The results presented in this thesis show that localised fields and therefore the functioning of nanostructures such as optical antennas can be precisely assessed by a mapping with fluorescent nanosources. The mapping provides a flexible tool to tune the nanostructures and increase the level of control exerted on optical fields. In reverse, an optimised nanostructure will efficiently control single emitters in its vicinity. Benefiting applications include: high resolution imaging, high sensitivity sensing and photo detection, photovoltaics and non-linear optics.

Contents

1 An Introduction to Control of Light Through Nanostructures

For a long time, the spatial control of light seemed principally by the diffraction limit. The interaction of light with matter, a central topic in optics, could only be addressed with a resolution close to half the wavelength of light. Many systems of interest, for example in biology, however exhibit features much smaller. The advance of nanoscience and nanotechnology has enabled the fabrication of nanostructures shorter than the wavelength of light. An important class of nanostructures are optical antennas. Optical fields localised by such optical antennas have proven to be highly confined and enhanced, effectively breaking the diffraction limit and providing a new tool to control light on the nanoscale.

This introduction to control of light through nanostructures begins with the motivation of near-field optics in the first section. General concepts of the interaction of radiation and nanostructures, the topic of this PhD thesis, will be elucidated in the second section, with a focus on optical antennas. The third section introduces to the near-field microscope and the chapter closes with an outline of the thesis.

1.1 Why the Optical Near-Field?

In nanoscience and nanotechnology, a central topic is the exploration and exploitation of ever smaller systems by optical techniques. When the size of a system becomes comparable to the wavelength of the light interacting with the system, the *diffraction limit* enters the picture as a fundamental boundary [1, 2]. The spatial control of light is fundamentally constrained at length scales equal to roughly half its wavelength. This constraint sets the limit for example to the optical resolution of a standard microscope.

Often, the wavelength of operation is dictated by the system of interest. Biological systems emit and absorb visible light; photosynthesis uses visible light for chemical processes; photovoltaic devices convert from the solar spectrum; our vision relies on visible light. Here, a change to shorter wavelengths is not an option to control light on smaller scales.

The optical near-field contains the spatial information with wavevectors larger than those for propagating waves, therefore beyond the diffraction limit [3]. As an evanescent field, it is bound to some type of interface and decays within about 30 nm. Optical near-fields are tightly connect to nanostructures that provide the necessary interface. The spatial extent of the near-field is determined by the physical features and material of the nanostructure and the wavelength of operation. The spatial control of the field is a parameter of the nanostructure, not a fundamental limit. Therefore, the control of optical fields through nanostructures is an opportunity to extend optical techniques to the exploration and exploitation of smaller and smaller systems.

The fabrication of nanostructures goes hand in hand with the investigation of the associated near-fields. The central question of this thesis is the design and investigation of nanostructures suitable to control light.

1.2 Nanostructures and the Near-Field

The first artificial nanostructure used to shape optical radiation was a simply a sub-wavelength aperture. Even though offering only a very low transmissivity [4], sub-wavelength apertures build the foundation of Near-Field Scanning Optical Microscopy (NSOM) [5,6]. NSOM has been the first experimental method to image, create and control optical fields on length scales of 60 nm to 100 nm [7].

The Fabrication of Nanostructures. The real challenge in the realisation of such nanostructures has been and still is their characteristic size of well below 100 nm. For example, the resonant optical dipole antennas presented

later in Chapter 3 have dimensions of 170 nm in length, 65 nm in width and 50 nm in height. The required precision is at the order of 10 nm.

Today, nanotechnology allows to precisely design and structure with an accuracy of 10 to 30 nm. Complex nanostructures, carefully dimensioned with respect to the wavelength of the incident radiation, capitalise on internal, geometrical resonances that couple resonantly and efficiently to external visible radiation. The respective dimensions, at which the resonance occurs, depend on the exact shape, material composition and local environment of the structure. As metals are imperfect electrical conductors for optical frequencies, the first order resonance does not occur at a length equal exactly half of the free space wavelength, but at an effective length a factor two to five shorter [8]. Therefore, for materials commonly used in optics like silver, gold or aluminium, typical dimensions of resonant structures are below 100 nm.

While the apertures used as near-field sources in NSOM had no sophisticated relation to the wavelength of the light transmitted other than being smaller, today's precise fabrication of nanostructures allows to match their dimensions to optical resonances. As a consequence, the interaction of light with matter becomes strongly enhanced, and the properties of optical fields can be controlled on a much higher level than previously possible.

Optical Antennas. Nanostructures designed to improve the interaction between a nanoscopic object and light are generally termed *optical antennas*. They are designed to interact resonantly with light of a specific wavelength, strongly enhancing the interaction. Analogous to their radio frequency counterparts, optical antennas link freely propagating radiation to nanoscopic objects through localised fields. Depending on the actual geometry of the antenna, the localised energy can be confined to extremely small volumes. The incident energy absorbed by the antenna is squeezed into the confined volume, such that this field becomes strongly enhanced.

A nanoscopic object placed in close proximity to the antenna interacts with the antenna and the strongly enhanced local field. The nanoscopic object may encompass, among others, single atoms or molecules, quantum dots, or complex nanostructures and circuits [9, 10].

An optical antenna operates as a bidirectional transducer. Through near-field coupling, it connects nanoscopic emitters to freely propagating radiation, and vice versa it connects freely propagation radiation to nanoscopic absorbers. As efficient transducer, optical antennas have a wide range of applications.

Applications of Optical Antennas. Antennas have applications wherever an efficient link between nanoscopic objects and propagating light is required.

As a photo detector, an optical antenna strongly localises and enhances the impinging optical radiation. This allows a reduction in the size of the detector which improves the signal-to-noise ratio and the readout speed [11–13]. Equally in photovoltaics, the localisation may improve the carrier separation and reduce the cost as less expensive semi-conducting material is required [14, 15].

Non-linear processes benefit from the high field intensities that result from the strong field localisation at an optical antenna. Also, some metals offer high intrinsic non-linearities, e.g. gold and aluminium. Second [16,17] and higher [18] harmonic generation, four-wave-mixing [19] and two-photon photoluminescence [20–22] have been demonstrated.

A strongly localised field is accompanied by an equally strong field gradient, which is a prerequisite for optical trapping of nanoscale particles [23, 24].

The last application to be mentioned here is the most relevant one in the context of this thesis. Optical antennas allow the study of single and / or weak emitters that otherwise could not be observed [25] or spatially discriminated [26]. An emitter placed in the very vicinity of the optical antenna can couple very strongly to the antenna modes. As the antenna is a transducer between this localised field and free radiation, the antenna links the emitter to free radiation [27–30]. The efficiency of this process is the critical benchmark for every optical antenna.

For a more detailed view on applications of optical antennas, the reader may be referred to several reviews that have been published recently [31–35].

The Design of Optical Antennas. To this point, an optical antenna has been introduced as an abstract device to convert free radiation to a localised field and vice versa. There is no restriction on the shape of the device, as long as it operates in an efficient manner. A wealth of classical, radio-frequency designs and their radiative properties is well known. Many have been adapted to an operation at optical wavelengths.

Among these are monopole antennas [26, 36, 37], dipole antennas [38], Yagi-Uda antennas [29,39,40], gap antennas [38,41], fractional antennas [42, 43], triangular antennas [25], bow tie antennas [22,44–47], particle antennas [48, 49], bull's eye antennas [50], slot antennas [51–53], cross antennas [54] and devices localising through sharp needles [55–57]. Recently, some effort has been invested in more complex devices as three-dimensional, stacked

antennas [58, 59], loaded antennas [60], antennas coupled to transmission lines [61–63] and feeding elements [64].

All optical antennas listed have their specific properties, and may differ in excitation and emission rates, directivity, field enhancement and confinement, and bandwidth of operation.

Coupled Nanostructures. So far, only optical antennas have been taken in consideration. While optical antennas are transducers between nanoscopic objects and light, other nanostructures may serve different purposes.

Two or more arbitrary nanostructures can interact through near-field coupling when placed sufficiently close to each other. Simple examples include the hybridisation of the energy levels of two coupled, identical rods [65], layered nanoshells [66] or extended chains [67].

For the former, the two rods still resemble an optical antenna; an example of how completely different nanostructures can be coupled will be presented in Chapter 4 where an aperture is linked to a tapered waveguide and the transmission resonantly enhanced. Instead of free radiation, now a guided waveguide mode provides the radiation. The waveguide is partially tapered and eventually brings the guided mode close to its cut-off. Here, the mode transforms into an evanescent mode that couples in the near-field efficiently to the aperture.

A sophisticated arrangement of equal and arbitrary nanostructures allows to control various properties of light.

Open Questions. Though the resemblance to well-known radio-frequency antennas is very apparent, a number of important differences arise at an operation of optical antennas and nanostructures in general at optical frequencies, and remain subject to ongoing investigation.

The scaling between wavelength and dimensions of a nanostructure is linear only at radio-frequencies where metals behave as perfect conductors. At optical frequencies, this scaling behaviour breaks down, and an antenna responds to an effective wavelength that is different by as much as a factor 5 from the wavelength of the incident radiation [8].

Also, while radio-frequency antennas are usually driven through a transmission line connected to some electrical circuit, optical antennas are orders of magnitude smaller and operate at much higher frequencies. The fabrication challenge complicates enormously with the small size, and the accurate, reproducible and cost-effective fabrication of an optical antenna with an interfaced source or receiver is a task hardly possible for today's nanofabrication tools.

The efficiency of the coupling process between an antenna, an object or

two arbitrary nanostructures depends greatly on how well the impedances of the interacting components are matched [9, 31, 35, 68, 69]. For an optical antenna and a single molecule, the respective impedances of roughly 1 MΩ and 3 Ω differ largely [31]. In contrast, the impedances of the tapered waveguide and the aperture can be matched easily as will be seen in Chapter 4.

1.3 Recording the Optical Near-Field

The optical near-field is an evanescent field and as such it decays typically within 30 nm. As a consequence, the local field of e.g. an optical antenna must be recorded within nanometres above its surface. Also, as the characteristic lateral dimensions of optical antennas and other nanostructures are well below the wavelength of visible light, the thorough spatial probing and analysis of optical phenomena is a difficult task.

In this section, I will very briefly introduce near-field microscopy and the near-field set-up. The experiments reported in the experimental chapters were performed on such a set-up, however the precise configuration will be the subject of each of the experimental Chapters 3, 4 and 5 individually.

A sketch of the near-field microscope is presented in Figure 1.1. The very base of such a set-up is a confocal microscope that is encircled in the Figure by a dashed box. The confocal part of the set-up includes two avalanche photodetectors (APD) that map orthogonal polarisations of an impinging optical field.

The difference to a purely confocal microscope lies in additional components above the confocal part the microscope (dotted box). The scanning tip or fibre has to be within nanometres of molecules, beads or a second nanostructure in order to interact in the near-field. A piezo allows to position the scanning tip or fibre with respect to a sample plane and a shear-force feedback mechanism actively controls the vertical position of the scanning tip or fibre with nanometric accuracy. Details on shear-force can be found in [70, 71].

This near-field set-up has five free axis: the sample plane with the molecules or beads can be positioned in three axes, and the scanning tip or fibre in the two lateral axes. The third axis of the piezoelectric scanner for the scanning-tip or fibre is reserved for the shear-force feedback.

As modi of operation, the excitation can either be performed confocally through the objective or in a true NSOM configuration through the fibre. In both cases, the detection path remains the same. The former mode of excitation was employed in the experiments presented in Chapter 3 and the latter in Chapters 4 and 5.

As mentioned before, the exact configuration of the near-field set-up will

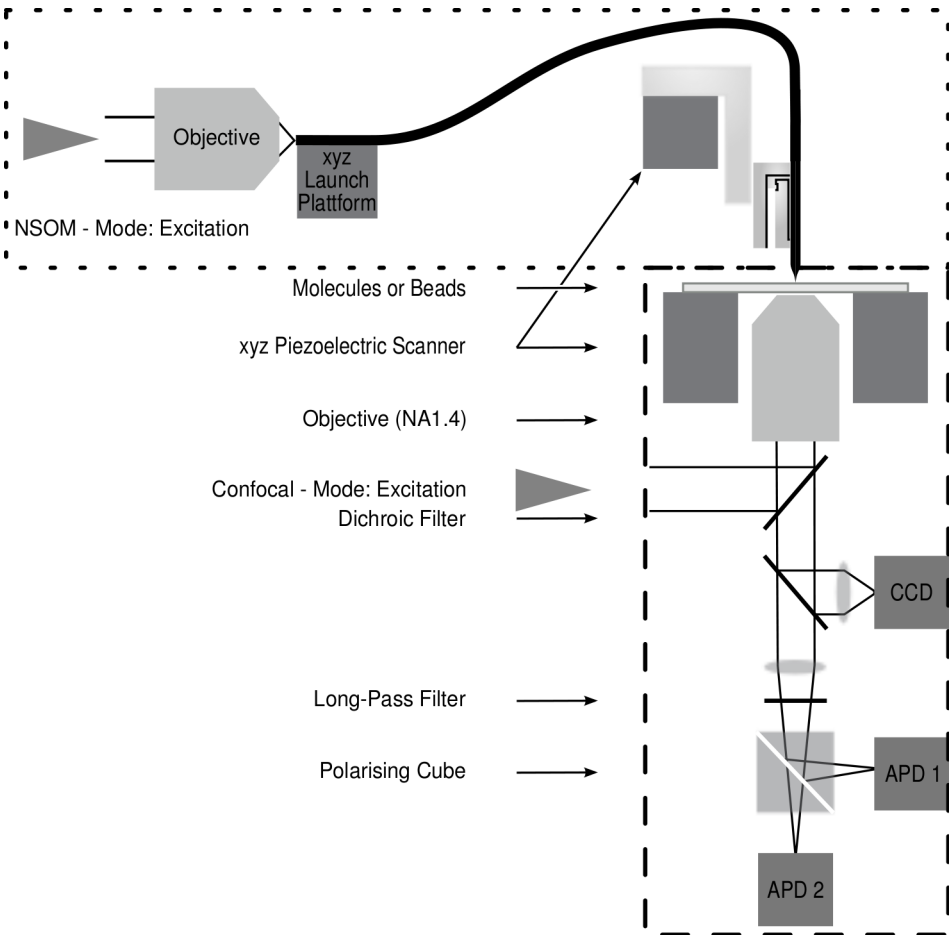

Figure 1.1: **Scanning Near-Field Optical Microscope (NSOM).** Our microscope builds on a standard confocal set-up (dashed box). A scanning tip or fibre is attached to an additional piezoelectric scanner above the confocal set-up (dotted box). A feedback mechanism allows to approach the scanning tip or fibre to the molecules or beads such that near-field interaction is possible. The signal is mapped polarisation-resolved on two different Avalanche Photodetectors (APD).

be detailed in each experimental Chapter individually. For more information on near-field scanning optical microscopy in general, the reader may be referred to [72–74].

1.4 Outline of the Thesis

Chapter 2 is dedicated to the fabrication of nanostructures that will be experimentally analysed in the subsequent chapters. As mentioned before, the characteristic length scale of nanostructures of interest is below 100 nm, which is possible though challenging with standard nanofabrication tools. The chapter focuses on steps taken to reliably and reproducibly reach this accuracy.

In the first experimental chapter of this thesis, Chapter 3, maps of the mode profile of optical antennas are presented. The mode maps were extracted from the magnitude of the fluorescent signal of single beads that interact with the optical antenna through the near-field. The beads had a diameter of only 20 nm. Plasmonic features of with a FWHM of 35 nm are revealed.

In Chapter 4, we report on the impedance matching of a single subwavelength aperture and a tapered waveguide. When the impedances are matched, a peak in transmission is observed.

Single molecules are imaged in an NSOM configuration in the very last Chapter 5. Sophisticated nanostructuring of the probe has resulted in an increased throughput and a higher damage threshold than present in conventional NSOM probes, permitting to move to smaller aperture sizes.

2 Fabricating Optical Antennas and Other Nanostructures

The control of optical fields requires the fabrication of structures with dimensions well shorter than the wavelength of light. Nanostructures like optical antennas with characteristic dimensions below 100 nm must be fabricated in an accurate and reproducible way, such that meaningful optical experiments can be performed. The precise fabrication is a challenge also to the latest equipments in nanotechnology. A Focused Ion Beam (FIB) system in combination with a lithography system allows the dedicated fabrication of arbitrary nanostructures with a tolerance of only 10 to 30 nm. This fabrication approach fullfils all demands to accuracy, reproducibility and effectivity.

In this chapter, the concepts and tools of nanofabrication will introduced and discussed in view of the nanostructures required for the optical experiments. Concepts of nanofabrication and methods are discussed in the first section. The next section focuses on the fabrication steps and considerations taken before proceeding to the fabrication with the Focused Ion Beam (FIB) system. The last two sections discuss FIB milling and lithography and include a discussion of important parameters.

2.1 An Introduction to Nanofabrication

The aim of nanofabrication is the preparation of dedicated structures with typical dimensions of below 100 nm. In the context of this thesis, 'dedicated structures' means *optical antennas* in Chapter 3, *sub-wavelength apertures coupled to tapered waveguides* in Chapter 4, and *modified probes for Near-Field Scanning Optical Microscopy* in Chapter 5.

The Nanostructures of this Thesis. The scope of this thesis is the control of optical fields through advanced nanostructures. Therefore, all nanostructures must be small with respect to the wavelength of visible light.

The optical antennas of Chapter 3 show a resonance at a length of 170 nm. The width of such a structure is about 65 nm at the base. For reasons explained in that chapter, the antenna is to be fabricated on the end face of a scanning tip. The end face of this tip is only about 500 to 900 nm in diameter wide. The topic of Chapter 4 is a resonant coupling between a tapered waveguide and a sub-wavelength aperture. The technical realisation is a tapered and cut fibre waveguide, with the aperture milled into the end face of the waveguide. As an error in diameter of the tapered waveguide causes a shift in the resonant wavelength, high accuracy is required. Chapter 5 demands the fabrication of a similar structure, however with an aperture size of as small as 40 nm.

Summarising the requirements to the nanostructures, apertures and antennas of at most 40 to 60 nm in extent in the smallest dimension must be fabricated within the scope of this thesis. The features must not be fabricated on a flat cover slip, but at the end face of a scanning tip or a tapered optical fibre. As the dependence of the optical signal on certain physical dimensions of the nanostructure is of interest, a precise and reproducible fabrication is a precondition.

Nanofabrication Technologies. Advances in nanofabrication have only recently allowed to progress into the nanoscale regime and fabricate sophisticated nanostructures for applications in science and technology.

The tools for nanofabrication encompass a wide range of technologies [75, 76]. In a scientific environment, the most widely used technologies include Electron Beam Lithography (EBL) and Focused Ion Beam Lithography (FIBL). These two technologies follow the so-called top-down approach, where the nanostructure evolves from a structural layer. Self-assembly is a popular bottom-up method where nanoparticles self-organise on a surface to form complex patterns [48, 49, 77, 78]. However, the level of control on the process is far lower than for top-down methods. This is a significant drawback to self-organisation. Electron Beam Lithography

(EBL) is widely used to write large arrays of nanostructures. EBL may reach a resolution of better than 10 nm [79]. Focused Ion Beam Lithography (FIBL) is a comparably slow method and therefore mostly used for prototyping applications. Since no lift-off as for EBL is required, FIBL can applied in all sample geometries.

The choice of a suitable nanofabrication method is determined by the chemical composition and geometry of the initial structural layer and the desired properties of the later nanostructure. As it is virtually impossible to apply a resist on the small surface at the end face of the scanning tip or fibre, EBL can be safely ruled out. FIB milling combines high resolution with the absence of any type of mechanical contact. In the past, FIB milling has proven a reliable and powerful mean of nanostructuring on and of complex surfaces. Examples include probe fabrication for aperture Near-Field Scanning Optical Microscopy (NSOM) [80,81], nanometric light sources [55, 82] and optical antennas [27, 37].

Within the scope of this thesis, all nanostructures are fabricated using a Focused Ion Beam system with an attached lithography system. The practical resolution of the combined system is around 10 to 30 nm. The lithography provides the accuracy and reproducibility required to fabricate the desired nanostructures on the end face of a scanning tip or fibre.

2.2 Prior to Focused Ion Beam Lithography

As mentioned in the previous section, the optical antennas or the subwavelength apertures must be fabricated in the end face of a flat scanning tip or fibre. In this section, I describe the steps taken to prepare the scanning tip or fibre and the structural layer prior to the application of Focused Ion Beam Lithography (FIBL). These steps include the tapering of the scanning tip or fibre and the deposition of the structural and other metallic layers. As the choice of the deposited materials determines the optical properties of the nanostructure and impacts the application of FIBL, a discussion on materials is part of this section.

Tapering by Heat-Pulling

All experiments in this thesis require a sharp scanning tip or fibre. The sharpness is a result of heat-pulling an optical fibre. It may be remarked here, that the experiments presented in Chapters 4 and 5 require tapered optical fibres as the base of the fabrication. The scanning tips used for the research in Chapter 3 are also made from optical fibre material. However, as they will not need to guide light, they are cut at a length of 2 cm and will thus be denoted as scanning tips.

The fibre material used is a single-mode optical fibre designed for a wavelength of 633 nm. Their diameter of 125 μm is three to five orders of magnitude larger than the features of interest at the nanoscale. In the very first step of the fabrication we match these two lengths scales by tapering the optical fibre. The two techniques used to fabricate a taper region are chemical etching [83–85] and mechanical heat-pulling [85–87]. In this thesis, the latter technique has been employed as the technical equipment was already available on premises. The pulling process is extremely sensitive to fluctuations of room temperature, humidity or changes in the handling of the fibre, such that the reproducibility is low.

Thin Layer Desposition

In the context of this thesis, the deposition of a metal on the scanning tip or fibre serves three different purposes:

- To establish sufficient conductivity for high-resolution electron microscopy or focussed ion beam applications.
- To improve the adhesion of a second material on a substrate.
- To deposit the structural layer.

Sufficient conductivity is enusured by the deposition of a layer of Titanium of typically 10-15nm in thickness.

Adhesion is important because most experiments presented in Chapters 3 to 5 involve scanning a nanostructure across a surface. The scanning exercises high friction on the nanostructure. If the structure is less strongly attached, it may easily become damaged or even detach. Poor adhesion may be a result of the low reactivity of noble metals, mismatches in the crystalline structures, surface cleanliness or the evaporation process itself [88]. A good adhesion of the nanostructure's material is essential to the success of the later experiment. It is achieved by depositing a thin adhesion layer of a few nanometres in thickness before the structural layer. Typical adhesion materials include chromium and titanium. In our evaporator, titanium has lead to better results and will be used throughout this thesis. It may be noted here briefly that the adhesion layer often induces less desirable optical properties, expressed through its refractive index and absorption [89, 90].

The structural layer is deposited last and is discussed in the next section.

A Consideration on Materials for the Structural Layer

The structural layer is the starting point in the fabrication of e.g. an optical antenna or a sub-wavelength aperture. Usually, the proposed experiment

determines the parameters such as the choice of material or film thickness. However, the fabrication of the structural layer is also subject to the available deposition systems and methods. The choice of a specific structural layer must be seen as a compromise between the required optical properties and the characteristics of the fabrication process.

The materials most widely used for plasmonic applications are gold and aluminium [21, 91]. Silver is very plasmonic material as well, but its rapid oxidation is problematic [92]. Also other materials have been investigated, such as copper [91], nickel [93], oxides and nitrides [94] or semiconductors [95]. However, their plasmonic properties are less pronounced. Graphene is another plasmonic material. However, the effective wavelength of plasmons on graphene is extremely short at optical wavelengths [96].

In the visible, gold and aluminium are the materials of choice. Aluminium has a smaller penetration depth than gold. This allows to confine light to smaller volumes. Gold is chosen more often for applications in the red or infrared, while aluminium is better at shorter wavelengths. However, there is a spectral overlap between both materials that leaves space to consider fabricational arguments as well.

Gold and aluminium behave very differently during the deposition of the structural layer and processing in an FIB system. On our deposition equipment, gold films are generally smoother than aluminium films. Aluminium tends to form large grains. This is especially problematic on the end face of scanning tips or fibres, where grains feel the presence of the rim of the face. As Section 2.4 will show, gold is easier to process in the FIB system than aluminium. It is softer, so lower doses and shorter exposure times are sufficient. The grains are less pronounced, so sputtering occurs more homogeneously.

Aluminium has been choosen as the material for the optical antennas presented in Chapter 3 for several reasons. First, the harder aluminium is expected to withstand the friction experienced during the near-field scanning better. Second, the antenna length corresponding to same-order resonances is slightly longer than for gold. This simplifies a precise sweep through different lengths in the fabrication. Third, its smaller penetration depth confines the local fields better and permits to test the resolution of the proposed experiment. The waveguides in Chapters 4 and 5 are coated with aluminium. Aluminium prevents light leakage most effectively due to its smaller penetration depth. On the end facet, a smooth gold film is beneficial for milling very small and well-positioned sub-wavelength apertures.

2.3 Fabricating Nanostructures by Focussed Ion Beam Milling

A Focused Ion Beam (FIB) system is a tool to structure a surface with nanometre resolution. This section establishes a technical understanding of an FIB system and introduces the system on which most of the nanofabrication presented in this thesis was pursued. Any fabricated nanostructure must be visualised at some point. A discussion of the detectors of this FIB system explains the imaging process and points out the challenges in image interpretation.

Operation Principles and Limitations

Nowadays, Focussed Ion Beam (FIB) systems are very versatile though still complex tools in nano-machining. In this section, I will constrain myself to the aspects relevant to applications presented in this thesis. For more details, the reader may be referred to the extensive literature, e.g. [97, 98].

A Focused Ion Beam (FIB) system employs a strongly focussed beam of ions, usually gallium, to mill a sample with nanometric precision. Ion beams operate similarly to electron beams in SEMs. However, irradiation of a surface with ions and electrons has very different effects. First, ions are almost five orders of magnitude heavier than electrons. With a typical acceleration energy of 30 keV, ions gain a much higher momentum that is transferred to atoms on the surface on impact. Second, ions have a larger effective cross section which increases the interaction probability with atoms at the surface. At equal acceleration energy, ions interact at the sample surface, while electrons penetrate deeply into the sample.

While atoms at the sample surface only scatter electrons, they are sputtered by the gallium ions and rejected from the sample surface as either neutral atoms or secondary ions. Thus FIB milling is inevitably a destructive method.

Modern FIB systems incorporate both an electron source and an ion source in separate beam columns. This permits to sputter material with the ion beam while simultaneously imaging the progress with the electron beam.

Ions and electrons are particles carrying a charge. The charging of the scanning tip or fibre during imaging or sputtering is an critical factor for SEMs and FIB systems. If a scanning tip or fibre is little conductive and charges build up, the beams are distorted and repelled from the tip. This can drastically reduce the achievable resolution and induce drift and artefacts. Operating both beams simultaneously can neutralise the charging to some extent. However, now the beams themselves may interact.

The fabrication of structures of optically relevant dimensions means to bring also currently available FIB systems to their limits. Desired feature sizes reach to some tens of nanometres. Any charging of the sample distorts the beam sufficiently to render this impossible. Mechanical or electrical instabilities of the beam or the mount have a similar effect. The inevitable surface damage caused by an ion beam, e.g. during focusing of the ion beam, becomes very relevant when considering a typical thickness of the structural layer of only 30 to 100 nm. Even a rapid imaging scan with the ion beam with the purpose of orientation on the sample can lead to considerable damage. Also, gallium ions are implanted near the surface. Their impact on the optical properties is hard to determine, however most likely their presence increases dissipation.

The Available FIB System

Most of the work in this thesis was performed on a *Auriga Cross Beam* FIB system by *Zeiss*. This system has been designed specifically for the fabrication of plasmonic nanostructures in thin films, e.g. the optical antennas presented in Chapter 3. The SEM with Zeiss's *GEMINI* column may reach a resolution of better than 2 nm for an optimal sample. The focussed ion beam column *COBRA* is specified with ≤ 2.5 nm resolution and beam currents between 1 pA to 50 nA are available. Additional features include charge compensation and a gas injection system. On the software side, the unique feature is a dedicated lithography software, Fibics's *NanoPatterning and Visualization Engine* (NPVE). Nanofabrication with this lithography software is the topic of Section 2.4. The fabricated nanostructures can be imaged with three different detectors: an *Everhart-Thornley* Secondary Electron Detector and two *in-lense* detectors for secondary and back-scattered electrons. These detectors provide complementary information about the plasmonic structures with high accuracy.

Imaging with the Detectors

Any information about a nanostructure derives from signals captured by a single or several detectors of the FIB system. For the thorough interpretation of experimental data, it is essential to know the properties of the three different detectors.

Secondary electron (SE) detectors are very popular because of their signal strength and sensitivity to the topography of the sample. Secondary electrons originate in inelastic scattering events and possess lower energy than back-scattered electrons, thus contain only partial information. The BSED, or back-scattered, detector records high-energy electrons that are elastically

scattered by the sample. The scattering cross section depends strongly on the atomic species which permits chemical discrimination of a sample with very high resolution. Since the back-scattered signal is relatively weak, the BSED detector has an annular shape and is placed symmetrically around the electron beam.

The SE and the BSE detectors may be placed inside either the focusing optics of the SEM or on a side of the vacuum chamber. Detectors at the former, the *in-lens*, position collect the signal with a higher solid angle and have a higher resolution. As electrons have to cross the focusing optics twice to arrive at an *in-lens* detector, these detectors are prone to optical aberrations and charging.

Two conclusions are drawn for the imaging of nanostructures presented in this thesis. First, discrimination between materials is possible with the BSED detector only in the case of gold as the structural layer. The atomic number of gold differs sufficiently from that of the substrate, an optical fibre. This is unfortunately not the case for aluminium. Second, high resolution imaging of a scanning tip or fibre is very difficult. The optical antennas in chapter 3 are electrically isolated by removing the surrounding metal and in addition are located at the end of a microscopically large, dielectric support with a thin, only partially conductive layer, such that charging effects limit the resolution. The nanostructures in Chapters 4 and 5 suffer from this limitation as well, however to a lower degree.

2.4 Focussed Ion Beam Technology and Lithography

Even the use of the technologically most advanced Focused Ion Beam system is limited by the control software. A flexible and efficient software, able to provide access to all relevant parameters of the ion beam, is the key to the successful fabrication of plasmonic structures. Adding lithography hard- and software to an FIB system constitutes a very efficient system for nanofabrication.

This section introduces to *Focus Ion Beam Lithography* (FIBL) and shows its potential in a systematic study of parameters relevant to the quality of the nanostructures. The work flow of the fabrication of nanostructures concludes the section.

An Introduction To FIBL

Lithography is a transfer process that creates an image of a before defined pattern. Electron Beam Lithography (EBL) has been a very popular fabrication technique in nanofabrication. Its popularity has lead to the commercial availability of highly integrated scanning electron microscopes and

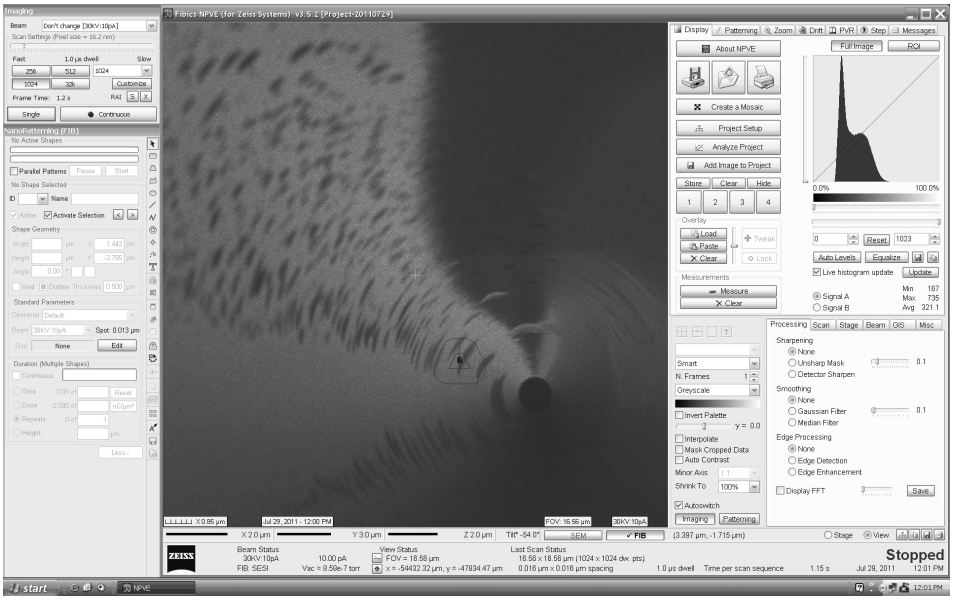

Figure 2.1: **Screenshot of the NPVE programme.** The black circle in the lower right of the visualisation panel shows the end face of a scanning tip or fibre, ready for lithographic milling.

lithography systems. This in turn has lead to the transfer of lithography technology to FIB systems, creating the field of *Focussed Ion Beam Lithography* (FIBL).

The lithography software on the available FIB system is the *NanoPatterning and Visualization Engine* (NPVE) by Canadian maker Fibics. Figure 2.1 shows a screenshot of the programme. The major advantages of this lithography programme are the very tight integration into the interface of the SEM, its simplicity for prototyping applications and its adaptation to FIB applications. The combination allows to easily and rapidly prototype new designs and to fabricate them accurately with the ion beam.

Due to the mass and momentum of the gallium ions, FIBL allows to write a pattern directly into a structural layer, without the need of a resist or similar. The consequence of this strong interaction of ions with the structural layer is that new parameters such as the exact shape of the scan path and re-deposition of removed material become very critical to the success of the milling. Therefore, a careful calibration of the lithography process is essential.

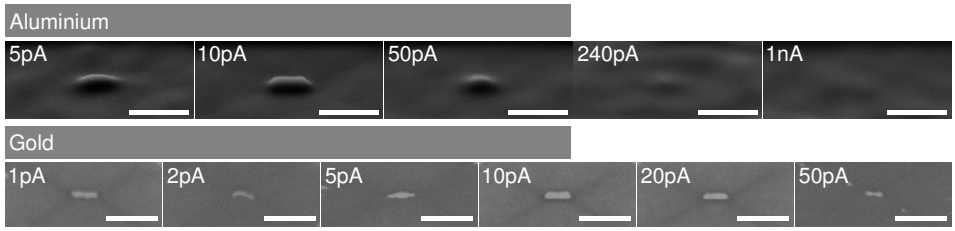

Figure 2.2: **The Beam Current.** Currents of 10 to 20 pA yield the most well-formed nanostructures for gold and aluminium. The images are taken with the SESI detector and the scale bars are 500 nm long.

Analysis of Milling Parameters

The lithography programme *NPVE* can control a variety of parameters of the ion beam in order to optimise the result of the milling process. These parameters can be sorted roughly into two practical categories. To the first category belong all parameters regarding the ion beam itself: the *beam current*, the *dose*, the *dwell time* and the *number of repeats*. The parameters in the second category determine the trajectory of the beam and affect the re-deposition. They include the *scan direction* and the use of *clean-up* layers.

In the first category, the *beam current* is chosen prior to the milling, because the focusing and correction of the astigmatism must be repeated after every change of current. The remaining parameters *dose*, *dwell time* and *number of repeats* constitute an over-determined system:

$$\text{beam current} \sim \frac{\text{dose}}{\text{dwell time} \times \text{number of repeats}} \tag{2.1}$$

The interaction with a particular structural layer obviously depends on its material composition and structure. The two most relevant materials in this thesis, gold and aluminium, show very distinct behaviour under the ion beam. Aluminium is very hard material that requires high doses to mill and that can withstand some imaging with the ion beam. Gold, on contrary, is extremely soft and virtually melts away when being imaged with the ion beam. The impact of most parameters is shown for both materials to adequately capture the implications of soft and hard materials. For all images shown in the following, the structural layers were deposited on a cover slip and had thicknesses for 60 nm for aluminium and 80 nm for gold.

Beam Current. A lithographic pattern is written at different beam currents and images taken with the secondary electron detector are shown in Figure 2.2. For each material, the beam dose and the dwell time are held constant, and the number of repeats is the variable adjusted to match the current.

Clearly visible is the existence of an optimal current of between 10 and 20 pA where the structures seem well-defined and possess sharp edges and corners. For doses higher and lower, the edges start to round and the structure appears fluffy, or vanishes all together. In the case of gold, the atoms re-organise and form bubbles along the structure that may change the shape of the structure completely. The two materials, the soft gold and the harder aluminium, show roughly the same optimal beam current for comparable layer thicknesses. The value of this optimal beam current seems less a material property, but rather a property of the ion beam.

The beam current is the number of ions interacting with the structural layer per unit time and area. It is equivalent to the exposure time it takes to write a pattern to the structural layer. For smaller beam currents, the exposure time must increase to compensate the for lesser current. A large exposure time, however, increases the likeliness of critical drift during the milling process. On the other hand, a higher beam current transfers more charges and more momentum per unit time to the structural layer. This may cause more problematic charging which perturbs the ion beam trajectory and shape, and second order effects may occur more frequently.

Technically, beam currents are selected by moving apertures with different radii into the beam. As the alignment of these apertures is not perfect to the nanoscale, each change of aperture requires to adjust focus and astigmatism to gain the highest beam quality again. Thus, it is not practical to find the optimal beam current for each structural layer again. In the following, 10 pA is the beam current of choice.

Beam Dose. The parameter beam dose sets the total charge that is irradiated on the structural layer per unit area. It must be chosen approximately proportional to the thickness of the structural layer. Since this thickness may vary due to variances in the evaporation process, the dose must be adjusted for each structural layer again.

A sweep through a range of beam doses is presented in Figure 2.3. The dwell time remains fixed and the number of repeats compensates the changing beam dose. A lower-than-optimal beam dose leaves the structural layer fully or partially intact, and the desired nanostructure is yet hardly visible. With increasing beam dose, the nanostructure slowly emerges from the structural layer. At some point, the surrounding parts of the structural

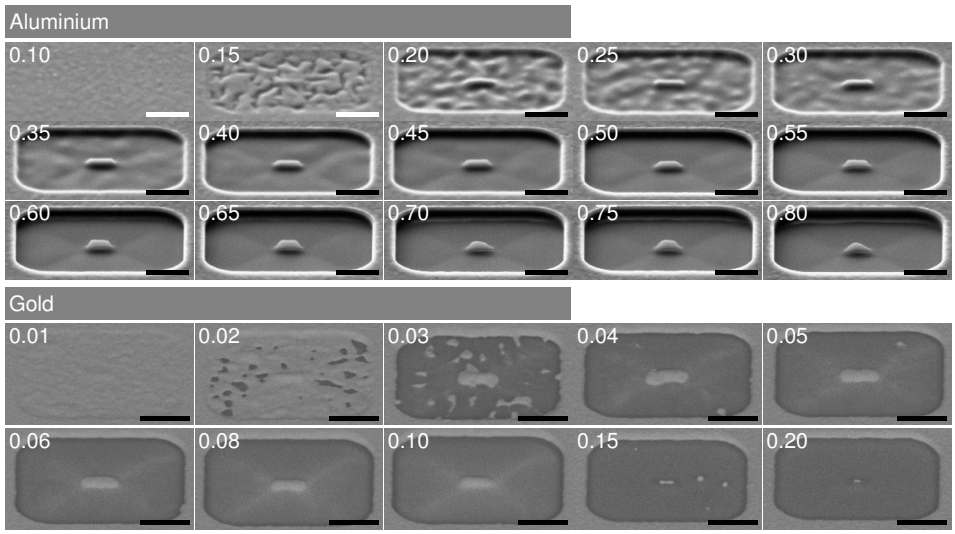

Figure 2.3: **The Beam Dose.** A sweep of the beam dose is essential to find the optimal dose for a given layer. The images for aluminium are taken with the SESI detector, and for gold with the BSED. The doses are given in nC / μm^2 and the scale bars are 500 nm long.

layer are fully removed and the beam starts to mill into the substrate. While this is in itself not a problem, the now dielectric surface insulates the nanostructure and causes stronger charging, which, together with second order effects, has a destabilising effect on the ion beam close to the surface. As a consequence, the nanostructure starts to shrink and eventually vanishes completely.

Thus, the optimal dose is the dose when the material surrounding the nanostructure is just fully removed. Though, the determination of this optimal dose may need experience. Even for very high doses, the nanostructure may still show in the SEM images as a topographic entity. However, second order effects have reduced it to merely a dielectric socket in the substrate than a metallic antenna.

Especially for aluminium this is problem because the sputtering rates for the metal and the substrate are comparable. The socket in the substrate may show the same signature in the SEM images as an isolated metallic nanostructure. In Figure 2.3, the optimal dose is 0.45 nC / μm^2. At the next lower dose, the surface of the substrate starts to exhibit some splotched, curved remains of the aluminium. The nanostructures milled with doses of 0.70 nC / μm^2 and higher seem to float above the surface. Here the dose was higher-than-necessary and sufficient glass substrate was

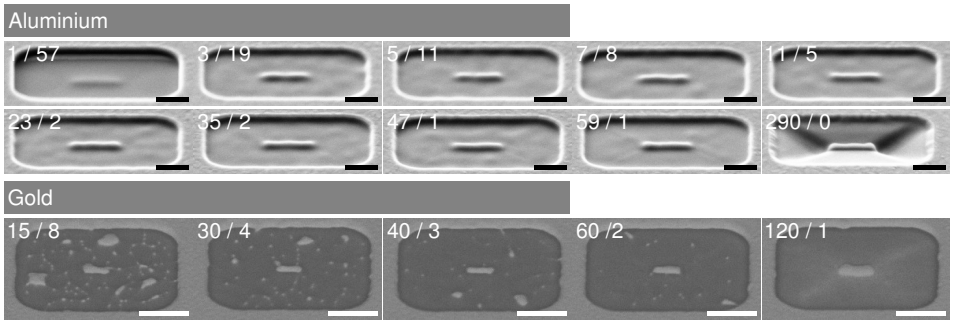

Figure 2.4: **The Dwell Time and the Number of Repeats.** The shape of the nanostructures depend more strongly for gold than for aluminium on the dwell time (before the slash, in microseconds) and the number of repeats (after the slash). The dose is held constant and the scale bars are 500 nm long.

removed such that the nanostructures stand on a glass socket appearing transparent to the electron beam.

For gold, the backscattered electron detector provides a material-sensitive signal which is stronger for gold than for the underlying substrate. At the optimal dose, the signal strength of the backscattered electron from the milled substrate has fully changed. In Figure 2.3 this happens between the doses of 0.03 and 0.05 nC / μm^2. Also the sputtering rate is much higher for gold than for the substrate. This allows to safely ascribe any topography to the metallic gold and not to a socket in the substrate.

Dwell Time and Number of Repeats. With the beam current and the beam dose set, the remaining two parameters of Equation 2.1 are the dwell time and the number of repeats. The dwell time is the period of time the ion beam spends on a single pixel. The number of repeats determines whether the pattern is written at once or repeated a number of times with an anti-proportionate dose.

Since the beam parameters are over-determined, the choice of the dwell time inevitably defines the number of repeats and vice versa. Mathematically speaking, the product of dwell time and number of repeats should be constant. A quick look at the numbers given in Figure 2.4 shows that this is only the case approximately. Rounding-errors of the lithography software cause this inaccuracy, which is especially visible for a dwell time of 290μs. It is important to re-assess during an FIB session whether the product of the displayed dwell time and number of repeats is constant. Otherwise, the milling behaviour might become erratic.

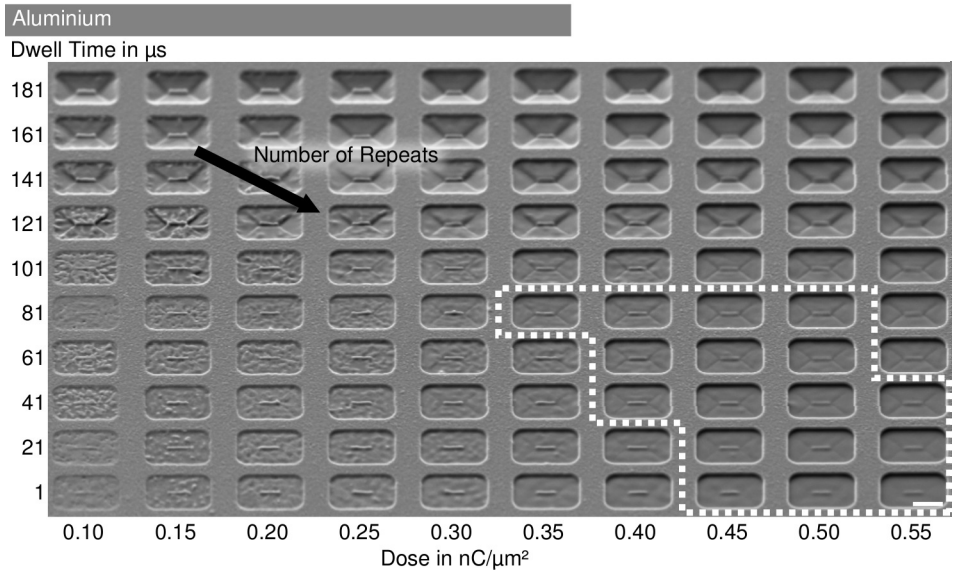

Figure 2.5: **Dwell Time versus Beam Dose.** A lithographic pattern is written for various combinations of dwell time and dose. The number of repeats increases from top left to bottom right and is over-determined by the choice of dwell time and dose. Structures in the boxed area show the highest quality. The scale bar is 1 μm long.

For aluminium, Figure 2.4 demonstrates that the number of repeats does not influence the quality of the nanostructure as long as the product of dwell time and number of repeats is constant. This is not the case for the last structure with a dwell time of 290μs. Gold shows a strong dependence on the number of repeats in Figure 2.4. The best choice is the use of only one or two repeats with a high dwell time, even though many repeats tend to yield narrower features.

While so far the dose was kept fixed, a broader picture of the parameter dependence is drawn in Figure 2.5 for aluminium. The number of repeats is again over-determined by the choice of dwell time and beam dose. The upper part of the image shows the inconsistent part of the parameter space. The milled area suddenly becomes very deep even for a constant dose, and distinct diagonal lines appear. In the left part the dose is too low to fully

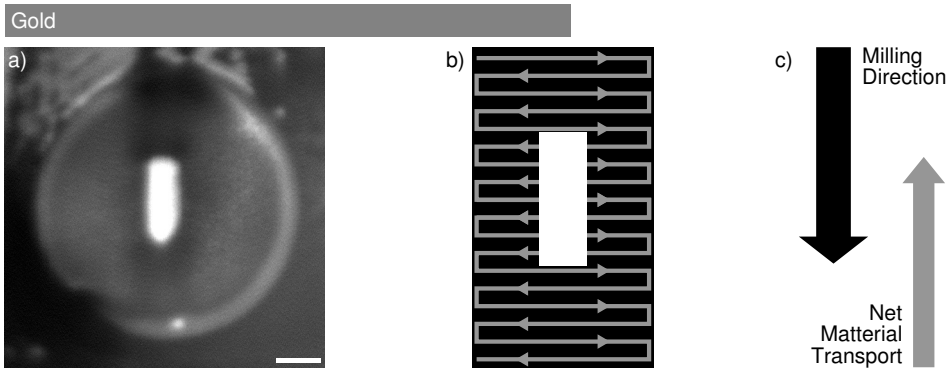

Figure 2.6: **Re-Deposition.** In (a), re-deposition appears as the triangular prolongation of the otherwise rectangular nanostructure. It can extend the nanostructure by up to 40 nm. The scan path of the ion beam is shown in (b). The general milling direction from top to bottom causes a net material transport in the opposite direction, shown in (c). This explains the re-deposition only at the lower end of the structure. The scale bar is 100 nm long.

remove the aluminium. The best structures are group in a slightly diagonal area in the lower right and correspond to a low dwell time with many repeats.

As demonstrated, aluminium and gold show a distinctively different dependence on the dwell time and the number of repeats for a structural layer on a flat cover slip. Scanning tips and fibres, however, may charge and drift substantially due to their geometry. Keeping the number of repeats at one and using a high dwell time effectively reduces the impact of drift, because the ion beam approaches the prospective nanostructure exactly only once.

Scan Direction, Re-Deposition and Clean-Up Layer. Ideally, the material sputtered by the ion beam is fully removed from the surroundings of the nanostructure and absorbed into the machine vacuum. However, some fraction will re-deposit in proximity to the nanostructure, and may seriously affect its shape [99]. Two options of compensating re-deposition are presented in this section: a modification of the trajectory of the beam, and the use of *clean-up* layers.

The effect of re-deposition is demonstrated in Figure 2.6. The rectangular pattern in Figure 2.6(b) has been used to write the nanostructure shown in Figure 2.6(a). In addition to the expected rectangular shape, the resulting nanostructure shows a triangular prolongation of about 40 nm in length on the lower end. This prolongation is the result of re-deposition of the

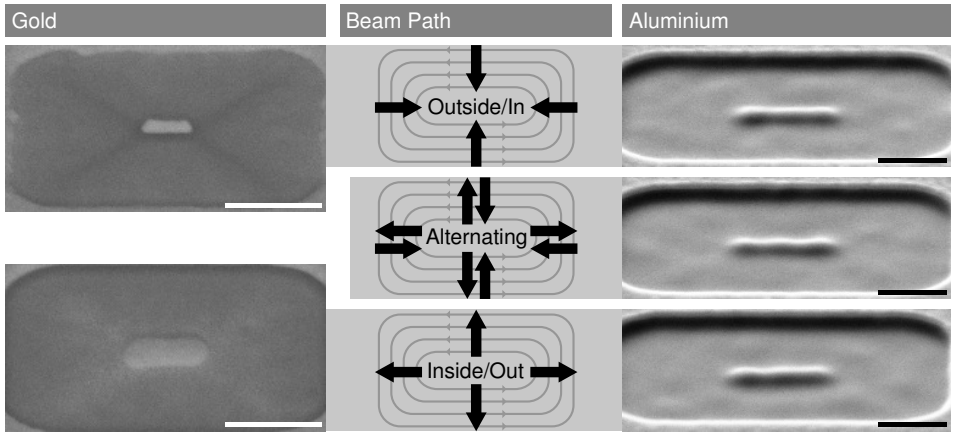

Figure 2.7: **The Beam Path.** The quality of the nanostructures depends stronger on the beam path for gold than for aluminium. The scale bars are 500 nm long.

sputtered material. Figure 2.6(b) shows why re-deposition occurs exactly at the lower end. At each position of the ion beam, sputtered material is re-distributed homogeneously in all lateral directions. The same amount of material is sputtered and re-distributed by the beam at an adjacent scan position, leading to a vanishing net flux of re-deposited material along the connecting line. Now, the beam shown in Figure 2.6(b) scans mostly along horizontal lines. The net re-deposition flux along each horizontal line is zero (end points neglected), but there is a flux away from the scan line in up- and down-directions with equal probability. The next scan line will not only sputter the original layer at its location but also the material that the previous scan line has re-posited here. This previously re-deposited material has an equal change of being re-redeposited in up- and down-directions. Summing up over several scan lines, this causes a net flux in re-deposition against the overall scan direction as depicted in Figure 2.6(c). This effect leads to the triangular prolongation at the lower end of the nanostructure.

The trick to avoid critical re-deposition at the nanostructure is a modification of the beam path such that the beam scans always against the nanostructure. The *NPVE* lithography software three options to control the beam path in the proximity of a nanostructure. The three different options of the scan path are listed in Figure 2.7. The beam scans circles the nanostructure and approaches it either from the outside to the inside or vice versa, or in both directions in alternating way. The implications for gold become immediately clear when comparing the two SEM images for

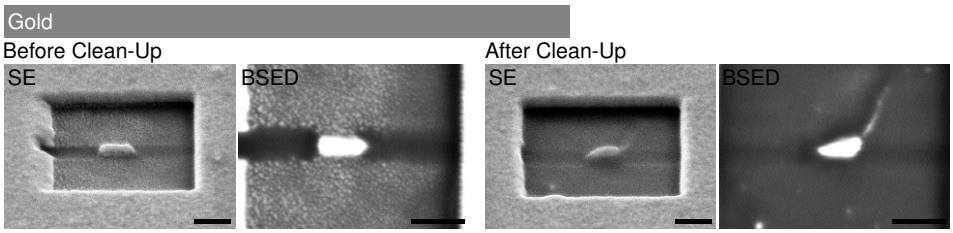

Figure 2.8: **Clean-up Layers.** All detectors show re-deposited gold bubbles on the milled surface before a second *clean-up* scan with a low dose. These are completely gone after the *clean-up* scan. The scale bar is 200 nm long.

outside-to-inside and inside-to-outside milling. For the latter, the structure widens by roughly 80 nm in each direction. Re-deposition seems less of a problem in the case of aluminium.

In general, all nanostructures presented in this thesis are fabricated using an outside-to-inside beam path.

The second option to avoid re-deposition is the implementation of a second writing pattern of identical geometry on top of the actual writing pattern. A lower dose is assigned to this second layer that only suffices to remove re-deposited material. Such an arrangement is shown in Figure 2.8. Before the application of this *clean-up* mill, the re-deposition clearly shows as gold bubbles in both the high-resolution secondary electron image and the material-sensitive backscattered electron image[1]. The second mill with a lower dose has completely removed these bubbles.

A problem associated with a second layer is that the sample may have drifted and the two layers are now slightly offsetted. This may introduce some asymmetry to the nanostructure. Also, instead of only a single dose, now two different doses are to be calibrated correctly. For the structures presented in the next chapters, I passed on applying a *clean-up* layer and consider the previously chosen outside-to-inside beam path as sufficient to compensate re-deposition.

Application Flow of Focussed Ion Beam Lithography

A strict routine of the lithography process is essential to fabricate plasmonic structures in an accurate and reproducible way. As previously explained, any exposure to the ion beam immediately degrades the structural layer and implants gallium atoms. It must be a major effort of the routine to

[1]The images were taken on different SEM / FIB systems. The secondary electron detector was attached to a better SEM.

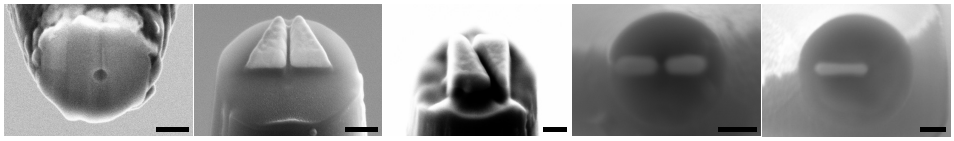

Figure 2.9: **Example of Fabricated Nanostructures.** These nanostructures show examplary the capability of FIBL as a method to structure on the end face of tapered scanning tips or fibres. The scale bars are 200 nm long.

keep the exposure to the ion beam at a minimum. A second motivation for a routine is the ability of the lithography to systematically a sweep a single parameter, e.g. the length of a nanostructure. Modification of only a single parameters implies the existence of a routine to keep all other parameters absolutely constant.

Before any lithography can be performed, the target has to be installed and properly aligned. The alignment of scanning tips and fibres is less straight-forward than for flat cover slips, because the scanning tips and fibres will have slightly different positions on their common mount; therefore, they do not share a common focal plane. As the ion beam is intrinsically destructive, an adjustment of the focus and the astigmatism for every scanning tip or fibre separately is not desirable. Using a single scanning tip or fibre to align the electron beam and the ion beam on their point of coincidence, it is possible to bring any other scanning tip or fibre exactly into the point of coincidence and thus in the focus of the ion beam without imaging with the ion beam.

Now the scanning tip or fibre is at the correct position to perform the lithography. All but the very first scanning tip or fibre have not been exposed to any ion irradiation. A single image is taken with the ion beam to localise the exact position of the end face and to position the lithographic shape. Figure 2.1 shows this image in the centre of the lithography programme. Once that is done, the exposure of the lithographic shape is performed.

2.5 Conclusion – Accurate and Reproducible Nanostructures

As the nanostructures shown in Figure 2.9 convincingly demonstrate, FIBL is a powerful and efficient method in the structuring of thin layers on optical fibres. Knowledge of the technical properties of the FIB system and its detection system has proven a prerequisite to a successful evaluation

of the milling process and the resulting nanostructures. With a thorough calibration of the milling parameters, the lithography system permits to fabricate a variety of shapes in a controlled, flexible and reproducible manner. Feature sizes of down to 20 nm are realised routinely even in this particular sample geometry.

Focused Ion Beam Lithography is thus fully capable of meeting all requirements that the experimental set-ups and the proposed experiments in chapters 3,4 and 5 impose on the nanostructured samples.

3 Mode Mapping of Optical Antennas

Nanophotonic structures offer emerging applications in many vibrant research fields, such as photovoltaics and sensing. An assessment of the working principles of such a structure requires knowledge of its spatial modal distribution, which determines the coupling of the structure to light field. As plasmonic structures typically confine light fields to as small as a few tens of nanometres, their analysis on the sub-wavelength scale is a very relevant topic.

Optical methods involving the far-field, as e.g. *two-photon photoluminescence*, are diffraction limited, and lack the required resolution. Near-field techniques such as *NSOM* place an aperture or scattering probe in close proximity to a structure of interest. However, for visible light, the size of the probe is comparable to the features of the structure, which may introduce artefacts to the recorded fields. Here, we propose to place the nanostructure of interest on a sharp dielectric tip, and scan this tip across single fluorescent beads. The beads probe the spatial modal distribution of the nanostructure through their fluorescence signal. The advantage of this method is that the scanned surface may contain a large number of beads and molecules that differ in dipole orientation, size, and spectrum, such that a bleached probe is readily replaced. We employ this method to probe the spatial modal distribution of optical antennas, observe modal features of 35 nm FWHM and reveal the antenna resonance.

The first section introduces the study of optical antennas. The fabrication, experimental set-up and performed numerical calculations are discussed in the second section. Mode maps and a resonance curve of optical antennas are presented in the third and concluded in the fourth section.

3.1 An Introduction to the Study of Optical Antennas

The challenge in the study of optical antennas and nanostructures in general arises from the strong localisation of their optical fields. An optical antenna is able to spatially confine optical radiation to an order of magnitude below the diffraction limit [37]. Obviously, an experimental method to study such an optical antenna must reflect this length scale in some way.

Several parameters may be of interest when assessing an optical antenna or a nanostructure in general. First, the strength of the resonance allows to judge how resonant a structure is compared to a second structure. This scalar parameter does not *per se* require experimental facilities with a spatial resolution better than the wavelength of light. Second, the spatial modal distribution shows how the localised field evolves around the optical antenna. The degree of confinement and the local enhancement of the field across the optical antenna are of interest in this distribution. Experimentally, the field must be mapped with a spatial resolution better than the sharpest expected feature of the near-field at the antenna. Third, a recording of the lifetime of an emitter placed close to the antenna and with a similar spatial resolution addresses the *local density of states* (LDOS) of the antenna. All these parameters are expected to be polarisation-dependent.

As an antenna is a three dimensional structure, an ideal experimental method would record all components of the electric and magnetic fields simultaneously. This is also called *vectorial* imaging of the field vectors.

Numerous methods have been developed in the past to access the near-field of a nanostructure. A review by Vogelgesang et al. [100] discusses extensively the various approaches. Apart from all-optical methods, the authors also mention various methods involving electron microscopes as the mean of excitation or detection, or both. As the topic of the thesis is optical control, these methods will not be considered here.

Assessment from the Far-Field. *Two-photon photoluminescence* (TPPL) is standard tool to investigate the resonant properties of a nanostructure [20, 21, 101–103]. The brightness of the luminescence signal indicates the existence and strength of an optical resonance. However, as a far-field method, the resolution of TPPL is fundamentally limited by diffraction. Therefore, a mapping of an antenna mode is not possible with TPPL. Also, as both excitation and detection are in the far-field, the excitation of certain modes may be forbidden by the symmetry of the modes.

Mapping Through Interaction in the Near-Field. These limitations may be overcome when recording directly in the near-field of the optical antenna. As a read-out of the near-field is possible only within its decay length of a

few tens of nanometres, a probe must be placed in close proximity to the optical antenna. The lateral resolution is now determined by the dimension of this probe. Near-field experiments require scanning of the probe and the optical antenna with respect to each other in order to map the localised fields and their properties spatially.

A large number of near-field probes have been developed and experimentally tested over the years, ranging from sub-wavelength apertures and pointed near-field scatterers to single or bunched emitters.

The excitation or imaging with sub-wavelength apertures is termed *Near-Field Scanning Optical Microscopy* (NSOM) [7, 104]. The aperture is fabricated at the end of a tapered fibre waveguide or AFM tip and surrounded by a metallic film that prevents light leakage from the waveguide or tip. As the intensity of the transmitted light scales with the diameter of the aperture to the power of minus four, the resolution of these probes is practically limited to 60 to 100 nm at most. Smaller probes do not transmit sufficient intensities. As a result, the resolution is not sufficient for highly confining nanostructures. In addition, the thickness of the metallic film is typically around 200 nm, bringing the total diameter of an aperture probe to around 500 nm or more. The presence of such a large metallised probe in close proximity to an optical antenna may alter the recorded local fields, thus distorting the results of the experiment.

An optical resolution of less than 10 nm is mastered with scattering (or aperture-less) probes. The resolution of these probes is mostly defined by the radius of their very tip and limited only by the required strength of the scattered signal. As scattering probes are excited and read out from the far-field, the signal-to-background ratio is comparably low. The choice of a strongly scattering metallic probe over a weakly scattering, dielectric probe may improve the ratio. However, the probe may couple to and distort the localised fields of the nanostructure of interest once again [105]. Variations of scattering probes include placing a metallic nanoparticle at the tip which acts as the scattering centre [49, 78] and may allow vectorial imaging of the electric field [106]. The challenge of positioning such a particle in a reproducible manner stably at that position remains unresolved. Also, nanostructuring of the probe has been a promising approach to excite plasmons on its surface that converge efficiently to the very tip [81, 82]. Independent of the exact configuration of the scattering probe, sophisticated experimental schemes are necessary to combine high resolution with low background, including modulation [107, 108] and cross-polarisation schemes [38, 109].

Single or bunched emitters belong to the third class of probes. They offer a number of advantages over the aforementioned aperture and scattering probes. First, the optical resolution of such a probe is largely equal to the physical size of the emitter. In the case of an effectively point-like single

molecule, the resolution is at the order of only one nanometre. Second, a single emitter may have a dipole momentum that has a fixed orientation in space; this emitter may preferably interact with only certain field components, which allows to vectorially image the complete electric field of an optical antenna. Third, the lifetime of an emitter is very sensitive to the presence of the metallic optical antenna, allowing for a spatial mapping of its lifetime and thus the local density of states of the antenna. Forth, as excitation and emission occur at different wavelengths, the readout of their response to the optical antenna is greatly simplified.

Placing an Emitter at an Optical Antenna. In order to spatially map the properties of the optical antenna (or any other nanostructure), the emitter must be placed deterministically at different positions with nanometre accuracy. As the size of emitters generally does not exceed several tens of nanometres at most, the positioning is not easily accomplished.

A very simple approach includes the drop-casting of emitters across the nanostructure, with a large enough ensemble of identical nanostructures. This random positioning of emitters may yield a sufficient coverage of all possible positions [110, 111]. Prior functionalisation of the surface may aid in the positioning process [29]. However, the emitters are fixed in their positions at the nanostructures and the intrinsic differences between the emitters and nanostructures add an error to the map from averaging across an ensemble.

AFM technology allows a deterministic positioning of larger emitters, such as nitrogen-vacancy centres, by physically pushing them to a desired position at the antenna [112–114]. Since this method is not a true scanning technique, the high time consumption and the potential loss of the emitter in the process are strong drawbacks.

A true mapping of the properties of an optical antenna requires to deterministically position and scan the emitter and the antenna with respect to each other. In the past, several groups have successfully attached an emitter to a scanning tip and scanned this emitter across a nanostructure. The emitter employed include single molecules [115] and single beads [116], nitrogen-vacancy colour centres [117], quantum dots [118] and doped particles [119, 120].

Even though an emitter attached to such a probe can be positioned deterministically at an optical antenna, the attachment of the emitter to the scanning tip is not well controlled. The attachment is performed either by chemical ligation or electrostatic attraction. For the former, the very tip must be functionalised successfully, such that the attachment is performed at the part of the probe that will be closest to the optical antenna. For

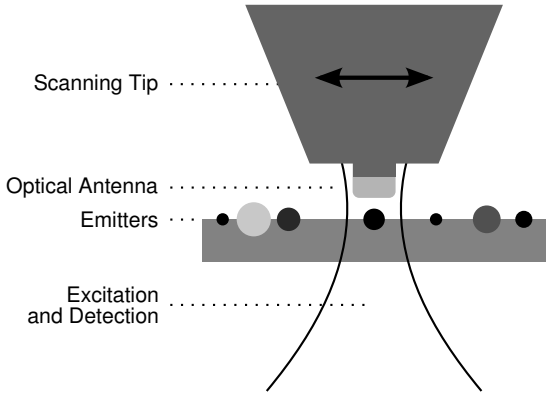

Figure 3.1: **The Proposed Scheme.** The optical antenna is directly fabricated into a scanning tip. One at a time, a multitude of molecules, beads or nanocrystals of different sizes, operating wavelengths or dipole orientations map the properties of the optical antenna through near-field interaction.

both attachment processes, the probability of a successful attachment event is well below unity and the probability of accidentally losing the attached particle is high.

The difficulty of the attachment process is especially relevant when employing single molecules or beads. These emitters will bleach after certain number of optical cycles and cease to be emitters. Therefore, they must be replaced very frequently. In the case of vectorial imaging, a single emitter with a dipole momentum fixed in space will only interact with the part of the local electric field parallel to its dipole momentum. Several emitters are already required to map all components of the field at the optical antenna, independent of bleaching events.

The Advantage of Scanning the Antenna across Beads. Obviously, the complicated attachment procedure and its subsequent challenges are avoided, if instead of the emitter being attached to the scanning tip, the optical antenna is cut directly into the scanning tip or the scanning tip. The scanning tip and the antenna become a single unit that easily and deterministically positioned and scanned as depicted in Figure 3.1. This method will be proposed and experimentally exploited within this chapter.

Chapter 2 has shown the reader the capabilities of a modern Focused Ion Beam (FIB) system when combined with a powerful lithography system. The preciseness and reproducibility of these systems permit to accurately fabricate a range of optical antennas, each into a different scanning tip,

that differ systematically in a desired parameter (e.g. in the length of the antenna). The combination of FIB and lithography has not only increased the fabrication accuracy of optical antennas, but has greatly reduced the time consumption.

The reader may object that, for a systematic study of optical antennas, it is not convenient to have placed all optical antennas on scanning tips that have to be mounted and recorded individually in the experimental set-up. The major advantage of this proposed method is, however, that the emitters probing the local field are now simply spin-coated onto a flat cover slip. Instead of only a single emitter at a scanning tip, a multitude of emitters on the cover slip are available as field probes. Bleaching of the emitter is not critical anymore, because there is an abundance of replacements readily available. Furthermore, the cover slip may contain single molecules, beads and nitrogen-vacancy centres at the very same time that also differ in spectrum, size, quantum efficiency, or dipole orientation. In principle, this method provides a multitude of information on a single optical antenna in a simple way. A systematic study of several optical antenna is still straightforward due to the advances in nanofabrication technology.

An additional advantage is of more technical nature. The emitter acts as the local field probe and its emission must be recorded by a detector. If the emitter is scanned, its relative position to the detector changes. If the change in relative position is large enough, the signal from the emitter arriving at the detector may be modified or even vanish. Therefore, scanning the emitter may add uncertainty in the recorded data. A scan of arbitrarily large antenna structure may be impossible. In the proposed scheme, the emitter always remains at the same position.

3.2 Fabrication, Set-Up and Numerical Calculations

The previous section detailed the proposed method to map the local field of optical antennas. This section lists the steps taken prior to the actual experiments. The fabrication of the optical antennas on the scanning tip and the preparation of the polymeric matrix containing the probing fluorescent beads are explained in detail in this section. Furthermore, numerical calculations show the impact of critical design parameters of the antenna and the scanning tip on the optical resonance of the antenna. The section closes with a description of the experimental set-up and the experimental routine.

The Fabrication of Optical Antennas on Scanning Tips

The aim of the nanofabrication is to cut an optical antenna into an aluminium film. The aluminium film is deposited on the flat end face of the scanning tip, that has a diameter of around 500 nm. As will be seen later in this section, the first order resonance of an aluminium optical antenna is expected to occur at a length of about 170 nm. Therefore, the major challenge in this section is to accurately and reproducibly fabricate a nanostructure of 170 nm in length on an end face of just 500 nm in diameter. Also, as a focus of the investigation is the relation between optical properties and length of the antenna, shorter and longer optical antennas may be fabricated with specific lengths. As the strength and spectral position of the resonance will depend on the full three dimensional shape of the antenna, height and width are to be kept constant such that only the length will be a parameter.

The fabrication of such an optical antenna on a scanning tip can be divided loosely into two steps. In the first step, the scanning tip is prepared and, in the second step, the actual optical antenna is milled into its end face.

Preparation of the Scanning Tip. An optical fibre is the base of the scanning tip. The fibre is tapered by heat-pulling (see Section 2.2)[1]. Now, the tapered scanning tip has a rounded tip with a radius of around 50 to 80 nm; however, a flat end face is required such that an optical antenna can be placed there. The deposition of a thin layer of titanium (see Section 2.2) provides conductivity such that the scanning tip can placed in an FIB system and a flat end face of 500 to 900 nm in diameter can be milled. The end face is then coated first with a thin adhesion layer of 2 to 5 nm titanium and second with the structural layer, roughly 60 nm of aluminium (see Section 2.2).

Fabrication of the Optical Antenna. The optical antenna is milled into the aluminium film of the scanning tip using an FIB system. Section 2.4 details the steps undertaken to calibrate the system. Once this calibration routine is completed, the electron and the ion beam are focused on the end face and the optical antenna can be milled safely.

Figure 3.2(a) is taken with the ion beam and shows the end face of the scanning tip as seen with the lithography programme. The scanning tip points towards the viewer. The sharpness of its edge confirms that

[1] Remark: Even though the scanning tips are drawn from an optical fibre, they merely act as a sharp glass tip. In the experiments presented here, no light will be guided through them and they are not longer than two centimetres.

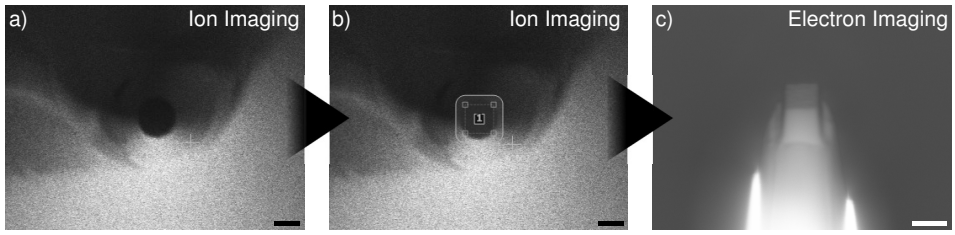

Figure 3.2: **Lithographic Milling.** The scanning tip with the metallised end face is positioned within the imaging screen of the *NPVE* lithography software. The clear features of the round end face in image (a) confirm that the scanning tip is well-focused on. The lithography shape is positioned in (b). The result after exposure to the ion beam, a square of gold, is shown in (c). Images (a) and (b) are taken with the ion beam and (c) with the electron beam. All scale bars are 500 nm long.

the ion beam is well-focused on the end face, a prerequisite to mill sharp antenna features. In Figure 3.2(b), the lithographic shape is placed on top of the outline of the end face. Once the positioning is satisfactory, the lithography process is started. Figure 3.2(c), taken with the electron beam under an angle, shows the scanning tip after exposure to the ion beam. The lithographic shape, in this case a square, is clearly visible.

During the fabrication process, the end face with the structural aluminium film has been exposed to the hard ion beam only a single time to position the lithography pattern on the scanning tip in Figure 3.2(b). All other images are taken with the SEM only, such that the implantation of ions into the sample and surface damage due to irradiation by ions are kept at an absolute minimum.

Discussion of an Exemplary Optical Antenna. Typical scanning tips with optical antennas at different steps of the fabrication are displayed in Figure 3.3. The tapered and metallised scanning tip in Figure 3.3(a) has been the starting point for the milling process. The dark and round end-face visible visible in Figure 3.2(a) corresponds to this state.

The typical topography and material composition of a scanning tip with an optical antenna after FIB milling is presented in Figure 3.3(b). The previously flat surface of the end face is very rough now and the optical antenna sits on a socket of glass of over 100 nm in height.

Aluminium as a material is difficult to mill in the frontal configuration required by the antenna fabrication. The sputtering rate strongly depends on the size and position of single aluminium grains and the sputtered atoms recombine quickly on the surface. This explains the visible roughness of the

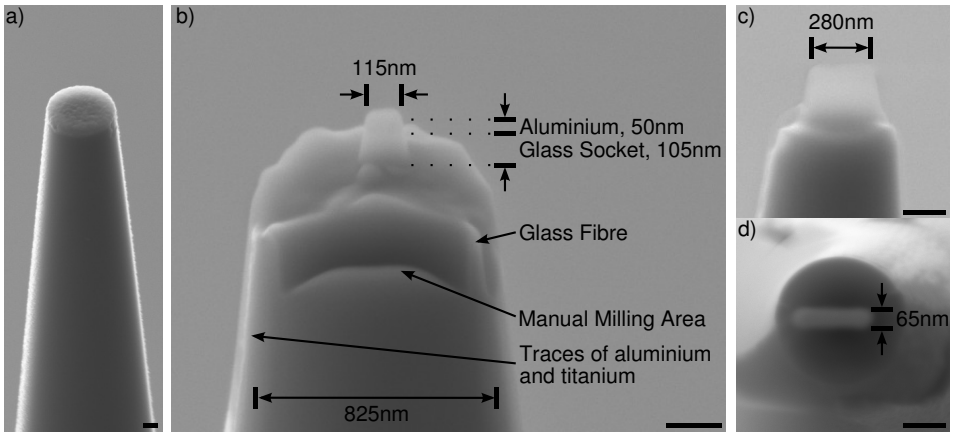

Figure 3.3: **The Fabrication of Optical Antennas.** Metallised, tapered scanning tips as presented in (a) are the starting point for the fabrication of antennas. The SEM image in (b) shows the composition of a typical antenna probe. The actual antenna is separated from the glass surface by a glass socket. The surface appears very rough after the milling, which is a result of the specific milling behaviour of aluminium. In some cases, remaining perturbing features are removed by manual milling. The variance in the size of the scanning tip is clear from (c), where the antenna covers almost the complete tip. The average width of a lithographically fabricated antenna is 65 nm as seen in (d). All scale bars are 200 nm long.

end face around the antenna. In addition, no available detector is capable of differentiating between aluminium and the glass of the optical fibre (see section 2.3). The only strategy to fabricate an optical antenna made of aluminium and without any electrically short-cutting traces of aluminium remaining nearby, is to employ a larger-than-necessary dose. The existence of the glass socket is the consequence of this larger dose. Should some traces of spurious aluminium still remain on the end face, a manual mill is applied in order to clean the affected area.

From an experimental point of view the existence of the socket is advantageous. As the large end face is separated from the fluorescent beads by the height of the socket and the optical antenna, roughly 150 nm in total, only the antenna and the bead can interact within the near-field. To some extent, the diameter of the scanning tip can be adapted to the length of the optical antenna. Figure 3.3(c) shows such a case.

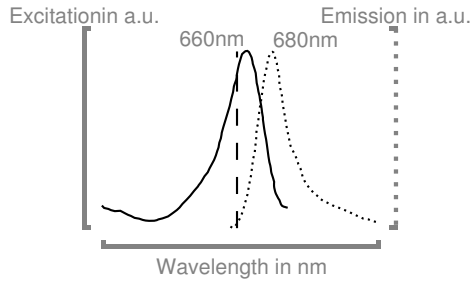

Figure 3.4: **Spectra of the Fluorescent Beads.** Excitation and emission spectra of *Invitrogen no 8783* beads of 20 nm in diameter. The dashed line indicates the wavelength of the exciting laser, 647 nm. The peaks of absorption and emission are at 660 nm and 680 nm, respectively [121].

The Range of Fabricated Optical Antennas. The resonance of the type of rod antenna shown in Figure 3.3, depends mostly on its length. In the fabrication, the height and width of the antenna were kept as constant as possible. For the former, this corresponds to a careful calibration of the deposition process for aluminium. The latter is achieved by a careful focusing of the ion beam on the end face and the employment of fully identical lithographic shapes that differ only in the length.

Optical antennas with lengths in the range of 100 to 600 nm were fabricated, which covers the first-, second- and third-order resonances for an excitation wavelength of 647 nm. Their widths are identical to only a small error and determined as 65 nm, as indicated in Figure 3.3(d). The height of the aluminium layer is 60 nm directly after the deposition process. Damage induced by initial imaging with the ion beam and second order effects have reduced the thickness by an amount that cannot be determined from the SEM images. However, as will be seen later in this chapter, numerical simulations with a thickness of 50 nm agree well with the experimental data.

The Preparation of the Single Fluorescent Beads

As the absorber and emitter that will act as a field probes in the later experiment, I have chosen polystyrene beads of 20 nm in diameter (Invitrogen FluoSpheres 8783). Their excitation and emission spectrum is presented in Fig. 3.4. The beads were excited at 647 nm with an Innova Spectrum 70C Argon-Krypton laser. This specific bead size is small enough to be fully penetrated by the near-field of a nearby nanostructure, but still generates sufficient fluorescence as it contains a few hundred dye molecules. Each molecule has a random orientation inside the bead, such that the bead is

equally stimulated by all field components of the local field at the optical antenna.

The beads are diluted in a solution of 3% Polyvinyl Alcohol (PVA) in water, well-mixed in an ultrasound bath, and finally spin-coated on a cleaned standard microscope glass slide. The thickness of the resulting film is verified by an AFM measurement and determined to roughly 70 nm which is sufficiently small for the application. The concentration of the dyes is adjusted such that beads appear well-separated and Gaussian-shaped in images taken with a standard, diffraction-limited confocal microscope. In the later experiment, extremely bright beads were avoided as the brightness may be due to clustering of many beads. This procedure was sufficient to perform the experiments on actual single beads and a final mass concentration of 10^{-3} % of the original bead solution and the solution of PVA in water was selected.

After spin-coating, the samples were dried at ambient conditions to remove the remaining solvent.

Numerical Simulations of Optical Antennas

Numerical calculations were performed to estimate the fabrication tolerances and to verify the experimental results. As the simulation tool, I used the commercial finite-difference time-domain (FDTD) software *Lumerical* by the company of the same name. A simulation software must always be an approximation to the actual experimental situation. The quality of the approximation is not only limited by the available computing power, but also by the programming tools and objects available in the software.

Compromises in the Numerical Calculations. In the experiment, the optical antenna is excited by a Gaussian diffraction-limited beam. The antenna converts the energy of the Gaussian beam to a localised field. This localised and enhanced field drives the bead which in turn responds with an increased fluorescence.

In the simulation, this situation can only be approximated. The first approximation concerns the illumination. Only a special plane wave source can be spatially restricted, such that a monitor placed outside the volume with the plane wave records only the antenna fields and not the excitation field. Figure 3.5(a) depicts this situation. The scanning tip with the antenna is approximated by an infinite glass surface, under which the optical antenna sits on the glass socket and an adhesion layer. The substrate on which the beads are placed is also approximated by an infinite glass surface. The inner rectangular shape surrounding the antenna, the adhesion layer and the socket is the boundary of the exciting plane wave. The outer

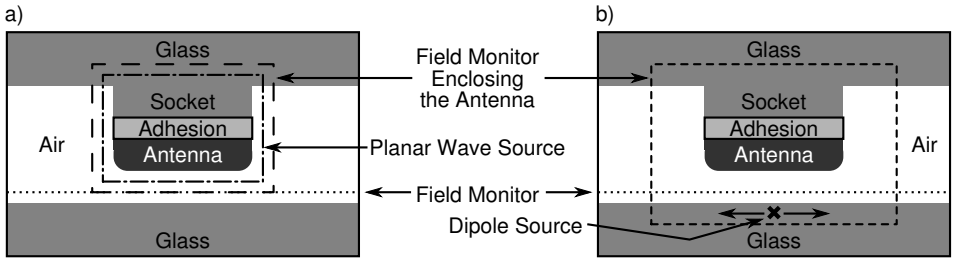

Figure 3.5: **Sketch of Simulation Domains.** In (a), a plane wave excites the antenna homogeneously. The plane wave is polarised along the antenna axis and irradiated from the bottom. In (b), a dipole emitter is placed into the glass under the antenna. One field monitor maps the field of the antenna as the bead would experience it directly above the glass substrate. A second field monitor fully encloses the antenna and allows to record the strength of the total electric field on the surface of the antenna. The sketch is not-to-scale.

boundary, in 6 nm distance to the antenna and the socket, is a field monitor to record the strength of the near-field of the antenna. An equivalent situation involving a Gaussian source, resembling the experimental situation, is extremely difficult to realise, because the excitation and the antenna field cannot be discriminated with certainty. As shown later, these simulations match the experimental resonance data very well and this approximation is justified retroactively.

The second approximation involves the field actually driving the emitter. In the previous situation, the strength of the resonance is measured by integrating the local field across a surface. This value is then set equivalent to the expected magnitude of the fluorescence to be measured in the experiment. However, the emitter is much smaller than the antenna and therefore not driven by the full integrated field of the antenna. In more complex designs, there can be substantial deviations between such calculated resonance and the experimental data.

In Figure 3.5(b), a dipole source instead of a plane wave drives the optical antenna. The dipole source can be scanned underneath the antenna. It is placed inside the glass substrate, which has the same index of refraction as the matrix of Polyvinyl Alcohol in which the beads are embedded. This configuration stresses the point-like character of the bead and the actual scanning of the bead during the experiment. Since the dipole source drives the antenna only locally, the field monitors only map the effect of the local driving, avoiding the problem explained in the previous paragraph. Even though the situation seems reversed — the dipole source excites the

antenna, while in the experiment the antenna fields excite the beads — it is fully equivalent for odd-order resonances that are equally driven by local sources and plane waves.

A major difference between both situations is that a plane wave can only drive odd-order resonance, while the dipole source can drive any resonance. In this chapter, complementary numerical calculations in both simulation domains will be presented to support the experimental data in the most comprehensive way.

The following simulations in this section are all performed using a plane wave source as depicted in Figure 3.5(a) that is polarised in-plane along the axis of the antenna.

The Effect of the Height of the Antenna. The height of the antenna is not equal to the height of the deposited aluminium layer. Irradiation by gallium ions during imaging of the scanning tip and second order effects will have reduced the thickness depending on the dose received. In principle, it should be possible to determine both the height and curvature of the aluminium antenna from the SEM images. However, as the antenna is necessarily an isolated structure, the direct surroundings are purely dielectric. Charging effects reduce the resolution to the point that the exact boundary of the aluminium part cannot be determined with certainty. The socket and the antenna appear as a homogeneous body. Similarly, the curvature cannot be resolved with certainty.

Figure 3.6(a) shows that an increase in height of the antenna strongly decreases the strength of the resonance. The spectral position of the resonance is not effected for the first-order resonance. However, the third-order resonance shifts by as much as 50 nm when changing the height by 40 nm.

The Effect of the Curvature of the Antenna. In Figure 3.6(b), the resonance behaviour is plotted for different radii of curvature of the optical antenna. A radius of curvature of 5 nm corresponds to an almost box-like antenna, while an antenna with a radius of 40 nm has the shape of half a cylinder. For the first-order resonance, the resonant length shifts by as much as 30 nm when the radius of curvature is changed from 5 to 40 nm.

As the effective resolution of the FIB system is better than 20 nm, the curvature constitutes a relevant parameter. We anticipate an approximate radius of 30 nm from the SEM images and a comparison of the spectral position of the resonance between simulation and experimental results.

The Effect of the Height of the Socket. The height of the socket on which the antenna sits is unknown as well. While the overall height of

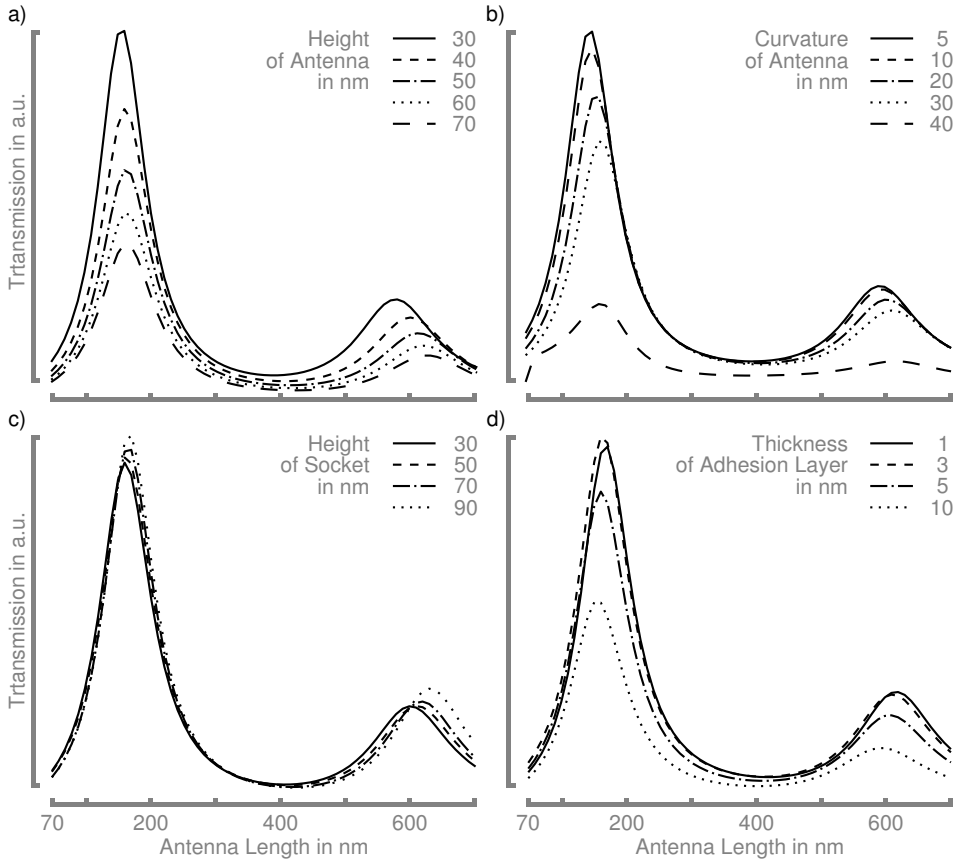

Figure 3.6: **Dependences of the Resonance.** (a) The spectral position of the first-order resonance shows hardly any dependence on the height of the aluminium antenna, while the third-order resonance shifts slightly. The strength of the resonance fades with increasing height. The second-order resonance cannot be excited by a plane wave and remains invisible. (b) An increasing curvature of the antenna weakens the resonance considerably. The spectral position shifts by 30 nm to longer wavelengths when increasing the curvature from 5 to 40 nm. (c) The height of the glass socket has little influence on the resonance, while the thickness of the adhesion layer in (d) damps the strength of the resonance.

socket and antenna is measurable by SEM, none of the two heights are known individually. As mentioned before, the interface between aluminium and glass is invisible to the SEM due to charging effects and the height of the aluminium can only be approximated.

Fortunately, as the simulated resonance curves in Figure 3.6(c) show, there is no shift in wavelength or amplitude for heights of the socket between 30 and 90 nm. Only for the third-order resonance some shift is visible.

As a consequence, the height of the socket will be neglected as a relevant parameter.

The Effect of the Adhesion Layer. The crystalline structure of a deposition material is often quite different from that of the substrate. As a results, the growth on and the adhesion to the substrate may be poor. The film may not be smooth enough to mill an optical antenna and the mechanical stability insufficient for the friction experienced during near-field scanning. A thin layer of titanium has been employed to improve the adhesion of aluminium to the glass substrate. However, titanium not favourable for plasmonic applications and a shift of the spectral position and a decrease in strength of the resonance is to be expected [89, 90].

Several resonance curves for different thicknesses of the adhesion layer are presented in Figure 3.6. When increasing the thickness from 1 to 10 nm, the amplitude at the resonances drops by 30 to 50%. The wavelength of the resonance does not shift. The fabrication tolerance of the deposition system can only be estimated at thin layers. Assuming a tolerance of at most ± 5 nm, a nominal thickness of 3 nm set in the deposition system will lead to a shift of the resonance wavelength by at most 10 nm. The strength of the resonance will increase or decrease by at most 20%. In any case the thickness of the adhesion layer should be kept as constant as possible during the fabrication. Its possible impact should be closely monitored in the analysis of the experimental data.

A Conclusion. The numerical calculations show indeed a first-order and a third-order resonance. The resonances occur at lengths of the optical antenna of around 170 nm and 600 nm, respectively. The most relevant fabricational parameters are the thickness of the adhesion layer and the height of the antenna. While the spectral shift of the resonance is negligible, a strong damping of the resonance may be a result of an unfavourable choice of parameters.

The Experimental Near-Field Set-up

The experimental set-up must bring the scanning tip with the optical antenna close enough to the fluorescent beads such that the bead and the antenna interact through near-field coupling. The near-field microscope used for the experiments in this chapter has already been introduced in Chapter 1. In this section, only the relevant properties for this experiment will be detailed.

The set-up bases on a standard confocal microscope. An Argon-Krypton laser at an operating wavelength of 647 nm provides the illumination and is focused by an NA1.4 objective into a diffraction-limited spot. The fluorescent beads that will probe the local antenna field are placed on a standard cover slip. A piezoelectric scanner permits the three-dimensional positioning of the cover slip. The fluorescence of the beads is projected onto two orthogonal polarisations and recorded by two avalanche photo detectors (APD). Therefore, the excitation and detection of the beads is exactly as in a standard confocal microscope.

The difference lies in the presence of a scanning tripod which holds a second three-dimensional piezoelectric scanner. The scanning tip with the optical antenna is placed on this scanner. A feedback system based on shear-force contacts controls the vertical axis of this scanner and allows to bring the scanning tip into near-field contact with the beads below on the cover slip.

With this set-up it is possible to independently position and scan the single beads and the scanning tip with the optical antenna with respect to the optical axis of the microscope. As will be clear from the next section on the experimental routine, the presence of two independent piezoelectric scanners is essential for the experiments.

The Description of the Experimental Routine

Central to the proposed method of mode mapping is the role of a single fluorescent bead as the probe for the local electromagnetic field of the optical antenna. The sensitivity of this method depends critically on how well the single bead can interact with the field of the optical antenna and on how well the fluorescence signal from the bead is collected by the detection system.

The effort undertaken to ensure a good alignment is explained in Figure 3.7. In the initial configuration shown in Figure 3.7(a), the beads are randomly positioned with respect to the optical axis. With an initial orientation scan, the beads are localised and a single bead is centred both axially and laterally on the optical axis of the microscope as shown in Figure 3.7(b).

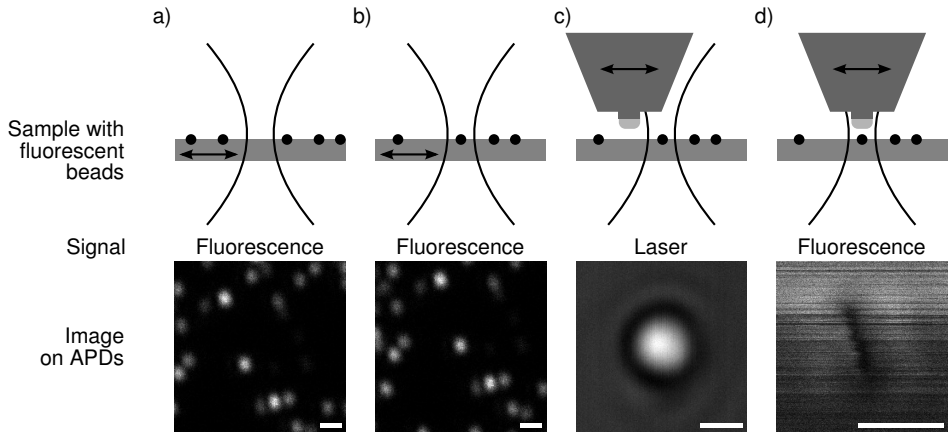

Figure 3.7: **Flow Chart of the Experimental Routine.** As the bead acts as a field probe of the optical antenna, careful alignment to the centre of the optical axis is essential and shown in (a) and (b). In (c), the scanning tip with the antenna is localised to a few 10 nm by scanning it through the optical axis and recording the scattered laser light. The final configuration is shown in (d), where a fluorescent bead is exactly on the optical axis and the antenna is being scanned across.

As the long-term stability of the position of the bead is very essential, the stability of this position is monitored and, if necessary, corrected for at least an hour. At this point, the bead as the field probe is well-positioned on the optical axis and the detectors are aligned to optimally capture the fluorescence of the bead.

In the next step, the scanning tip with the optical antenna is brought almost into contact with the cover slip and a fine positioning in lateral direction is performed. This is necessary as the initial position adjusted with the help of a CCD camera can be several micron off the optical axis. As shown in Figure 3.7(c), now the laser light scattered by the scanning tip is recorded instead of the fluorescence of the bead. The image of the scattered light shows a convolution of the diffraction patterns of the tip itself and any structure on the end face. For the vast number of scanning tips, this diffraction pattern has sufficient symmetry to identify the exact position of the centre of the tip, as is the case in this image.

The final configuration, in which all experiments were performed, is presented in Figure 3.7(d). If possible, each scan was performed for a polarisation of the excitation parallel and perpendicular to the axis of the optical antenna. Even though the optical antenna has a length well below the diffraction limit and is not directly visible, in most cases the first scan

showed some shape similar to that in Figure 3.7(d), which allows to deduce the likely position of the axis.

3.3 Results – Mode Mapping with 35 nm Plasmonic Features

In the previous section, the preliminary steps leading to the experiments, including the fabrication of scanning tips with optical antennas, numerical calculations of antenna parameters and their tolerances, the experimental set-up and the experimental routine were discussed.

Here, experimental findings and numerical simulations are presented. In the first part, the impact of the presence of a scanning tip on the angular emission of the single bead is explored. Following up are recorded mode maps of optical dipole antennas. The section closes with the demonstration of a resonance curve and a discussion on the mechanism behind the enhancement of the fluorescence.

Collection Efficiency in Proximity of the Probe

Since any microscope objective has only a finite collection angle, it is important to investigate and analyse the spatial radiative properties of the joint system of optical antenna and single bead. As the single bead acts as the field probe, a possible modification of the fluorescence signal of the field probe due to an interplay of collection angle and spatial radiative properties must be a very critical aspect to this method.

In an attempt to investigate the interplay experimentally, a scanning tip with only a flat end face and no optical antenna was used as a simplified model. The diameter of the flat end face is about 900 nm and the end face had not been metallised. This simplified geometry has two advantages. On one hand, as the end face will be close enough to the single bead to enable an interaction in the near-field, a metallisation might have resulted in quenching of the fluorescence [122, 123]. In this case, it might have been impossible to de-convolute the interplay of collection angle and spatial radiative properties from the impact of quenching. On the other hand, as an optical antenna is not required, it is not necessary to mill frontally into the end face. As demonstrated in Figure 3.3(b), the outcome of the frontal milling is a very rough end face, of which any feature can interact individually and unpredictably with the single bead. In this simplified model, the scanning tip has a completely flat end face, similar to the scanning tip shown in Figure 3.3(a) which is metallised, however.

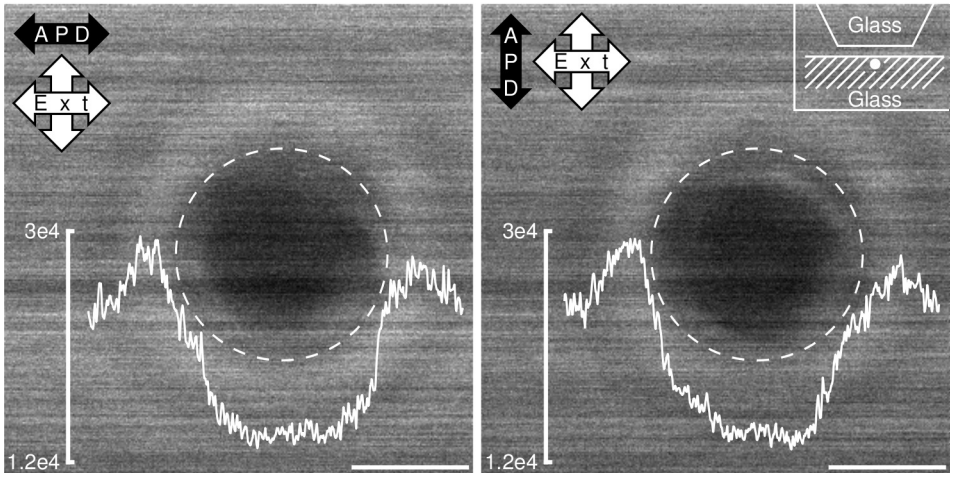

Figure 3.8: **Emission Beneath the Scanning Tip.** A single fluorescent bead is placed in the focus of the microscope and its fluorescence polarisation-resolved by two APDs as indicated by the arrows. When a scanning tip with a flat glass end face, similar to that shown in Figure 3.3(a) but without metallic film, is scanned across the bead in close proximity, the collected fluorescence drops by almost a factor 2 directly under the tip. It is important to note that the collected fluorescence under the tip remains constant over a length of almost 600 nm. The dashed circle indicates the extent of the end face, directly outside which a somewhat brighter corona is visible. The experimental configuration is shown in the inset and the scale bars are 500 nm long.

Polarisation-resolved maps of the fluorescence of a single bead while scanning the aforementioned scanning tip across are presented in Figure 3.8. An elliptically polarised excitation at a wavelength of 647 nm reflects the rotational symmetry of the scanning tip. Clearly visible is a circular region in the centre, where the detected fluorescence drops by almost a factor 2 with respect to the surrounding level of fluorescence. Within that region, the detected fluorescence remains fairly constant. In the figure, the extent of the end face is marked by a dashed circle. Just outside that circle, the detected fluorescence increases slightly to form a clearly visible corona. Outside that corona of increased fluorescence and the extent of the end face, the fluorescence resumes a constant value again. Here the scanning tip is laterally too far away from the fluorescent bead as that it would affect the radiation properties.

The transition region between the area of low detected fluorescence in the centre through the corona of increased detected fluorescence, to the

surrounding region of constant, by the presence of the scanning tip undisturbed fluorescence has a width of approximately 250 nm, which is roughly equivalent to the diffraction limit at this wavelength.

A modification of the quantum efficiency can be ruled out safely as a reason for the modification of the fluorescence. As the scanning tip is purely made of a dielectric and no metal is present at the end face, the non-radiative decay channel is not altered by the presence of the tip. The fluorescent beads, optimised for marker applications in biology, already have a very high quantum efficiency, which means that the radiative decay rate is much higher than the non-radiative decay rate. Therefore, the quantum efficiency of these beads cannot increase or decrease in the presence of a dielectric scanning tip. The modulation must originate in the spatial radiation properties of the system of single bead and scanning tip, namely the angular emission. The angular emission can be tailored in two possible ways. The first is to couple the single emitters within the bead resonantly in the near-field to a nearby nanostructure [28]. While in principle this could happen in the measurements with optical antennas presented in the next sections, there is absolutely no nanostructure present on this scanning tip.

The second option to tailor the angular emission is the layering of materials with different indices of refraction. A dipole emitter in a homogeneous medium will emit symmetrically in a plane perpendicular to its dipole momentum. In the case of a standard confocal microscope and an emitter immobilised in a polymer matrix, the dipole emitter will be located close to the interface between the polymer on the cover slip and air. As the polymer has almost the same index of refraction as the cover slip, the interface between polymer and air is the only interface present near the emitter. The proximity of the interface between materials of higher and lower index of refraction breaks the symmetry in the emission and causes a bending of the emission pattern into the cover slip [124, 125]. Modern microscope objectives are designed to maximise the collection efficiency by taking advantage of the existence of this interface and the bending of the emission lobes. K. G. Lee et al. [126] even reached a near-unity collection efficiency with a standard objective by tailoring the angular emission with sophisticated layering of three different materials.

In the present experimental configuration, the interface between the cover slip with the polymer matrix and air gradually ceases to exist with an approaching scanning tip. As the scanning tip has the same index of refraction as the cover slip and only an air-filled gap of several nanometres remains between the scanning tip and cover slip, the local environment of the bead becomes homogeneous again. As a consequence, the collection efficiency is reduced, which is clearly visible in Figure 3.8.

For a scanning tip with an optical antenna made of aluminium, this effect will be similar. The refractive index of aluminium is 1.54 at a wavelength of 647 nm, almost identical to the refractive index of glass, 1.52, considering that the space occupied by the scanning tip and the antenna now was formerly filled with air of a refractive index of 1. The only difference to the fluorescence map shown in Figure 3.8 of a planar glass scanning tip will be the spatial extent of the region where the angular emission is modified. An optical antenna occupies only a fraction of the end face, while the rest of the end face is not close enough to the bead to interact in the near-field due to the presence of the socket (see Figure 3.3)(b).

Mode Maps of Optical Dipole Antennas

In this section, optical antennas are scanned across single fluorescent beads following the routine described in Section 3.2.

An overview of experimentally recorded fluorescence maps for different optical antennas is presented in Figure 3.9. The two Avalanche Photo Detectors record the emitted fluorescence in the two orthogonally polarised components. For each optical antenna, the fluorescence maps are recorded for an illumination polarised parallel and perpendicular to the axis of the antenna. As the mounting procedure for a scanning tip with an optical antenna permits an initially unknown rotation of the scanning tip around its own axis, the optical antennas have different orientations with respect to the two APDs. For the sake of clarity, the fluorescence maps are rotated until the axis of the optical antenna is horizontal aligned. The respective axes of the two APDs and the excitation polarisation are clearly marked by arrows.

Modification of the Angular Emission or Quenching? Clearly distinguishable especially for the longer optical antennas with lengths of 370 nm and 400 nm is a region with a lower fluorescence count that has a similar shape and dimension as the optical antenna. The previous Section 3.3 has already discussed the effect of the presence of a scanning tip without antenna on the angular emission of the bead. We observed a decrease in the detected fluorescence by as much as a factor 2. While this phenomena was measured using a purely dielectric scanning tip, now a metallic antenna is in close contact to the surface and the fluorescent bead. The presence of the metal may *quench* the emitter [122, 123] which would provoke a similar decrease in fluorescence on our detectors as a modification of the angular emission.

However, the presence of quenching is very unlikely for a number of reasons. First, the degree of decrease in fluorescence and its spatial boundary

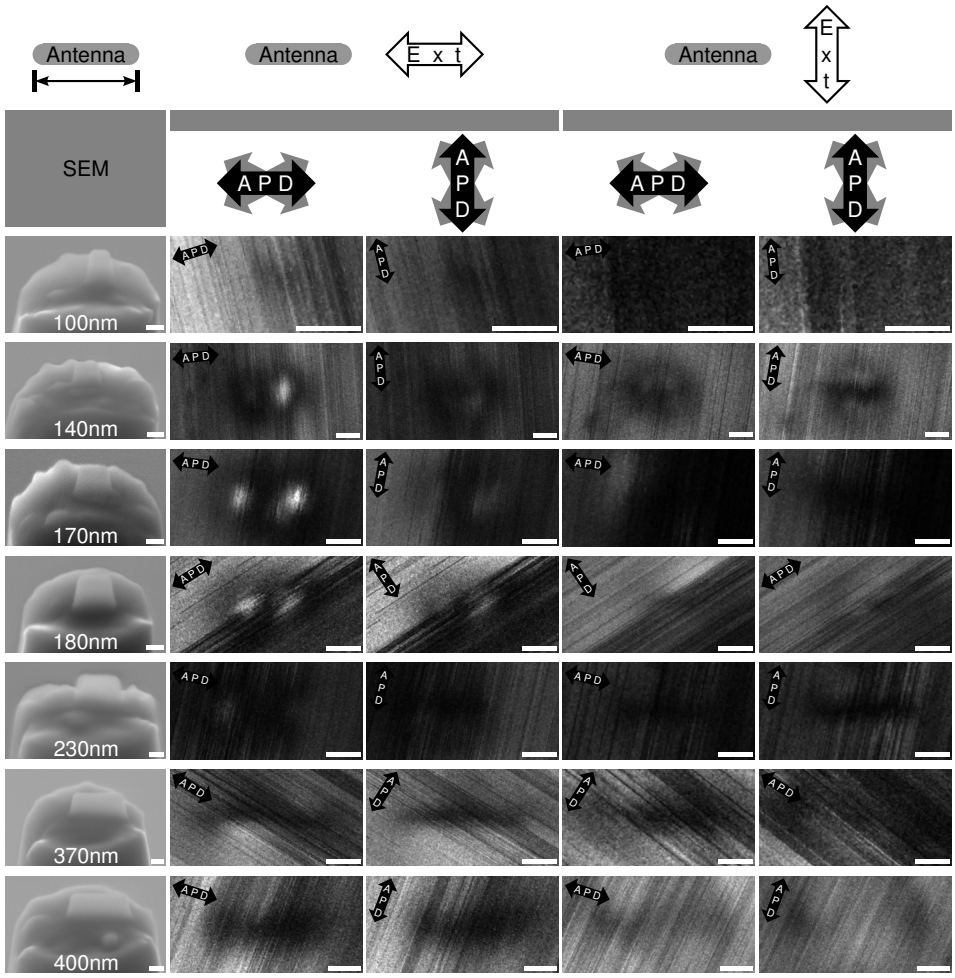

Figure 3.9: **Overview of Different Mode Maps.** Optical antennas with different lengths are scanned across single beads and their fluorescence spatially mapped. All fluorescence maps are rotated such that the axis of the antenna is along the horizontal. The black arrows indicate the exact polarisation mapped by each APD for each map. In the first column, the antennas are excited along their axis and the fluorescence polarised along the same axis is recorded. For this configuration, an antenna of the correct length is expected to reveal its resonance. Indeed, the antennas with lengths 140 nm, 170 nm and 180nm show bright fluorescence spots at their ends, indicating the first-order resonance. The other three columns present fluorescence maps with the excitation or the APD aligned perpendicular to the antenna axis and show as expected no sign of the resonance. All scale bars are 100 nm long.

show a dependence on the polarisation of excitation. Second, quenching occurs on very short distances of only a few nanometres. As the diameter of the bead is 20 nm, not all molecules within the bead are close enough to the metal to experience quenching. Third, the optical antenna will never be perfectly parallel to the scanning plane, but tilted by a small amount. Therefore, one end of the antenna will always be further away from the fluorescent beads than the other end. Due to the short quenching length, a modulation of the quenching rate would be expect along the tilted antenna. The decrease in fluorescence, however, is homogeneous along the whole length of the antenna.

These three argument show conclusively that the decrease in detected fluorescence is due to a modification of the angular emission and not due to quenching.

The Resonant Antennas. The fluorescence maps for the optical antennas with lengths of 140 nm, 170 nm and 180 nm each show two spots of increased fluorescence which would be expected for the first order resonance of an optical dipole antenna. These spots appear only for an excitation along the axis of the antenna. They are strongest the better the axis of the antenna is aligned with one of the two orthogonal polarisations recorded by the APDs. They disappear completely, when the antenna is excited perpendicular to its axis. Comparing the distance between each two spots with the length of the antenna in the SEM images reveals that the position of the bright spots match the physical extremities of the optical antennas. The fact that there are always two bright spots — though the second spot may be weak as in case of the antenna with length 140 nm — supports the existence of a resonant phenomena. If it were a *lightening-rod* effect, an accumulation of charges in the sharpest edge, then every single extremity of all optical antennas in Figure 3.9 should light up equally bright, which is not the case. The existence of the bright spots is clearly a function of the full antenna.

As it is very difficult to align the scanning tip such that the optical antenna is exactly parallel to the surface of the cover slip, all scanning tips are likely to be tilted to some degree. Any tilt results in an end of the optical antenna being further away from the fluorescent bead, thus an asymmetry in intensity of the two bright spots as measured in case of the antenna with length 140 nm should be expected.

An enlargement of the fluorescence maps of the antenna with a length of 170 nm is presented in Figure 3.10. The three-dimensional presentation of the fluorescence map shown in (a) provides a good impression of the quality of the observed fluorescence enhancement. The two fluorescence spots are clearly distinguishable with a good signal-to-noise ratio. Surprisingly

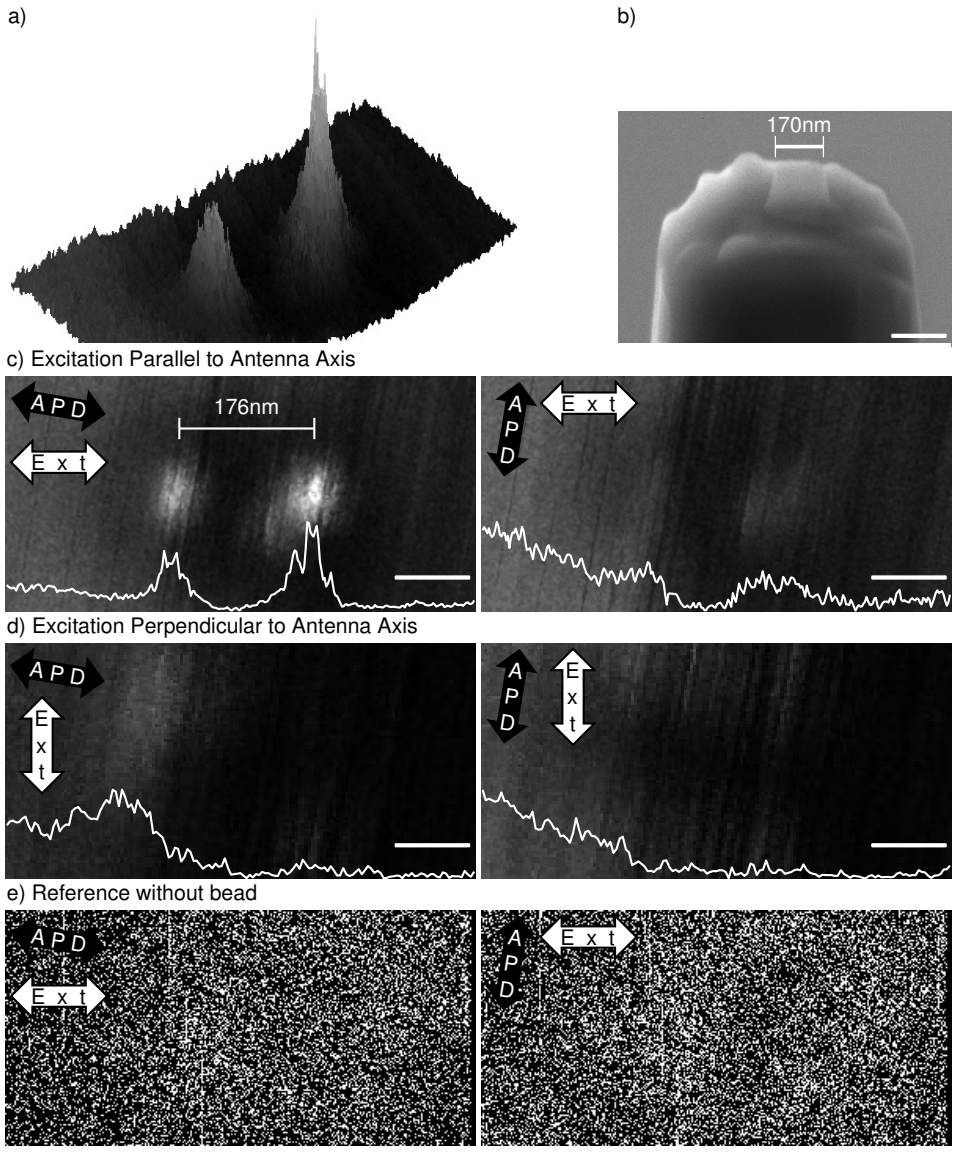

Figure 3.10: **The Resonant Optical Antenna.** The fluorescence map in (a) confirms the dipolar resonance of the antenna shown in (b). In (c), excitation and detection along the antenna axis reveal a separation of 176 nm between the bright spots, that matches the physical length of the antenna. With the detection perpendicular to the antenna axis as in the second map in (c) or excitation perpendicular to the antenna axis as in (d), no resonances of the antenna are seen. In (e), no bead is placed on the optical axis, thus contamination of the antenna with fluorescent particles can be ruled out safely. The scale bars are 100 nm long.

good is the agreement between the physical length of the optical antenna of 170 nm as extracted from the SEM image in (b) and the distance between the two bright fluorescence spots in (c) of 176 nm. This confirms that the bright fluorescence spots are indeed located at the extremities of the optical antenna. The other three fluorescence maps for a parallel polarised excitation but perpendicular polarised detection in (c), and for perpendicular polarised excitation in (d), as expected show no traces of enhanced fluorescence.

Not an Artefact by Attached Molecules. The fluorescence maps in Figure 3.10(e) were recorded without a fluorescent bead in the focus. They show the *auto*fluorescence arising only from the scanning tip with the optical antenna. A cause of artefacts can be that some fluorescent molecules attach to the optical antenna during previous scans. This may happen when either the polymeric matrix hosting the fluorescent beads is too thin or when the force the scanning tip exerts on the polymeric matrix with the beads is chosen too high. In either case, the fluorescent beads may come into physical contact with the tip, and some fluorescent material may attach to the optical antenna. As this attachment will happen predominantly at the extremities of the optical antenna, which statistically are the part of the antenna closest to the surface with the beads, the resulting fluorescence map is expected to have bright spots exactly at the extremities and effectively mimic a resonant optical antenna. Figure 3.10(e) shows a completely homogeneous however vanishing fluorescence profile, disproving the presence of fluorescent material on the optical antenna itself.

Calculations confirm the Optical Resonance. We performed comprehensive finite-difference time domain (FDTD) simulations to provide a more qualitative comparison with the experimental results. The employed simulation model has been sketched in Figure 3.5(b). Dipole sources with different orientations of their respective dipole momenta are buried 5 nm inside the glass substrate and scanned under the optical antenna. The optical antenna is 170 nm long, 65 nm wide, 60 nm high and its radius of curvature is 30 nm. An adhesion layer of 3 nm in thickness is assumed, and the glass socket has a height of 50 nm. The gap between substrate and antenna is 5 nm wide. A closed surface spun of field monitors records the total electric field at the optical antenna.

As previously discussed, in case of the first-order and third-order resonance, this numerically calculated situation of a dipole source exciting the antenna is equivalent to the experimental situation where the antenna excites the fluorescent bead. The second-order resonance must be treated

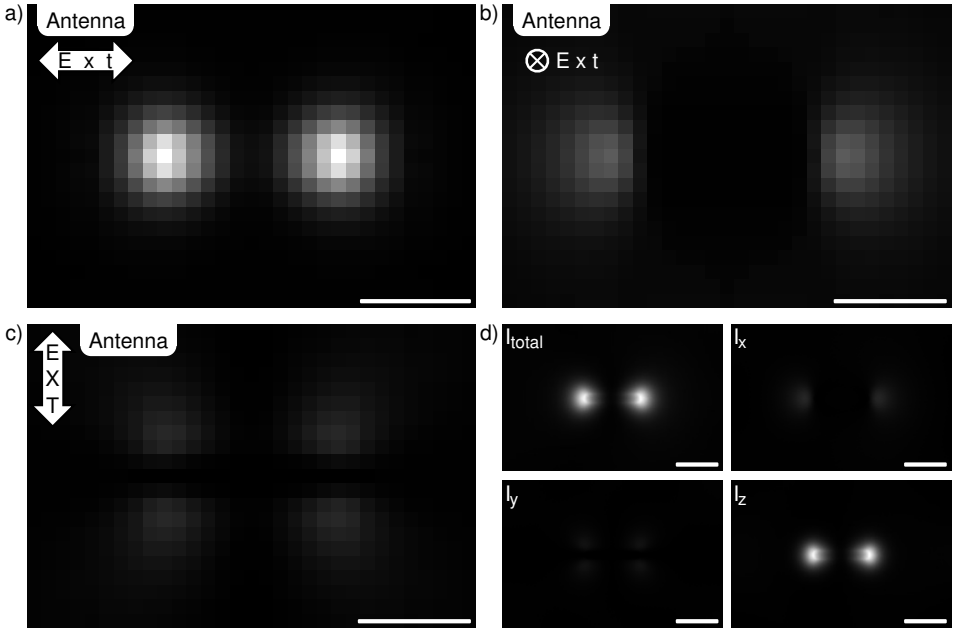

Figure 3.11: **Local Field Experienced by the Bead.** Dipole sources are scanned under the optical antenna as shown in Figure 3.5(b). Each pixel in (a), (b) and (c) corresponds to a separate calculation with the dipole source at the position of the pixel. The response of the antenna of 170 nm in length, the integrated electric field, is shown for a dipole moment (a) in-plane parallel and (b) perpendicular, and (c) out-of-plane to the antenna axis. The calculations are performed at the excitation wavelength of 647 nm. For odd-order resonances, this calculated situation is equivalent to an excitation of the bead through the antenna modes. In (d), all components of the electric field beneath the antenna are shown for an emitter position in the centre of the left bright spot in (a). All scale bars are 100 nm long.

differently as experimentally the antenna modes cannot be excited from the far-field at all.

Each pixel in Figure 3.11(a), (b) and (c) represents a separate numerical simulation with the dipole source at the position of the pixel. The dipole source is orientated (a) in-plane parallel and (b) perpendicular, and (c) out-of-plane perpendicular to the main axis of the antenna. The physical quantity visualised in these three sub-figures is the total electric field recorded on the closed surface for each simulation. In other words, the map shows how strongly the dipole source couples at each pixel to the modes of the optical antenna. Remarkable is the good agreement of the numerically calculated map with the experimental data presented in Figure 3.10.

The dipolar character of the optical antenna is confirmed by the plots of the electric fields in Figure 3.11(d). These images show the complete field under the antenna when the emitter is placed at the centre of the left bright spot in Figure 3.11(a). The field monitor that recorded the plotted electric field was indicated by the dotted line in 3.5(b) and is located inside the gap between substrate and antenna. Striking on the first view is the the predominance of an electric field polarised along the vertical z direction instead of the x direction along the driving dipole source. This has two reasons. First, the monitor starts to record the electric field only 25 fs after the excitation started. This ensures that the monitor captures the response of the antenna to the dipole source and not the orders-of-magnitude stronger excitation field of the dipole source. Second, the monitor is placed beneath the antenna, where the field of the optical antenna has simply gained a considerable component along z.

Size of Plasmonic Features. Gaussian fits to the fluorescence spots of the optical antenna with length 170 nm are provided in Figure 3.12. As a first observation, the Full Width at Half Maximum (FWHM) of each spot is roughly 10 nm larger perpendicular to the axis of the antenna than parallel. This is in accordance with the numerical data presented in Figure 3.11(a). As determined from SEM images, the physical width of the antenna has an upper bound at 65 nm, with the uncertainty justified by the margin in the interpretation of the SEM images. The FWHMs of 49 nm and 56 nm are slightly narrower than the physical width, which is very plausible.

The narrowest observed fluorescence spot has a FWHM of only 35 nm. The physical diameter of the fluorescent bead is specified as 20 nm by the provider. The width of the fluorescence spot is a convolution of the size the bead and the extent of the mode of the optical antenna interacting with the bead. The recorded FWHM of 35 nm is less than a factor two larger than the size of the field detector, the fluorescent bead, which is quite a

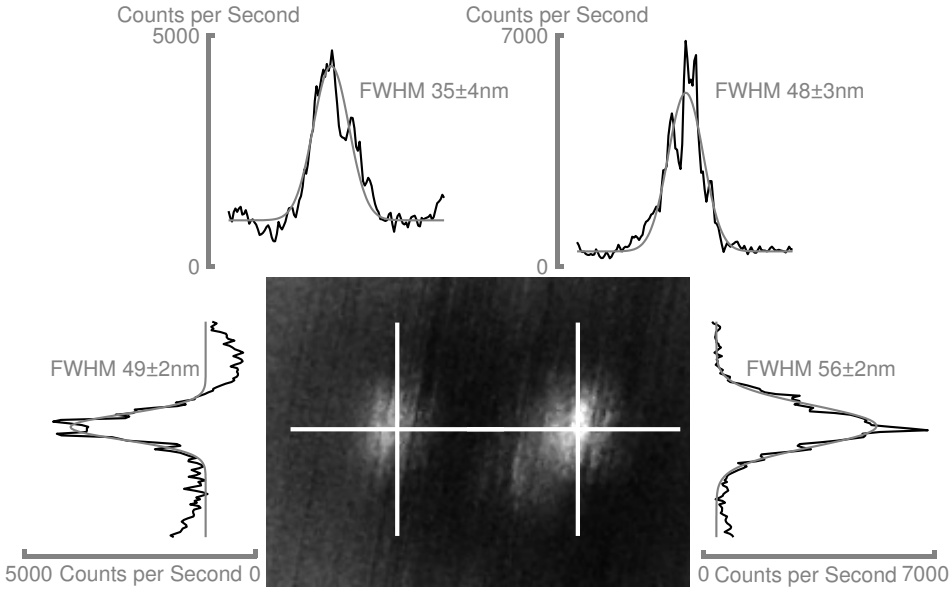

Figure 3.12: **Plasmonic features of 35 nm FWHM.** The fluorescence map belongs to the optical antenna of 170 nm in length, shown in Figure 3.10. The field probe, a bead of 20 nm in diameter, resolves spot sizes as small as 35 nm FWHM. The longitudinal spot widths are the smallest, with 35 nm and 48 nm FWHM, while the larger transverse widths of 49 nm and 56 nm are closer to the nominal width of the antenna of less than approximately 65 nm.

good result.

Resonances and Enhancement Mechanism of Dipole Antennas

In the previous two sections, maps of the fluorescence of a single bead scanned by different optical antennas have been presented. The presence of a resonant phenomenon is clear from Figure 3.9, where a dependence of the brightness of the two spots on the length of the optical antenna is observed easily.

However, it is still unclear whether the increase in fluorescence at the extremities of the antenna is due to a resonant enhancement of the excitation or the emission of the single bead. Were the former the case, the optical antenna would absorb energy resonantly from the far-field excitation and confine the energy at the extremities where the density of states is the highest. The bead is permanently excited by the far-field illumination, but, when positioned at the extremities, experiences an additional

excitation from the highly confined and enhanced field of the optical antenna. In this case, the angular emission of fluorescence from the bead is not modified.

In the latter case, the bead is excited by the far-field excitation, but couples resonantly to the optical antenna. The excited molecules within the bead decay into antenna modes and the angular emission becomes dominated by the antenna mode [28]. Now the angular emission pattern does change its shape.

There are several ways to answer this question. The shape of the angular emission pattern can be imaged directly with a sufficiently sensitive camera. A careful study of the resonant length of the antenna may reveal whether it is resonant with the wavelength of the excitation or the emission of the bead. The excitation of or coupling to even-order modes can be forbidden depending on the geometry of the fields. A forth option includes the behaviour of the polarisation of the detected fluorescence. However, it is very difficult to make a quantitative statement about the polarisation for several reasons, among them the arbitrary orientation of different optical antennas with respect to the polarisation of the two detectors. Also, the modulation the fluorescence experiences due to the proximity of the scanning tip is highly unpredictable. As the experimental set-up does not feature a sensitive camera, the two criteria remaining are the resonant antenna length and the symmetry properties of the excited and coupled modes.

The experimentally recorded enhancements of various optical antennas ranging from 100 nm to 580 nm in length are presented in Figure 3.13. Because of the aforementioned decrease of the detected fluorescence when the scanning tip is directly above the bead, the enhancement cannot simply be defined as the ratio between the magnitude of the fluorescence recorded with the scanning tip above and away from the bead. A normalisation to a non-resonant optical antenna must be implemented in order to compare different antennas. For practical reasons, a non-resonant optical antenna is at least equivalent to a resonant antenna under perpendicular polarised illumination. It may constitute even a better reference as fluorescence maps with two perpendicular polarisation of the excitation illumination are easily taken in comparably fast succession and the alignment of the set-up remains largely the same.

In this context, the enhancement will be defined as the ratio between the two count rates obtained under illumination polarised parallel and perpendicular to the optical antenna, $R_{\parallel}$ and $R_{\perp}$. As the intensity of the illumination is not equal in both polarisations, the count rates are normalised to the reference count rates in absence of the scanning tip, $R_{\parallel,\text{no probe}}$ and $R_{\perp,\text{no probe}}$:

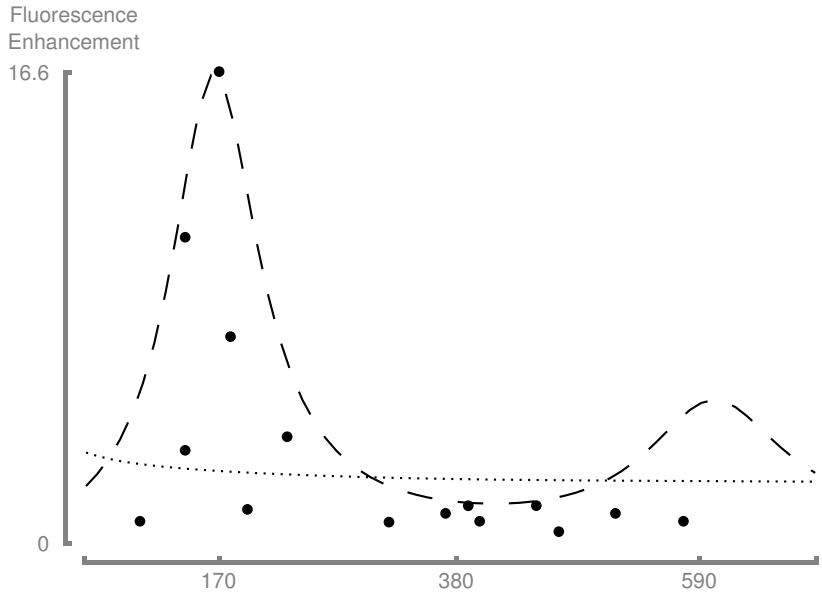

Figure 3.13: **A Resonance Curve of Optical Rod Antennas.** The black dots mark the experimentally recorded enhancement of the fluorescence in the vicinity of an optical antenna. The enhancement is defined as the ratio between the fluorescence count rate of a bead under a resonant and a non-resonant optical antenna. The dashed (dotted) line shows the result of numerical simulations for an excitation along (across) the axis of the antenna. The data for parallel excitation are fitted in amplitude to the experimental data. The first-order resonance matches well with the experimental data and the simulations, while the third-order resonance is not visible in the experimental data. The highest observed enhancement factor is 16.6×.

$$\text{Enhancement} = \frac{R_{\parallel}/R_{\parallel,\text{no probe}}}{R_{\perp}/R_{\perp,\text{no probe}}} \tag{3.1}$$

In Figure 3.13, scanning tips with an antenna length centred at around 170 nm show an enhancement of the fluorescence. At smaller and greater lengths of the optical antenna the enhancement stays at unity, marked by the black line. The fluorescence of the bead is amplified by as much as 16.6× by the most resonant antenna.

In an attempt to gain more insight into the mechanism of the enhancement, numerical simulations following the model used in Figure 3.5(a) were performed and their results are illustrated in Figure 3.13 by the dashed line for excitation along and by the dotted line for excitation perpendicular to

the antenna axis. The numerical calculations were performed at the wavelength of the exciting illumination, 647 nm, and are fitted in amplitude to the experimental data. The fitted numerical simulations agree well with the experimental data and confirm the presence of a dipolar resonance.

The difference between the excitation wavelength of 647 nm and the wavelength of 685 nm where the emission peaks is only 38 nm. This spectral distance corresponds to a change in length of the antenna of roughly 10 nm. This means that the dashed curve showing the numerical simulations would shift by 10 nm to longer lengths. With the available data and such a small shift, it is not possible to conclude the mechanism dominating the enhancement process by the resonant length.

However, the behaviour of the system must differ in the second-order resonance, depending on the mechanism. As this resonance cannot be excited with a flat phase front, excitation from the far-field is not possible. The bead will not experience an enhanced excitation. On the contrary, the emission of the bead can in principle couple to the antenna as it is a point-like emitter, lacking the flat phase front. As clearly visible in Figure 3.13, the second-order resonance does not show in the experimental data, thus it is the excitation that is resonantly enhanced by the antenna.

Even if a resonant coupling of the emission of the bead does occurs, it may be difficult to detect the coupling for this fluophore. As mentioned before, in order to couple the emission efficiently, the antenna length must be detuned by only 10 nm. A FWHM of the distribution of resonant antenna length of at least 40 nm can be read off Figure 3.13, well wider than the detuning. Also, only a fraction of the molecules contained in each bead will couple efficiently to the antenna, while the vast majority adds a fluorescent background.

3.4 Conclusion – A Viable Mapping Method

In this chapter, I have successfully demonstrated the spatial mapping of the modal distribution of an optical antenna and identified plasmonic features of 35 nm FWHM. The presented scheme is reliable and allows to conclude maps of different optical antennas accurately in form of a resonance curve. The observed enhancement in the fluorescence rate originates in an enhanced excitation field and not in a coupling of the emission field to the antenna modes.

The electromagnetic field was probed employing a fluorescent bead of 20 nm in diameter that was held fixed on a cover slip within the optical axis. The optical antenna was fabricated on a scanning tip and positioned deterministically and reversibly across the probing bead. The local strength

of the fluorescence signal of this bead, taken as a measure of the strength of the local field of the antenna, has proven to give an accurate map of the modal distribution of the antenna modes. An excellent agreement of experimental data, numerical calculations and theory was reached.

An enhancement in the fluorescence rate due to coupling to antenna modes was not observed for this specific bead in our experiments.

Correcting the recorded fluorescence spots under the optical antenna by the fluorescence of the bead in absence of the scanning tip, the resonance curve containing the experimental enhancement factors of different optical dipole antennas reflects well our numerical simulations.

In the past, many schemes of near-field mapping of optical antennas and photonic nanostructures have been proposed. However, in the authors' opinion, the demonstrated approach avoids most of the problems of previous schemes, while offering a superior resolution and reproducibility. Imaging artefacts by the proximity and geometry of the scanning tip are not overly critical, because the local environment of the optical antenna remains invariant during the experiment. Only the optical antenna itself is in direct contact with the cover slip and the beads due to the presence of a glass socket. On the contrary, for standard NSOM, any topographic feature anywhere under the aperture probe induces artefacts, as does the presence of a large aluminium-/-silica probe surface itself. The proposed scheme avoids any chemical or electrostatic attachment of a particle, which is hardly a controlled technique. Some few years ago a valid point would have been the challenge of fabricating a complex structure at the end face of a sharp scanning tip. However, nanofabrication is a rapidly evolving technology. Today's FIB systems can do exactly this lithographic fabrication in a very controlled and reproducible manner and are available in more and more laboratories.

The major challenge lies rather in the experimental set-up, because the success of this method is limited by its tolerance to tilt. If the end face with the nanostructure is tilted with respect to the surface of the cover slip which defines the scanning plane, parts of the nanostructure will be further away than others from the field probe. The consequences include an exponential deviation of the strength of the fluorescence due to the strong decay of the near-field and an apparent spatial broadening of the localised field. As the scientific interest necessarily shifts to more complex and likely larger nanostructures over time, the impact of both these problems will simultaneously increase.

4 Waveguide-Resonance Extraordinary Optical Transmission

While optical antennas efficiently link freely propagating radiation to small objects, a localised field can be guided between two arbitrary adjacent nanostructures by near-field coupling. Similar to the coupling between an optical antenna and e.g. a molecule, the matching of the impedances between the two arbitrary nanostructures is a critical factor for the efficiency of their coupling. Here we link a waveguide to a single subwavelength aperture in a gold film by matching their respectice impedances. We observe a resonant increase in transmission through the aperture. In resemblance to Extraordinary Optical Transmission (EOT), we call this phenomenon *Waveguide-Resonant Extraordinary Optical Transmission* (WR-EOT). The impedances are matched by tapering the waveguide. As the impedance to a mode depends on the local diameter of the taper guiding the mode, an aperture placed at the correct axial position is impedance-matched for a certain wavelength.

An introduction into the principles and concepts of WR-EOT is found in Section 4.1. The following Section 4.2 covers the fabrication of the aperture coupled to a tapered waveguide and the experimental set-up. The experimental results and a comparison with numerical calculations are found in Section 4.3. Section 4.4 concludes the chapter.

4.1 An Introduction to Coupled Sub-Wavelength Apertures

In the previous Chapter 3, we have mapped the electric field of a single metal rod acting as an optical antenna. We have shown how already this simple rod confines and enhances thus controls optical radiation on the nanometre scale. More complex and purposefully designed nanostructures and arrangements promise to improve the control and to address different properties of optical radiation. In this chapter, a coupled tapered waveguide improves the transmission through a single sub-wavelength aperture.

Complex Nanostructures. Two adjacent and identical objects may couple through near-field interaction. They may provide a strongly enhanced and confined field in the space between them. Examples include two identical rods [38, 41], triangles [22, 44–46], spheres [67, 127–129] or cylinders [130]. Three or more objects of equal or similar geometry may introduce e.g. directivity. For example, a chain of particles [67, 131, 132] or rods [29, 39, 40] may couple in such a way that the emission and absorption of optical radiation is only allowed from very specific angles.

While so far identical or at least objects of the same class were coupled, also two entirely different objects may expose interesting and useful properties. A spherical object or molecule interacting with an infinite surface may experience a modification of its angular emission properties [126, 133]. Similar observations have been made for a system of several coupled spheres [134]. A sphere coupled to a spherical cavity provides strong field enhancement at the interface between both [135]. Concentric rings, so-called *bulls eye* [50, 136], may add directivity to any emitting object in its centre. A single aperture smaller than the wavelength of the incident light hardly transmits any radiation. Its transmissivity changes dramatically when coupled to and feed by a suitable second nanostructure. Imura et al. improved the transmission with a single, resonant disc, placed in front of the aperture [137]. In this chapter, we show how a coupled tapered waveguide effects the transmission.

Coupled Single Sub-Wavelength Apertures. The anomalous transmission through a sub-wavelength aperture is generally referred to as *Extraordinary Optical Transmission* (EOT). The transmission is anomalous with respect to what is predicted by Bethe's original theory on the transmission of small holes [4]. Ebbesen et al. described EOT for the first time for an array of apertures in an infinite screen [138, 139]. Bethe's theory which was originally developed for single apertures in a cavity or waveguide was

subsequently extended to arrays of sub-wavelength apertures [140,141]. Initially it was believed that a superposition of surface plasmon polaritons in the periodic array of apertures was responsible for the extraordinary transmission. However, EOT has also been reported on dielectric surfaces [142] and at millimetre-wave frequencies [143]. Surface plasmon polaritons are not supported in any of the two situations.

The physical mechanism for EOT is based rather in the existence of a single transverse magnetic (TM) mode. This mode is at its cut-off and bound to the surface with the apertures [140, 144, 145]. The decisive property of this TM mode at cut-off is a diverging magnetic field component. In Bethe's theory, the mechanism of the transmission is formulated as an infinitesimal magnetic polarisation current at the aperture [4]. The diverging magnetic component couples to the magnetic current of the aperture and links the aperture very efficiently to the incident radiation. The energy then traverses the sub-wavelength aperture and is re-radiated on the opposite site.

The TM mode is bound to the surface and thus an evanescent wave away from the metal film with the aperture. The mode resonantly builds up the energy of the incident radiation near the surface with the aperture, similar to a resonator. The stored and resonantly enhanced radiation has a high probability of being re-scattered into the aperture which increases the transmission probability. This phenomenon is similar to EOT in aperture arrays [138]; except here only a single aperture is required.

An equivalent formulation considers the transmission phenomenon as a problem of impedance matching [68, 69, 146–149]. A sub-wavelength aperture has a certain impedance. A TM mode experiences an impedance that depends on how near this mode is to its cut-off. The efficiency of the coupling is given by how well these two impedances are made to match.

The challenge is to find a suitable nanostructure that provides a TM mode near its cut-off with the correct impedance. Also, this nanostructure must be placed sufficiently close to a sub-wavelength aperture in order to interact in the near-field.

Coupling a Tapered Waveguide to an Aperture. The impedance of a waveguide to a certain mode is a function of how well a mode 'fits' into the waveguide. The relevant parameters are the indices of refraction and the dimensions of the waveguide and the spatial extent of the mode.

A tapered waveguide features a continuously decreasing diameter of the volume where a mode is guided. The mode experiences a decline in the guiding qualities of the waveguide to the point that is ceases to propagate. Therefore, a mode experiences a local impedance that depends on the local

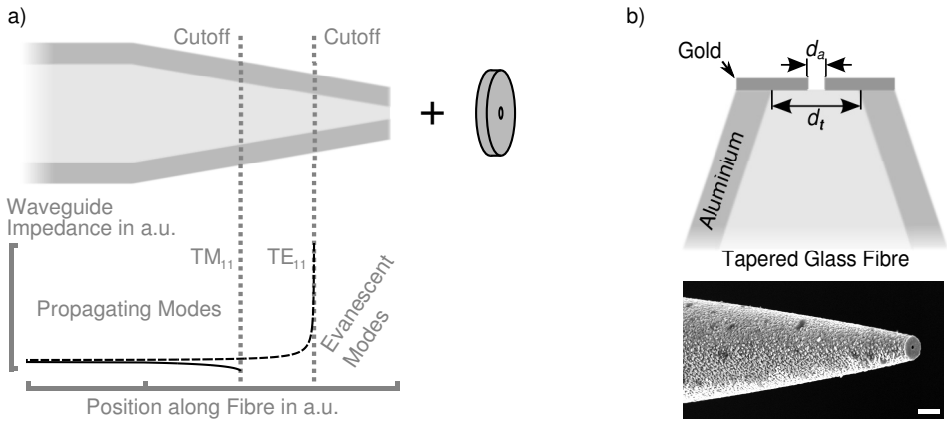

Figure 4.1: **WR-EOT in a Tapered Waveguide.** (a) The waveguide impedance of a mode in a tapered fibre waveguide changes drastically when the diameter of the waveguide approaches the diameter of the mode volume. A single aperture can be impedance-matched to the waveguide by moving it along the waveguide. (b) The sketch and the SEM image show the coupled system designed to measure WR-EOT. The scale bar is 1 μm long.

diameter of the waveguide [148, 149]. If the diameter of the waveguide goes beyond a threshold, cut-off of this mode is reached and the impedance diverges. The relation between the wavelength at which cut-off occurs and associated waveguide diameter for a TM_{11} mode is given by [148]

$$\lambda_c = \frac{\pi d_t n_f}{3.832} \tag{4.1}$$

for a perfect electric conductor. d_t is the final taper diameter, n_f the refractive index of the waveguide and λ_c the cut-off wavelength. Therefore, if an aperture is placed at a unique axial position along a tapered waveguide, the impedance of the waveguide is matched to the impedance of the aperture for a certain wavelength of the incident radiation.

So far, *Waveguide-Resonant Extraordinary Optical Transmission* (WR-EOT) has only been demonstrated for coupling between two perfectly conducting waveguides and in the microwave regime [150]. Here, we demonstrate a nanoscale version WR-EOT providing enhanced transmission at visible to near-infrared wavelengths.

Above equation was suggestively formulated for the TM_{11} mode for a reason. The proposed coupled system is sketched in Figure 4.1. It is a fully rotationally symmetric system, in which the TM_{11} mode is the lowest order mode that allows for concentric apertures. As demonstrated in Figure

4.1(a), the impedance of the modes depends strongly on the local diameter of the taper. The impedances diverge approaching mode cut-off and only evanescent waves are allowed past the cut-off.

The sketched cross cut in Figure 4.1(b) demonstrates how the waveguide is coupled to the aperture. The waveguide itself consists of a piece of tapered optical fibre that is cut at a certain diameter. This diameter is chosen to yield a resonance at a desired wavelength and is approximated by Equation 4.1. The aperture is fabricated into a structural gold layer directly on the end face. This ensures an optimal coupling between the aperture and the tapered waveguide. We expect the major contribution to the spectral position of the resonant coupling to come from the final taper diameter d_t. Therefore, the diameter of the aperture d_a will remain a constant in the experiments.

Two observations will have to be made in order to demonstrate the presence of a resonant coupling between waveguide and aperture. First, a peak in the transmission must be recorded and its linear dependence on the final diameter of the taper established. Second, the involvement of the TM_{11} mode in the enhance transmission must be verified.

4.2 The Fabrication of the Probe and the Experimental Set-ups

In the previous section it was established that a tapered waveguide will be coupled resonantly in the near-field to a single sub-wavelength aperture. The realisation of such a coupled probe is discussed and demonstrated in this section. Also the experimental set-ups and the steps taken to avoid artefacts are illustrated here.

The Fabrication of the Waveguide-Coupled Aperture

The design of the coupled system has already been sketched in Figure 4.1(b). In this section, the fabrication of such a tapered waveguide and such a sub-wavelength aperture are described.

The waveguide is simply a commercial optical fibre. The fibre is tapered by heat-pulling (see Section 2.2). The very end of the tapered fibre now has a diameter of approximately 100 nm, such that any final taper diameter larger than 100 nm can be realised. As the focus lies on measuring light transmission from the aperture, sources for spurious background radiation must be removed. Therefore, the outside of the fibre waveguide is coated with a layer of 220 nm of aluminium which is considered sufficiently thick to prevent light leakage (see Section 2.2).

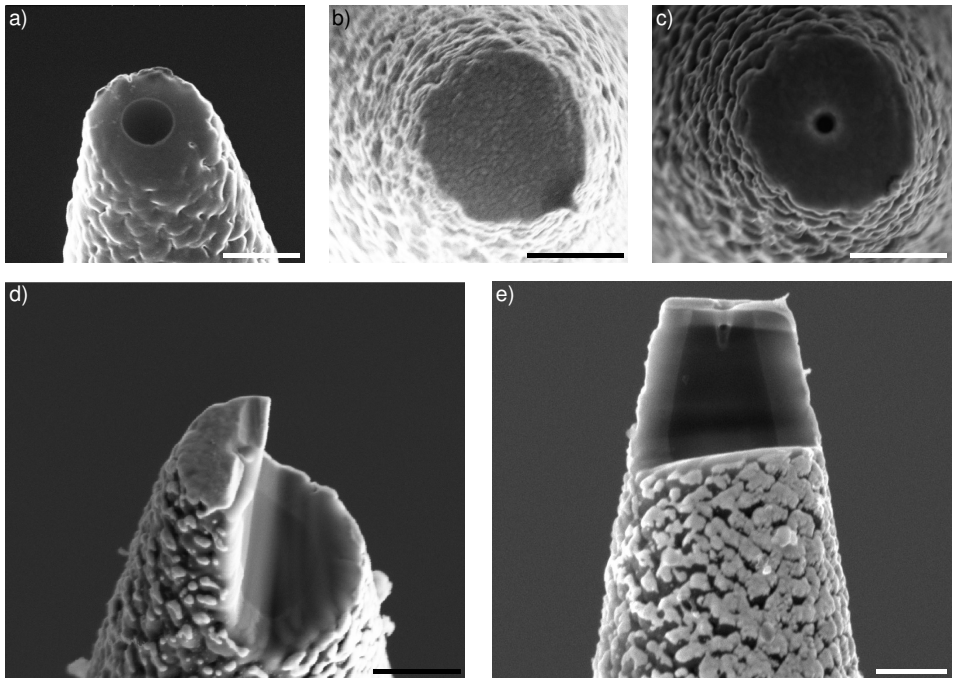

Figure 4.2: **Steps in the Fabrication.** After the desired final taper diameter is established by FIB milling in (a), the end face is coated with a layer of 90 nm of gold in (b). The final aperture is milled by FIB and kept at a diameter of 110 nm. (d) and (e) show cross sections of a typical probe. Distinguishable are the tapered core of glass, the thin layer of gold and the aperture. All scale bars are 500 nm long.

The wavelength at which the cut-off of the TM_{11} mode occurs is determined by the final diameter of the tapered waveguide, d_t, in Figure 4.1(b). This diameter must be very carefully adjusted to the desired wavelength. An FIB system (see Section 2.3) is used to define this diameter and to remove the apex of the tapered fibre waveguide. Figure 4.2(a) shows the probe after this fabrication step.

The next fabrication step is shown in Figure 4.2(b). A gold film of 90 nm in thickness is deposited on the end face. This is the structural layer in which the aperture will be milled. The choice of gold as the material for the end face was motivated by its favourable optical properties in the red and infrared, where our optical measurements were carried out, and the favourable fabricational properties (see also Section 2.2)

In a final step, a single sub-wavelength aperture with diameter d_a (see Figure 4.1(b)) is milled into the gold layer, nominally at the centre and

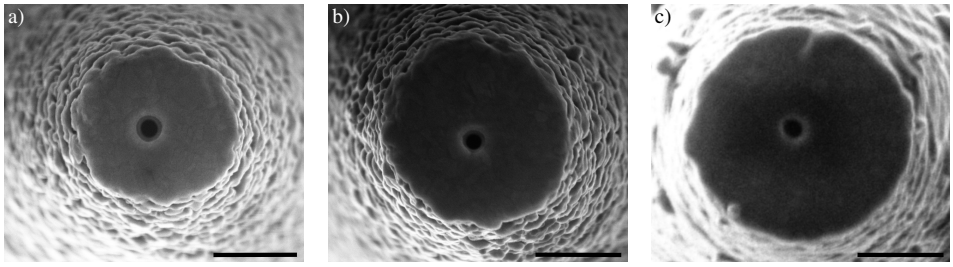

Figure 4.3: **Different Final Taper Diameters.** As the resonance depends critically on the impedance of the waveguide and thus the final taper diameter, probes with diameters as different as e.g. (a) 420 nm, (b) 525 nm and (c) 724 nm were realised. The diameter of the apertures is kept constant at 110 nm. All scale bars are 500 nm long.

with a variance of 30 nm in placement. Figure 4.2(c) shows an SEM image of the fibre waveguide with the aperture. The size of the aperture is chosen as 110 ± 10 nm and will be held constant for probes. Calibration of the milling process ensured that the aperture was milled through the gold layer only and not overly into the glass fibre core. This avoids possible spurious effects on the resonance [151].

Figures 4.2(c) and (d) show cross-sections of the probe. Clearly visible are the dark glass core of the tapered fibre waveguide and the aluminium and gold films. The aperture was milled slightly into the glass core. This indicates that the applied dose of the ion beam was chosen too high.

In Figure 4.3, waveguide-aperture probes with different final diameters of the tapered waveguide are presented. The different diameters of 420 nm, 525 nm and 724 nm are reflected in the increasing total diameter of the probe that includes the aluminium film. 420 nm and 724 nm mark the lower and upper bound to the range of diameters fabricated. The apertures of the probes are kept invariant within fabrication margins.

The reverse configuration, with the final taper diameter kept invariant and the aperture diameter changed, is demonstrated in Figure 4.4. For the experiments covered in this chapter, a diameter of 110 ± 10 nm was aimed at, which is achieved repeatably and reproducibly. The display of larger and smaller diameters shows the control exerted on the fabrication process.

As the optical characteristics of metals can differ substantially, we fabricated the devices with both gold and aluminium as the structural layer at the end face. Figure 4.5(a) and (b) show a probe in an aluminium / aluminium configuration and (c) and (d) in an aluminium / gold configuration (side coating / structural layer at end face).

As clearly shown in this section, we were able to fabricate tapered wave-

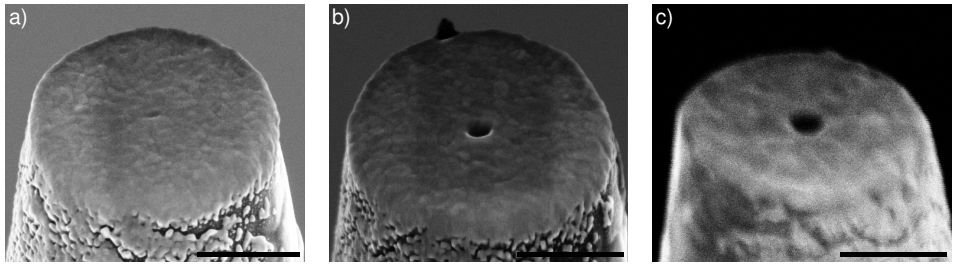

Figure 4.4: **Different Aperture Diameters.** Apertures with different radii are milled to demonstrate the accuracy of the fabrication. The apertures have diameters of (a) 57 nm, (b) 106 nm and (c) 150 nm and the final taper diameter is held constant. All scale bars are 500 nm long.

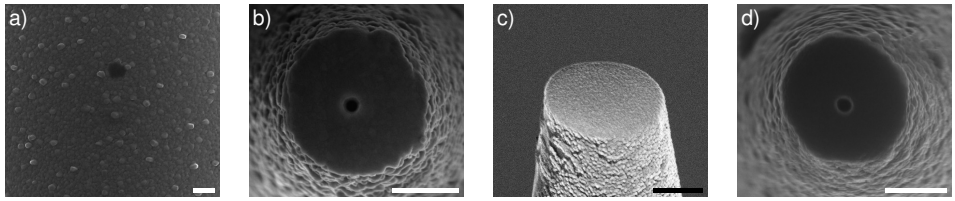

Figure 4.5: **Structural Layers of Different Materials.** The probe was realised in different material compositions. (a) and (b) show fully aluminium-coated and (b) and (c) hybrid aluminium / gold probes. (a) and (c) reveal the quality of the structural layer. The final configuration is shown in (b) and (d). All scale bars are 500 nm long.

guides with sub-wavelength apertures. The tolerances in the fabrication process are acceptable and a range of different final taper diameters was successfully fabricated.

The Experimental Set-Ups

We designed two experimental configurations to record both the in-coupling collection and the out-coupling transmission spectra of the waveguide-coupled aperture. Two light sources with different properties, a supercontinuum source and a thermal source, were employed in the experiments.

The experimental configuration for the out-coupling transmission spectrum is sketched in Figure 4.6(a). The supercontinuum light source is the brightest source available. However, its spectrum fluctuates rapidly and strongly in amplitude and slightly in frequency. In order to record a reliable transmission spectrum of the waveguide-coupled aperture, the spectrum of the source and its dependencies have to be observed carefully.

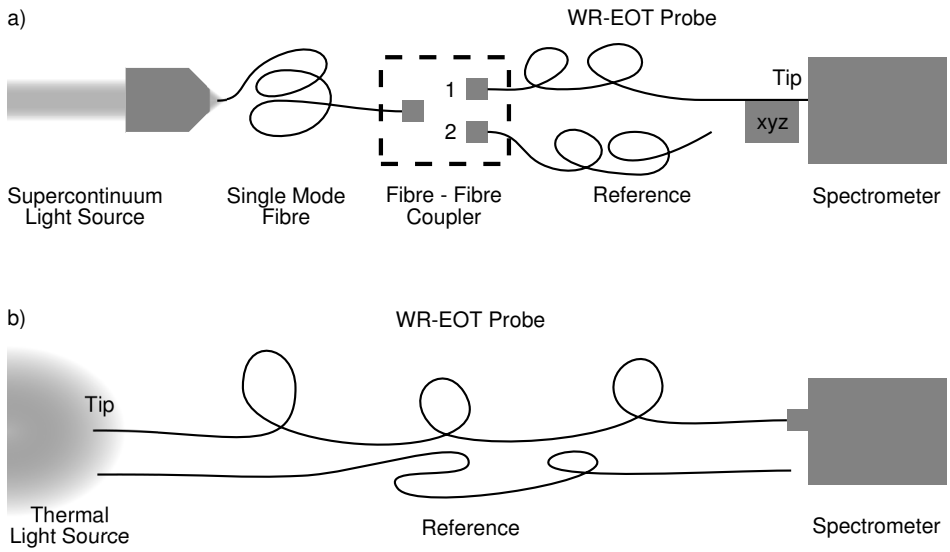

Figure 4.6: **Experimental Set-ups for Recording the In- and Out-coupling Collection and Transmission Spectra.** (a) The WR-EOT probe and a reference are placed in the entry slit of a sensitive spectrometer and the out-coupled light is spectrally analysed. The supercontinuum light source is coupled into an additional fibre, such that a constant, non-fluctuating spectrum is provided to probe and reference. (b) The in-coupling spectrum is measured with a thermal light source that provides a stable but shorter spectrum.

We address this issue by placing an additional single mode fibre between the supercontinuum source and probe and reference. This fibre is connected rapidly to either probe or reference by dedicated fibre-fibre couplers. This procedure guarantees that the spectra of probe and reference can be recorded in very quick succession. There is no need to change the coupling of the supercontinuum source itself.

The reference is a fibre of equal length and material as the WR-EOT probe. Recording a reference spectrum guarantees that the spectra can be corrected for the spectral properties of the fibre itself.

A translation stage with three axis allows a fine-positioning of the aperture in the entrance slit of the spectrometer. A laterally incorrect position leads to a spectral shift of the spectrum and was corrected using a reference laser with a known wavelength. An axially incorrect position reduces the strength of the signal and was corrected by adapting the axial position until the signal was maximised. For the reference fibre and for both reference fibre and WR-EOT probe in the configuration for the thermal light source,

the end plugged into the spectrometer was equipped with a fibre connector and therefore automatically in the correct position.

Using a thermal light source to reassess the spectra recorded under illumination by the supercontinuum source has two reasons. First, the supercontinuum source fluctuates strongly, so the spectra were reassessed using the more stable however spectrally narrower thermal illumination. Figure 4.6(b) shows how the in-coupling collection was recorded with the thermal source.

Second, recording the spectra for a probe in both configurations answers the question whether the angular collection and emission characteristics of the single aperture are adequately accounted for. As the aperture is almost a point-like source, an emission into 2π is expected. The emission pattern is rotationally symmetric but azimuthally inhomogeneous. However, the spectrometer has only a limited NA of 0.1 such that not all emitted radiation is captured. In the collection configuration light the aperture is excited from a different set of angles. If the angular collection and transmission characteristic of the probe play a significant role, then the two recorded spectra will differ strongly.

4.3 Results — Resonant Coupling of Aperture and Waveguide

The presented results prove that the tapered waveguide and the aperture couple resonantly. In the first section, the recorded spectra show the predicted increase in transmission at resonance. Experimental results and numerical calculations illustrate the importance of the TM_{11} mode in the second section. Numerical calculations in the third section demonstrate how the field energy is concentrated at the inner interface near the aperture.

Spectra and Wavelength Dependence on Taper Diameter

The first set of experiments aim at establishing the presence of a resonant coupling between tapered waveguide and aperture. A coupling will manifest itself as an increase in transmission at the resonant wavelength.

The two experimental set-ups described in Section 4.2 and Figure 4.6 allow to record reliable and meaningful optical spectra between the wavelengths of 500 nm and 950 nm. Preliminary numerical simulations suggest that these optical wavelengths correspond to waveguide probes with final taper diameters of between about 400 nm and 750 nm.

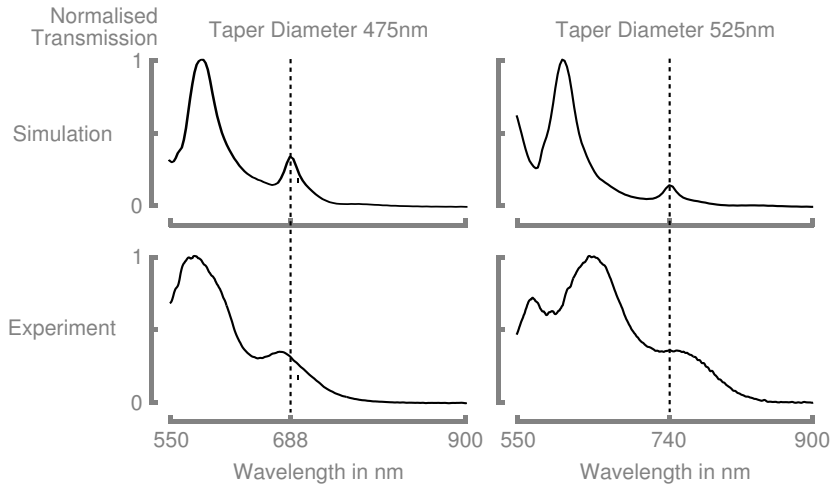

Figure 4.7: **Spectra of WR-EOT Probes.** The peaks attributed to WR-EOT are marked by the vertical dashed line. As this resonance is connected to mode cut-off, no modes can propagate at longer wavelengths and the spectra remain flat. The numerical simulations in the upper row agree well with the experimental spectra in the lower row.

Experimentally recorded spectra of two probes and corresponding numerical simulations are shown in Figure 4.7. The probes have final taper diameters of 475 and 525 nm and were excited by the supercontinuum light source. As a first observation, experimental and numerically calculated spectra roughly agree in the number of peaks of transmission and their respective spectral position.

The simulations exhibit slightly sharper features than the experimental spectra. Small ellipticities of the aperture may be a reason that are inevitable during fabriation. The spectrum of an elliptical aperture depends on whether the incident radiation was polarised along the short or long axis. As the polarisation is not controlled in the experiment, a spectral broadening is the consequence.

Well-reflected in the calculations is also the decay of the transmission to longer wavelengths. Here, the spectra remain flat and featureless. The resonant wavelength corresponds to almost cut-off of one of the lowest order modes. In other words, no mode at longer wavelength can propagate further. The transmission peak at the longest wavelength is expected to correspond to mode cut-off relevant for WR-EOT. As such, we expect the resonant wavelength to depend on the final taper diameter.

This assumption is confirmed as an almost linear dependence between final taper diameter and peak position is clearly visible in Figure 4.8. Each

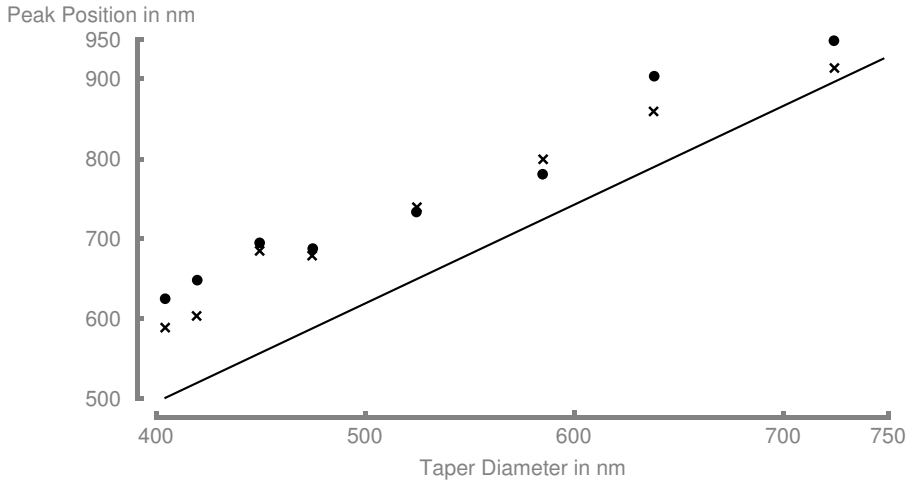

Figure 4.8: **Dependence of the Transmission on the Final Taper Diameter.** The experimentally recorded data, marked by crosses, show a linear dependence of the transmission on the final taper diameter. They agree well with the results of our numerical calculation marked by dots. Indicated by the black line is the cut-off wavelength corresponding to a TM_{11} mode as predicted by equation 4.1 for a perfect electric conductor.

WR-EOT probe shows a distinct peak in transmission that shifts to longer wavelengths with increasing final diameter of the taper. Our numerical calculations show a good quantitative agreement with the measurements in the location of the resonances. The slight discrepancy can be explained by the error in determining the exact final taper diameter from the SEM images. The material composition of the dielectric fibre core and the conductive aluminium film causes artefacts at the interface that makes the radius hard to determine.

The black line in Figure 4.8 marks the spectral position of the resonant coupling for a perfect electric conductor as predicted by Equation 4.1. The prediction shows an offset to shorter resonant wavelengths or, equivalently, to longer final taper diameters. The offset is due to the finite penetration depth of optical fields into real metals. This effect enlarges the effective diameter of the mode-guiding area and the aperture compared to perfect electric conductors.

A waveguide effectively acts as a filter for particular modes and wavelengths and has its own spectrum. Whether a mode is guided or strongly suppressed is a function of the material composition and geometry of the waveguide. Here, we have been using single mode fibres designed for operation at a wavelength of 633 nm. For a true single mode operation and

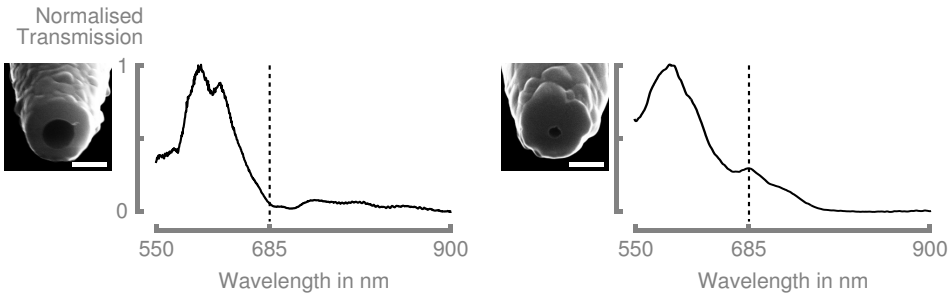

Figure 4.9: **Origin of the Transmission Peak.** A tapered waveguide supports only selected modes according to its geometry and thus has its own spectrum, shown on the left. The spectrum of the same waveguide now coupled to an aperture is shown on the right. Numerical calculations predict a resonant coupling at 695 nm. The two spectra differ in the presence of a peak exactly at that position. Therefore, WR-EOT is an effect of the coupling between waveguide and aperture. All scale bars are 500 nm long.

sufficient suppression of all other modes, the fibre must be at least several meters long. However, we used probes of only 20 nm in length that are tapered in addition. As a result, the transmission spectrum of the waveguide itself is unknown. The experimental data and conclusions illustrated in Figures 4.7 and 4.9 may be an intrinsic consequence of the employed waveguide rather than the coupling.

We demonstrate conclusively in Figure 4.9 that the observed peaks in transmission are a function of the coupling indeed. According to numerical calculations and an interpolation of the experimental data in Figure 4.8, the resonant coupling of this particular WR-EOT probe is predicted at a wavelength of 695 nm. The left spectrum was measured before the structural layer was deposited on the waveguide. It thus shows directly the transmitted spectrum of the waveguide, including all modulation induced by the taper. There is clearly no peak in transmission close to 695 nm. Now, the structural layer is deposited and the sub-wavelength aperture milled. A new peak appears at a wavelength of 685 nm, in good agreement with the predicted spectral position. Therefore, the peaks in transmission at the longest wavelengths are indeed result of a resonant coupling between the tapered waveguide and the single sub-wavelength aperture.

We have achieve similar results using the thermal light source. However, the thermal source is much weaker especially at longer wavelengths. The spectra shown here were acquired using the stronger and broader supercontinuum light source.

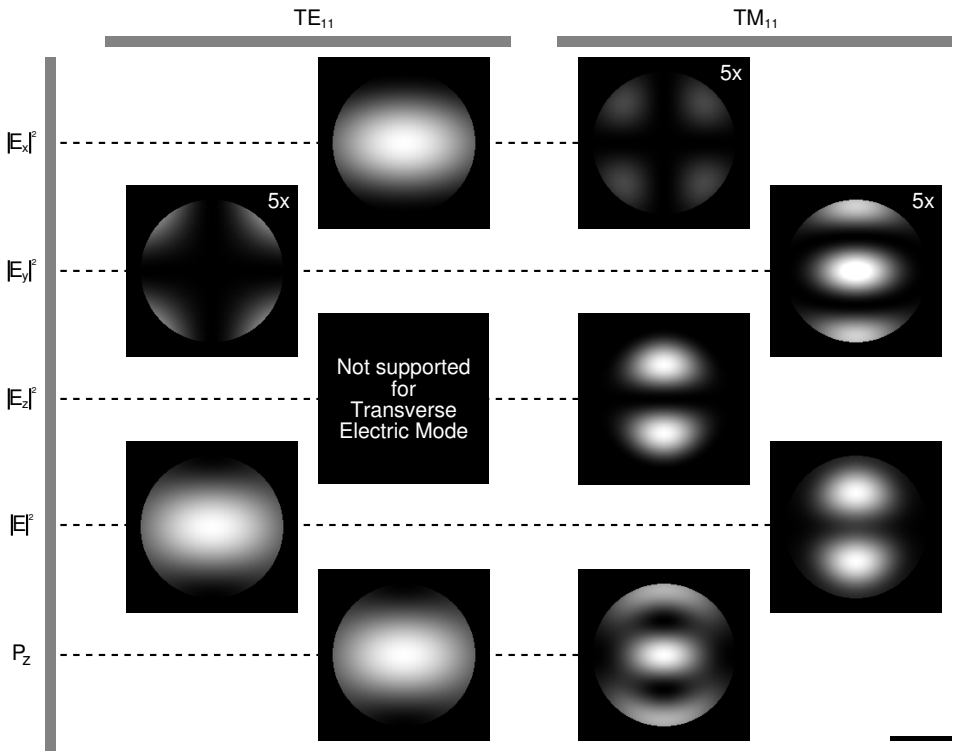

Figure 4.10: **Analytical Solutions for the TE_{11} and TM_{11} Modes.** The two modes expose very characteristic shapes inside the circular waveguide. The Poynting vector of the TM_11 mode shows a strongly confined flux of field energy in axial direction at the centre where also the aperture is located. The scale bar is 200 nm long.

In conclusion, the experimental data prove the existence of a resonant coupling between waveguide and aperture. The numerical simulations reflect the observations well.

The Role of the TM_{11} Mode

As mentioned in the introduction, the resonant coupling is ascribed to a lower-order TM mode in the tapered waveguide. In this section, we show experimentally and numerically that indeed the TM_{11} mode prevails near the aperture region of the waveguide.

The TE_{11} mode is the dominant mode guided inside the non-tapered part of the waveguide. To verify the existance of a TM mode near the aperture, the TM mode must be discriminated against the TE_{11} mode. Figure 4.10 presents analytical solutions of the electric field components

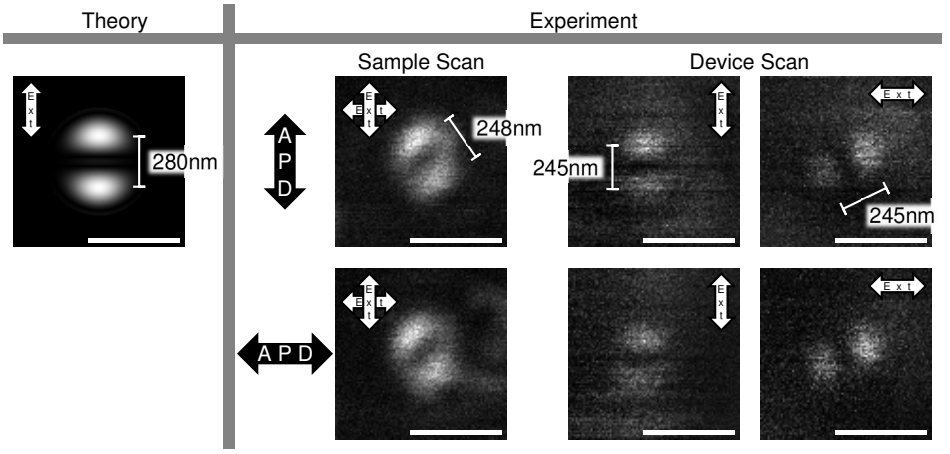

Figure 4.11: **Experimentally Mapped Mode Profile.** The probe without structural layer is scanned across single molecules in a Near-Field Scanning Optical Microscope (NSOM) and the fluorescence recorded. This spatial map reflects the shape of the mode inside the fibre. The analytical solution of a TM_{11} mode agrees well with the experimentally recorded maps for different polarisations and different scan configurations. The scale bars are 500 nm long.

and the Poynting vectors of the TE_{11} and TM_{11} modes. Both modes are clearly distinguishable on the base of their characteristic field distributions. Most notable is that the total intensity of the TE_{11} mode is confined to a broad single peak in the centre of the waveguide. In contrast, the TM_11 mode shows a double peak. In case of the Poynting vector along the axial direction, the TE_{11} transports the field energy in a broad central area. The TM_{11} confines the energy to a very small region in the centre of the waveguide. Here the aperture will be located.

An experimental confirmation of the prevalence of the TM_{11} mode is demonstrated in Figure 4.11. The WR-EOT probe is technically very similar to an NSOM probe. As such its field can be mapped by scanning the WR-EOT probe across single molecules. Similar to the mapping of optical antennas in Chapter 3, the magnitude of the fluorescence reflects the magnitude of the electric field. We are interested in the field that arrives at the structural layer with the aperture. Therefore, the measurements are pursued before deposition of the structural layer.

Figure 4.11 includes data taken in two different configurations. In the sample scan, the WR-EOT probe is held fixed on the optical axis, while a single molecule is scanned beneath. In the probe scan, the molecule is held fixed on the optical axis and the probe scans across. In both cases,

the molecule is excited directly through the field of the waveguide modes.

As clearly visible, the experimentally mapped fields correspond well in shape and dimension to the analytically calculated field distribution. The prevalent mode at the end of the tapered waveguide is indeed the TM_{11} mode.

Energy Distribution Inside the Waveguide

While the field distribution at the end of the waveguide can be mapped experimentally, numerical calculations are the only mean to determine the field distributions along the waveguide. For the calculations presented in Figure 4.12, a broadband mode source with the profile of a TE_{11} mode and polarised along x was launched into the waveguide. Several monitors record the electric and magnetic fields. Perfectly matched layers were placed at the open end of the waveguide to avoid spurious reflection effects. The field plots show only the relevant field components. The components other than E_x, E_z and H_y are at least an order of magnitude weaker or equal zero and do not contribute.

The field plots in the left column of Figure 4.12 clearly show the strong concentration of the electro-magnetic field near the aperture for a wavelength of around 710 nm. At this wavelength the resonant coupling is expected to occur for this WR-EOT probe. For E_x and H_z, the field energy is confined to the interior of the aperture on the side of the waveguide. Two bright spots appear next to the aperture for E_z. These also show in the fields monitored perpendicular to the axis of the probe and displayed in the upper right.

Plotted in the lower right is the total energy density of the electromagnetic field at 10 nm above and below the resonant wavelength. The field is integrated across the waveguide and normalised to the respective cross section. Energy densities at distances shorter than -10 nm to the aperture are not shown as computation artefacts become dominant here. The plot shows an exponential increase in energy density towards the aperture at the resonance frequency.

The field plots stress the importance of the TM_{11} mode at cut-off to the mechanism of WR-EOT.

4.4 Conclusion – Extraordinary Transmission

When a sub-wavelength aperture is fabricated into a tapered waveguide of a certain diameter, we observe an increase in the transmission through the aperture. The increase is due to a resonant coupling of the tapered waveguide to a single sub-wavelength aperture. The resonant coupling relies on

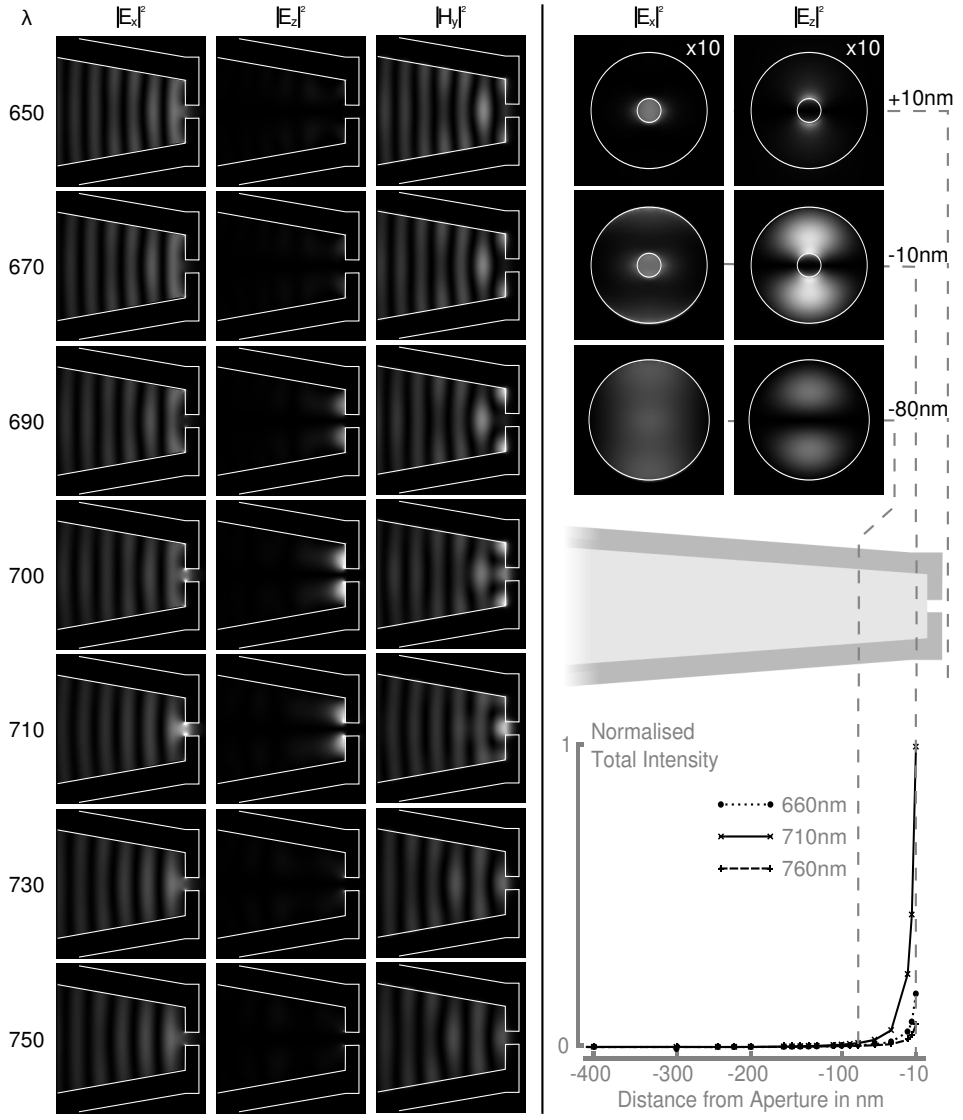

Figure 4.12: **Calculation of Field Components Inside the Waveguide.** Left column: The field distributions near the structural layer show a strong dependence on the wavelength. The resonant coupling occurs at 710 nm. Right column: The electrical field at different positions around the aperture shows again the signature of the TM_{11} mode. The diagram demonstrates at different wavelength how the field energy evolves along the tapered waveguide. The energy is normalised to the respective area of the waveguide. All grey scalings are identical for electric and magnetic fields, respectively.

matching the respective impedances of waveguide and aperture. As a novel variant of Extraordinary Optical Transmission, we call this resonant phenomenon *Waveguide-Resonant Extraordinary Transmission* (WR-EOT).

The impedance of a waveguide for a particular mode is function also of the physical diameter of the mode-confining volume. The tapering of the waveguide results in a continuously changing profile of the impedance. The impedance diverges when the transverse section of the tapered waveguide approaches the transverse section of the mode and the mode reaches its cut-off. We have shown that the spectral position of the resonant coupling of the aperture depends linearly on the final diameter of the tapered waveguide. Numerical calculations have confirmed this dependence. We were able to tune the resonance spectrally between 600 and 900 nm by varying the final diameter of the waveguide.

The experimental results and the numerical calculation prove that the mode present at the very end of the tapered waveguide is the TM_{11} mode. This mode is the lowest-order mode that allows for concentric apertures. At its mode cut-off, it becomes evanescent away from the metal film with the aperture and its transverse magnetic field diverges. Therefore, it is equivalent to a surface wave and its energy is stored near the surface with the aperture. This effectively increases the feed to the aperture and explains the improved transmission through the sub-wavelength aperture.

In conclusion, the near-field coupling between these intrinsically very different nanostructures can be controlled by carefully choosing their respective physical dimensions.

5 High-Throughput Near-Field Fibre Probes for Sub-Wavelength Control of Single Emitters

Near-Field Scanning Optical Microscopy (NSOM) offers an optical resolution beyond the diffraction limit and has shown to be an important experimental method for various applications in imaging, sensing, material science and lithography. However, a major contraint is the very low brightness of aperture probes. Apart from the low, fundamentally restricted transmission through a sub-wavelength-sized aperture, the feed of the light field to the aperture through a tapered waveguide accounts for high losses. These losses are not induced by physical principles but by the design and fabrication of the probe. In this chapter, we propose a novel nanostructured NSOM aperture probe that gives a 100× higher throughput and 40× increased damage threshold than conventional near-field aperture probes. The probe design incorporates only a minimum of lossy sub-wavelength components to compress the field, greatly reducing the losses of the probe. The increase in brightness in turn allows to employ smaller apertures. We show experimentally by imaging single molecules that the optical field is controlled and confined to within 45 nm.

Section 5.1 starts with an introduction to sub-wavelength imaging with aperture probes and its challenges. The advantages of the proposed probe design are discussed in this context. Section 5.2 reports on the technical aspects including the fabrication of the proposed probe, a sample containing single molecules, and the experimental set-up. The experimental results are analysed in Section 5.3 and the conclusion drawn in Section 5.4.

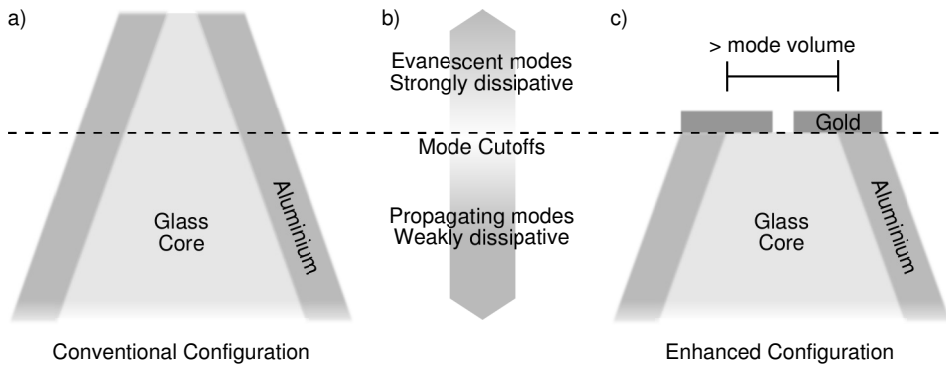

Figure 5.1: **Proposed scheme of device.** The conventional NSOM probe in (a) features a partially sub-wavelength-sized taper which supports only evanescent modes (b). In the proposed novel design in (c), the diameter of the taper is chosen such that the cross section always exceeds the mode volume of the lowest order mode. Therefore, at least one mode can always propagate freely along the waveguide. The sub-wavelength aperture is now formed in an additional film of gold on the end face.

5.1 Introduction to Aperture Probes

In the field of nanoscopy, a strong interest lies in the optical investigation, control and manipulation of soft and hard matter with feature sizes that extend to well below the diffraction limit of light [74]. The challenge lies in the realisation of experimental schemes that enable to control and confine light fields to sub-wavelength, seemingly un-physical volumes, while meeting basic requirements in efficiency, reproducibility and usability.

A Brief History of Probe Design Bethe had discovered the physical principle of Near-Field Scanning Optical Microscopy (NSOM) in 1944 [4] and the first experimental proof came from Pohl et al. in 1984 [5]. The design of an aperture near-field probe is sketched in Figure 5.1(a) and has remained largely unchanged since 1984. It consists of a tapered waveguide, that compresses the light field, and the aperture itself. The compression is required, because an NSOM probe should follow the topography of the sample as closely as possible, both to avoid imaging artefacts and to map the sample topography. In the first realisation, Pohl et al. had etched a quartz crystal to yield a pointed tip, which was then coated with an opaque metal layer of Aluminium. Mechanical pressure exerted on the pointed tip locally removed the metal and created an aperture of a few ten nanometres. Laser light fed to this quartz crystal traversed the aperture in form of an

evanescent field bound to the aperture region. When placed in extreme proximity of a few nanometres to a sample surface, this evanescent field interacts e.g. with single molecules on this surface and excites their fluorescence. The resolution is only determined by the diameter of the aperture and the intensity of the transmitted light.

Today, most researchers use an optical fibre instead of a quartz crystal that is either etched or heat-pulled to yield a sharp taper. Researchers familiar with Atomic Force Microscopy (AFM) may prefer Silica cantilevers over fibres because a cantilever is already sufficiently sharp and fits into any commercial AFM [152]. An elegant alternative is a sophisticated photopolymerisation of a liquid drop of polymer [153]. Independent of the nature of the probe, it must be coated with an opaque layer of aluminium or gold such that light leakage is prevented (see Section 2.2). The formation of the aperture is mostly done by FIB milling nowadays, because FIB systems allow a very high level of control and are availability in many research laboratories (see Section 2.3) [80, 154].

The Loss Channels. For an attempt to improve the transmissivity of a probe, it is important to assess where and how the losses within a probe occur. The design of the probe - a combination of a taper and a sub-wavelength aperture - suggest three different mechanisms that determine the losses and thus the efficiency of the probe: The coupling of the aperture to the taper, the transmissivity of the aperture and the light propagation to the aperture region inside the taper. Losses may occur in form of reflection back into the fibre and absorption by the coatings.

The coupling of the sub-wavelength aperture to the taper had been addressed in Chapter 4 when the final diameter of the taper was chosen such that the aperture couples in a resonant manner to the tapered fibre waveguide. This coupling improves the transmissivity merely by a factor two which is hardly noteworthy given a typical transmissivity of such a probe of at most 10^{-5}. The transmissivity of the aperture is fundamentally constraint. Bethe had set an inverse forth power-dependence of the transmissivity on the diameter [4]. Given that the required resolution is a fixed variable set by the features on the sample, the required aperture size and with it the theoretically achievable transmissivity are automatically fixed as well.

The third mechanism, the light propagation to the aperture region inside the taper, is the channel with the most potential of improvement. I will constrain the discussion of the losses in this mechanism to the taper of optical fibres. The discussion of probes based on AFM cantilevers and others is analogous and will be omitted here.

For a probe based on an optical fibre, laser light is coupled into the non-tapered end of the fibre and guided in a stable, low-loss optical mode in the core of the fibre [74]. The geometry and material composition of the fibre determine the dominant optical mode and the length of the fibre the suppression of other modes. As sketched in Figure 5.1(a) and (b), a waveguide mode propagates along the tapered waveguide only until it has reached its cut-off. At cut-off, the mode volume exceeds the available volume of the waveguide. The processes occurring now are reflection and absorption by the coating of the fibre and transition to a different mode configuration [155]. This transition may include same-order modes with a different confinement, e.g. by a combination of core and cladding instead of only the core, and lower-order modes of a smaller volume. These processes occur continuously along the taper until the mode volume of any possible modes exceeds the size of the waveguide. Here, no propagating modes are supported any more and the entire light field becomes evanescent. The losses due to absorption and reflection increase with a decreasing number of available modes with lower mode volumes. The losses are the greatest, when also the lowest order mode as the lowest propagating mode is not supported any more.

Probe Damage Through Heating. Absorption losses in the taper region can cause considerable heating of the aluminium coating. The literature reports increases in temperature by several hundred degrees close to the tip [156–158]. Heat transfer from the hot tip to the sample may affect some biological and lithographic applications, however, the major problem is the possible damage to the probe itself. The heat may cause diffusion in the aluminium layer of which uncontrolled leakage and a widening of the aperture can be a consequence. In the worst case, the aluminium layer and with it the aperture may get destroyed altogether. The existence of a threshold to the input power at which damage of a fibre probe may occur limits the maximal output power of an NSOM probe to only a few nanowatts [154]. Heat thus constitutes a major problem. Any attempt to increase the efficiency and the output power of a fibre probe must address the absorption losses in the taper as well.

Geometry and Evanescent Fields. While the absorption losses impact the efficiency of the probe by limiting the maximal input power, the evanescent character of the fields at cut-off proves a limitation to the relative transmission. Only evanescent fields confine to volumes better than the diffraction limit, however at the cost of a very short decay length of around 30 nm. In the conventional probe design in Figure 5.1(a), the light propagates in a low-loss fibre mode until it reaches its respective mode cut-off. An evanescent wave is excited that decays exponentially from its mode cut-off to the aperture. Obviously, the magnitude of the field that finally drives

the aperture depends inversely exponentially on the distance between mode cut-off and aperture. A reduction of this distance will improve the relative transmission of the probe as a whole.

The Proposed Probe Design. One way to reduce the losses and to avoid heat induced damage is the launch of surface plasmons inside [159] and outside [81] the probe. The surface plasmons aid to transport the field energy efficiently to the tip of the probe and focus equally well as conventional NSOM fibre probes.

In this chapter, we propose and realise a novel design of an aperture probe that suffices without the last, lossy sub-wavelength sized part of the taper and does not rely on plasmon guiding. The proposed design has two advantages: First, absorption is greatly reduced as the taper is always wide enough to fit a propagating mode. Second, the light field is never of evanescent, exponentially decaying character, but of propagating character and maintains its field strength to the aperture. As sketched in Figure 5.1(c), the upper, narrow part of the fibre is completely removed, while the aperture is formed in an additional gold film on the end face. This design is similar to the design presented in Chapter 4 for Waveguide-Resonant Extraordinary Optical Transmission (WR-EOT). However, here we lift the strict relation between the final diameter of the taper and the diameter of the aperture. The final taper diameter is simply chosen large enough such that at least one mode can propagate.

5.2 The Fabrication of the Probe and Experimental Set-Ups

This section illustrates and discusses the technical aspects of the experiment. The fabrication a probe according to the proposed design is explained, followed by details on the employed sample of single molecules. In the last part, the experimental set-ups are introduced.

Fabrication of the High-Throughput Near-Field Probe

The design of the high-throughput near-field fibre probes is essentially identical to that of the resonant probes discussed in the previous Chapter 4. However, since the resonance condition has been dropped, the final diameter of the taper and the diameter of the aperture are fully independent of each other and may take arbitrary values. Therefore, only the most important details of the probe fabrication are presented here. The reader may refer to Section 4.2 for more details.

In the process of fabricating such probe, an optical fibre (Thorlabs,

SM600) is tapered and coated with at least 200 nm of Aluminium to prevent light leakage (see Section 2.2). Using an FIB system, parts of the tip are removed to reach the desired diameter of the tapered core (see Section 2.3). In the next step, a gold layer of around 110 nm is evaporated on the end face of the probes which acts as the structural layer. Again using an FIB system, the aperture is formed in the end face with the desired diameter. Careful calibration of the employed dose of the ion beam guarantees that the beam mills only through the gold layer and that the glass core is damaged as little as possible. The choice of two different materials, aluminium and gold, reflects the required functionality of the coatings and has been discussed in Section 4.2.

As mentioned previously, the exact shape of the taper strongly influences the transmissivity of a probe. The reproducibility of heat-pulling is, however, very low, such that a comparison between different probes is not meaningful at all. We address this uncertainty in comparability by fabricating some probes first as conventional NSOM probes and then process them to the high-throughput configuration. As the difference between the two configuration is basically the length of the taper, this processing step means to further cut down the taper. For conventional probes, FIB milling removes the very tip, until a diameter of the glass core of 100 nm has been reached; for high-throughput probes, the milling is continued until the diameter of the core lies at the order of the wavelength.

A selection of SEM images of high-throughput probes is shown in Figure 5.2. We were able realise apertures of a diameter of as little as only 40 nm, shown in Figure 5.2(a). As the Figure 5.2(b) and (c) confirm, this aperture diameter is reproducible and scalable. The final diameters of the taper are chosen to be well above the diameter at which mode cut-off occurs and the sub-wavelength regime begins. As Figures 5.2(d) to (f) show, also a range of different final diameters of the taper were successfully realised.

Therefore, the fabrication of the high-throughput probes can be deemed sufficiently reproducible and repeatable.

Preparation of the Single Molecules

Terrylene diimide (TDI) molecules are highly photostable dyes [160] and as such well-suited for slow near-field applications. As shown in Figure 5.3, the dye has several absorption bands at 552 nm, 597 nm and 651 nm. The latter is the strongest band and overlaps well with the wavelength of the exciting laser, an *Innova 70C Spectrum*, tuned to 647 nm.

The dyes are diluted with a solution of 0.1 % Poly(methyl methacrylate) (PMMA) in Toluene, well-mixed and spin-coated on a standard microscope glass slide. As the near-field of a probe approaching the slide with the

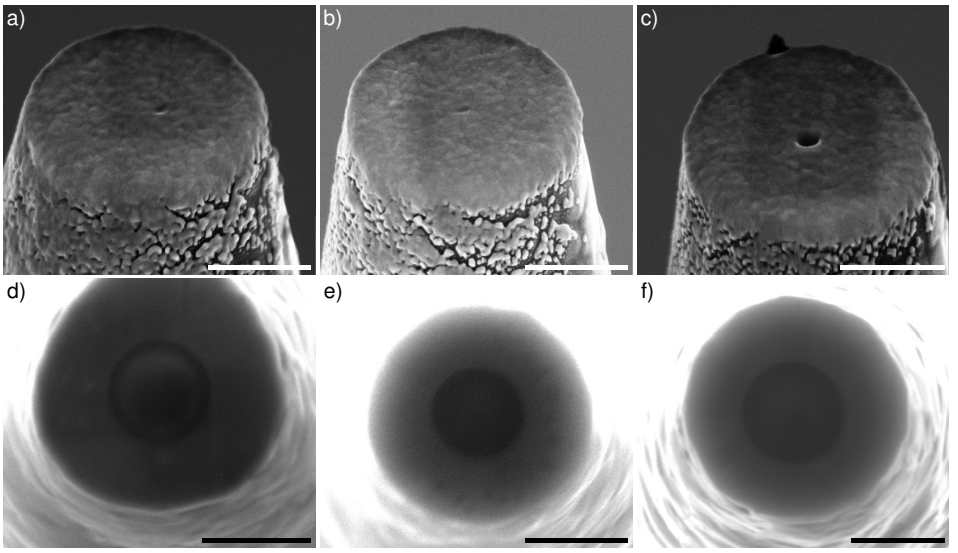

Figure 5.2: **Selected High-Throughput Near-Field Probes.** The SEM images (a), (b) and (c) show several high-throughput probes with apertures of 40 nm, 47 nm and 100 nm in diameter, respectively. Images (d), (e) and (f) show the same probes, however before deposition of the structural gold film. The final diameters of the tapers are 470 nm, 440 nm and 540 nm. The scale bars are 500 nm long.

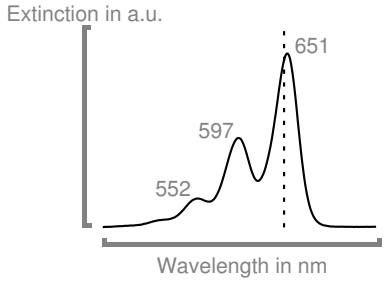

Figure 5.3: **Extinction spectrum of terrylene diimide (TDI)**. The dashed line indicates the spectral position of the exciting laser light at 647 nm.

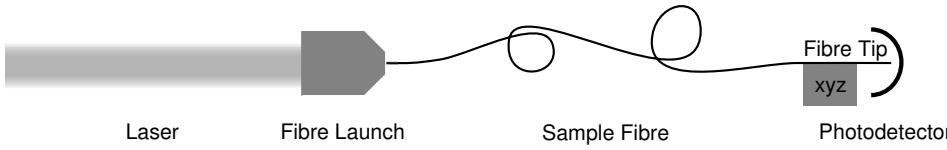

Figure 5.4: **Measuring Throughput and Damage Threshold.** Laser light at 647 nm is launched into the high-throughput probe. The end with the aperture is positioned in close proximity to a large photo detector and the transmission recorded.

polymer layer decays exponentially, a thickness of not more than a few ten nanometres is necessary to ensure that the dyes can interact with the decaying near-field. Verification with a *Stylus* device reveals a thickness of 65 ± 15 nm, which is within an acceptable range.

The concentration of the dyes is adjusted such that individual dye molecules appear well separated in optical images taken in a standard, diffraction limited microscope. This is not sufficient to prove that a fluorescence signal arises from indeed just a single dye molecule and not a cluster of many dye molecules. However, this is the best approximation with the available experimental set-up. Also, as only the resolution of a probe and not quantum properties of the dye are tested, clustering on a length scale significantly smaller than the resolution of the probe is not critical. A mass concentration of 10^{-5} % of the original TDI solution in the solution of PMMA in Toluene permitted exactly this.

Experimental Set-Ups

The measurement of the high-throughput near-field probes requires two different set-ups. The first set-up allows to determine the absolute throughput and the damage threshold of a probe. The second set-up verifies the improved resolution and its suitability as a near-field probe to image single molecules.

Measuring the Absolute Throughput and the Damage Threshold The dedicated set-up is shown in Figure 5.4. It consists of a fibre launch, the high-throughput probe, a translation stage and a large photodetector. Laser light of a wavelength of 647 nm is coupled into the high-throughput probe at the fibre launch. As a sub-wavelength aperture radiates inhomogeneously into the full half-sphere [161], care must be taken to collect a meaningful fraction of the total irradiated intensity. With the help of the translation stage, the tapered end of the probe with the aperture is placed

approximately less than a millimetre away from a photodetector. The photodetector has an edge length of 5 mm, significant enough to ensure that a large share of the emitted light is detected.

Some probes are measured in both the conventional NSOM configuration and the high-throughput configuration. For these probes, the transmissivity in the conventional NSOM configuration is recorded first. Afterwards, the fibre processed to the high-throughput configuration. For all probes, the transmissivity in the enhanced, high-throughput configuration is recorded in the described manner.

Now, for most of the probes, the precise coupling efficiency of the fibre launch is determined by removing the tapered part of the fibre, cleaving the fibre end and recording the transmissivity without the taper. Knowledge of the precise coupling efficiency allows to narrow the error in the transmissivity, even though the coupling efficiency plays only a minor role when noting the extremely small overall transmissivity of the probe itself.

For some of the probes we investigated the damage threshold. The intensity coupled into the fibre is slowly increased while monitoring the emitted intensity. When the threshold has been reached and sufficient heat has accumulated at the apex, the melting gold layer manifests itself in a dramatic increase of the transmissivity. Also here the coupling efficiency is established by removing the tapered part of the fibre and recording the transmissivity.

As a last remark it may be noted that the particular choice of wavelength and core diameter of the probes does make the presence of the resonant effects described in Chapter 4 very unlikely.

Assessing the Suitability as a Near-Field Probe The high-throughput probe is assessed in a standard Near-Field Scanning Optical Microscope. In Section 1.3, I have already introduced the basic concepts of Near-Field Scanning Optical Microscopy (NSOM). The experimental set-up employed also here is depicted in Figure 1.1. The suitability of the probe is tested by imaging single molecules in the near-field.

An *Innova 70C Spectrum* laser provides the excitation laser light at 647 nm which is coupled into the high-throughput probe at the launch. Single molecules are excited by the aperture, and their fluorescence recorded by two avalanche photodetectors (APD).

5.3 Results — Transmission and Damage Threshold

In this section the experimental results are presented. We show how the throughput and the damage threshold of the probe have been improved.

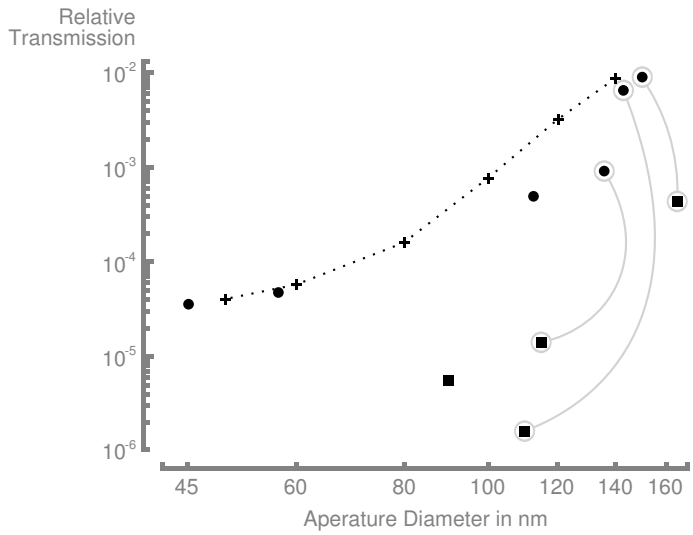

Figure 5.5: **Improved Throughput.** The relative transmission of the enhanced near-field probes (circles) at a wavelength of 647 nm is approximately two orders of magnitude better than for the conventional probes (squares) with similar apertures. The numerically calculated throughput (crosses, dotted line guide to the eye) is fitted to the experimental data in order to account for losses not included in the simulations. It reflects well the trend in transmission of the high-throughput probes. Some probes were measured in the conventional NSOM configuration first and then processed and measured in the high-throughput configuration. The data points representing the throughput for a single probe in the two configurations are connected by grey lines.

As a result of these improvements, it has become possible to reduce the size of the aperture. We confirm this conclusion by a demonstration of the imaging properties of a probe with a 40 nm aperture.

The Improved Throughput

The relative transmission of the fabricated high-throughput probes and, for comparison, also of conventional near-field probes is shown for various aperture diameters in Figure 5.5. As mentioned before, variations in the shape of the taper of individual probes can have spurious effects on the transmission data. In an effort to compensate this, some probes were first fabricated in the conventional NSOM configuration and their throughput recorded. Afterwards, they were processed to into the high-throughput probe design and their throughput recorded again. Data points belonging

to the same fibre in the two different configurations are connected by grey lines.

Clearly visible is the improvement of the transmissivity by two to three orders of magnitude for the high-throughput probes compared to conventional fibre aperture probes. For a typical aperture size of around 100 nm, We measure a throughput in the high-throughput configuration of 10^{-3}. Previous data and the literature [80,154] show a throughput of only around 10^{-5} or less for conventional probes.

As the aperture size of conventional probes has a lower bound given by the required brightness, any improvement in the transmissivity in turn permits to shrink the aperture while still maintaining a sufficiently high level of brightness. The probe with the smallest fabricated aperture, of 45 nm in diameter and displayed in Figure 5.2(a), still yields a transmissivity of better than 10^{-5}. This is over an order of magnitude better than the transmissivity of a conventional NSOM probe with a diameter twice as large. Bethe predicted the transmission of a single aperture to depend on the forth power on the radius of the aperture [4]. Though not fully applicable to these two different types of probes, the observed change in transmissivity with the aperture size follows the prediction approximately.

In an attempt to provide a more quantitative comparison with the experimental results, comprehensive finite-difference time domain (FDTD) simulations were performed by the group of Reuven Gordon. Details to these simulations can be found in [162] and the numerical calculations are marked by crosses in Figure 5.5. The dotted line is a guide to the eye only. As the simulations do not account for all loss channels, e.g. the taper outside the necessarily limited computation domain, the calculated relative throughput is fitted to the absolute values in the experimental data. As clearly visible, the values of the simulated throughput for smaller apertures follow nicely the same trend as the experimental values.

Therefore, two orders of magnitude enhancement in the throughput is achieved with this high-throughput configuration. This corresponds to a reduction in aperture diameter by over a factor two while maintaining the same the excitation power compared to the conventional NSOM configuration.

The Higher Damage Threshold

Shown in Figure 5.6 is the evolution of the transmitted intensity with the in-coupled intensity for a high-throughput near-field probe. The diameter of the aperture of this probes is 105 nm. The power in the fibre, as depicted in the Figure, is indeed the power just before the taper. The intensity measured at the fibre launch had been corrected for the coupling efficiency, thus

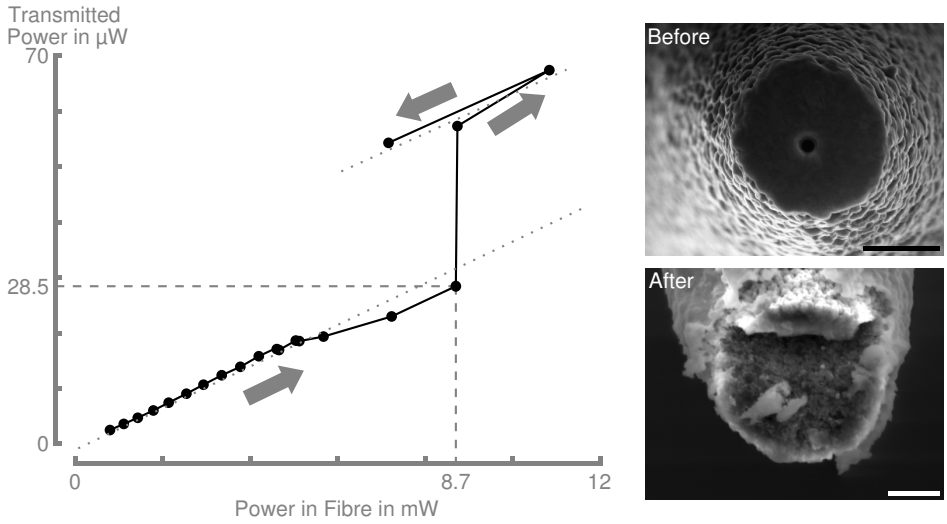

Figure 5.6: **Higher Damage Threshold.** A steep increase in the power transmitted by the aperture marks the damage threshold at over 8 mW inside the fibre. The arrows indicate how the power was ramped and the dashed lines mark the threshold. The two dotted lines are guides to the eye. The two SEM images show the probe before and after crossing the damage threshold. The scale bars are 500 nm long.

is equal to the intensity inside the fibre, before the taper. Clearly visible is a linear regime during which the transmitted intensity increases slowly with the launch intensity. At 8.7 mW, the transmitted intensity jumps abruptly and enters another linear regime at a much higher transmitted intensity.

The two SEM images in Figure 5.6, taken before and after the experiment, confirm clearly that the probe had been altered physically and irreversibly during the experiment. The layer at the end face is completely flawed and the gold mostly removed. The core of the fibre, which is visible now, appears very grainy and lacks the smoothness it had gained by focused ion beam milling. The aluminium layer that had covered the sides the fibre probe, is faulty as well and exhibits a very grainy surface, potentially prone to light leakage.

Principally, probe damage can occur due to thermal and mechanical stress. A mechanical origin of the damage seen in Figure 5.6 can be ruled out safely. If mechanical stress had been the reason, the fibre would exhibit smooth breaking surfaces and edges. Very likely not only the coating of the end face, but several micron of glass core would have broken off completely. From the author's experience, the SEM image taken after the experiment shows a typical case of overheating of a near-field probe. This irreversible

damage occurred when crossing the damage threshold. The steep jump in transmissivity was the consequence of the destruction of the aperture.

Assuming a typical coupling efficiency of 5%[1], the 8.7 mW inside the fibre at the taper correspond to over 170 mW at the launch where the intensity is routinely measured. As, in author's experience, conventional NSOM fibre break down at input intensities of 4 - 5 mW, the damage threshold improves by over a factor 40×.

We attribute the higher damage threshold, which is equivalent to a reduction of the heat load on the metal coating, to the broader design of the probe. First, the much larger surface of the probe reduces the optical intensities on the coating and supports a better heat transfer away from the very tip. Second, since at least one mode can still propagate inside the tapered fibre, effective back-reflection into a propagating mode is possible, which directly reduces absorption close to the tip.

Imaging Single Molecules

The high-throughput near-field probes may excel in transmissivity, however, they still have to prove an at least equal applicability and performance in the imaging of single molecules as conventional NSOM probes.

Figure 5.7 shows a near-field image of single terrylene diimide (TDI) molecules. The probe has been scanned over the sample with nanometric accuracy, and the figure shows the fluorescence signal recorded during the scan. The fluorescence spots of the two molecules presented in the insets show a confinement to around 62 nm (FWHM) in both axis. This is slightly larger than the nominal aperture diameter of 45±10 nm as determined from SEM images of this specific fibre. This slightly larger size of the fluorescence spot is attributed to the penetration of the electric field into the gold film hosting the aperture, which increases the effective aperture size, and to the finite aperture-molecule distance, that results in a certain spread of the excitation field.

The reader may have some doubt whether a gold layer of about 110 nm is sufficiently optically thick (see discussion on materials in Section 2.2). If it were not, some light may leak through the coated part of end face rather than being transmitted through the aperture. This would obviously falsify any data taken with a particular probe. The signal-to-noise ratio of the fluorescence trace of single molecules gives a good estimate of whether leakage might be a problem. If the gold layer is indeed not sufficiently thick, the fluorescence signal arising from excitation by leakage through the gold layer should be comparable to the fluorescence signal arising from

[1]Since lasers usually provide more power than required for NSOM, a low efficiency can be acceptable if the coupling in turn is very stable over time.

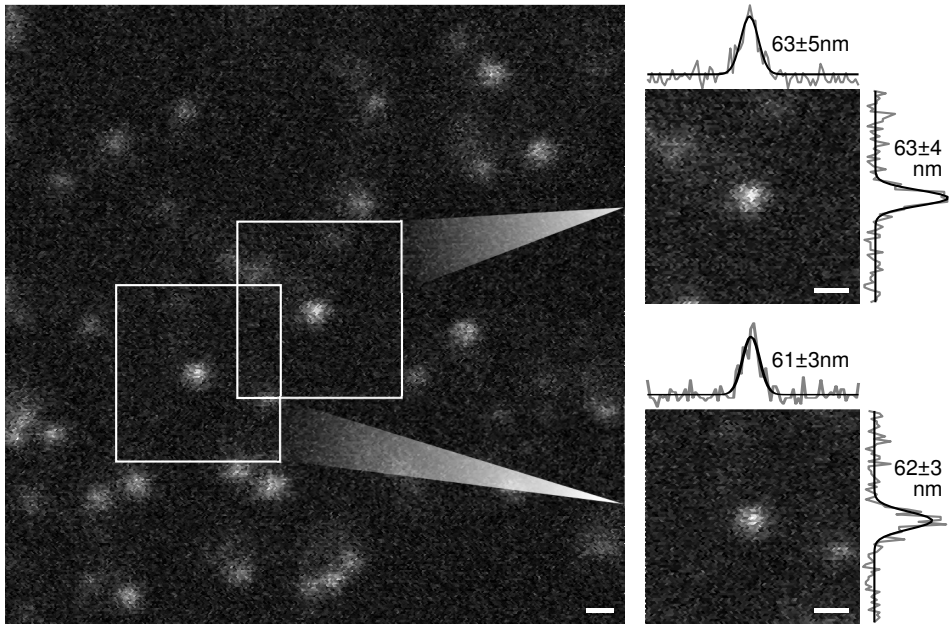

Figure 5.7: **Assessing Resolution and Sensitivity.** The Near-Field image of single TDI molecules with an aperture probe of 47 nm in diameter reveals the improved resolution. The spatial widths of the fluorescence spots are around 62 nm and reproducible for different molecules. All scale bars are 100nm long.

excitation by the aperture alone. As it is clear from the fluorescence traces in Figure 5.7, the excitation through the aperture dominates significantly over the background signal and fluctuations. This is supported by a signal-to-noise ratio of $20:4$. Even though this argument cannot rule out leakage through the gold layer altogether, the dominant signal arises clearly from the aperture.

5.4 Conclusion – Suitable as a Near-Field Probe

The mayor advance successfully demonstrated in this chapter is the near-field imaging of single molecules with apertures as small as only 45 nm in diameter. The high-throughput near-field fibre probe is indeed capable of imaging fluorophors reliably. The optical resolution exceeds that of the conventional probe design by a factor two while providing a comparable or even better brightness. In fact, the path towards smaller apertures and higher resolution seems limited not by the transmissivity of the probe, but rather by the finite penetration depth of the light into the metal, which

effectively widens the aperture, and the resolution of the Focused Ion Beam system.

It is important to recall that the throughput of a single aperture depends inversely on the radius to the power of four. Thus, the factor two gained in resolution while maintaining the level of brightness corresponds to an increase in throughput by almost two orders of magnitude. The probes fabricated successively in the conventional and the high-throughput design demonstrate this gain convincingly, and comprehensive FDTD simulations agree well with the experimental findings.

The modified probe design comes with a 40× higher damage threshold. The wider base reduces the optical densities inside the fibre and improves the heat transport from the very tip, which both reduces the heat load on the coating. We have recorded maximum output powers of up to 28μW.

The high throughput and damage threshold stress the potential of this probe design. Some reader may argue that this comes at the cost of a second fabrication step of evaporation and FIB milling. The second fabrication step may indeed consume some fabrication time, but can be accomplished more easily with every new generation of deposition devices and FIB systems. A second remark may be that the apex of the fibre has a diameter about twice as large as conventional probes which could be problematic whenever a recording of the sample topography is wished. This is easily addressed by placing a sharp feature like an optical monopole antenna near to the aperture [26, 37][2].

Applications, that may benefit from the high efficiency of the demonstrated high-throughput near-field probe, may require either high resolution e.g. in biology [163] or high intensities as for nonlinear interactions [164–168].

[2]This can done easily by electron beam deposition. FIB milling as employed in the two references might damage the coating of the end face.

Bibliography

[1] E. Abbe. Beiträge zur Theorie des Mikroskops und der Mikroskopischen Wahrnehmung. *Archiv f. Mikroskop. Anat.*, 9:413, 1873.

[2] L. Rayleigh. Investigations in optics, with special reference to the spectroscope. *Phil. Mag.*, 5:167, 1896.

[3] E. A. Synge. A suggested method for extending microscopic resolution into the ultra-microscopic region. *Phil. Mag.*, 6:356, 1928.

[4] H. A. Bethe. Theory of diffraction by small holes. *Phys. Rev.*, 66:163, 1944.

[5] D. W. Pohl, W. Denk, and M. Lanz. Optical stethoscopy: Image recording with resolution $\lambda/20$. *Appl. Phys. Lett.*, 44(7):651, 1984.

[6] A. Lewis, M. Isaacson, A. Harootunian, and A. Muray. Development of a 500 Å spatial resolution light microscope: I. light is efficiently transmitted through $\lambda/16$ diameter apertures. *Ultramicroscopy*, 13(3):227, 1984.

[7] E. Betzig and R. J. Chichester. Single molecules observed by near-field scanning optical microscopy. *Science*, 262:1422, 1993.

[8] L. Novotny. Effective wavelength scaling for optical antennas. *Phys. Rev. Lett.*, 98:266802, 2007.

[9] A. Alù and N. Engheta. Tuning the scattering response of optical nanoantennas with nanocircuit loads. *Nat. Photonics*, 2:307, 2008.

[10] M. L. Brongersma. Engineering optical nanoantennas. *Nat. Photonics*, 2:270, 2008.

[11] T. Ishi, J. Fujikata, K. Makita, T. Baba, and K. Ohashi. Si nano-photodiode with a surface plasmon antenna. *Jpn. J. Appl. Phys.*, 44:L364, 2005.

[12] L. Tang, S. E. Kocabas, S. Latif, A. K. Okyay, D.-S. Ly-Gagnon, K. C. Saraswat, and D. A. B. Miller. Nanometre-scale germanium photodetector enhanced by a near-infrared dipole antenna. *Nat. Photonics*, 2:226, 2008.

[13] M. W. Knight, H. Sobhani, P. Nordlander, and N. J. Halas. Photodetection with active optical antennas. *Science*, 332:702, 2011.

[14] D. M. O'Carroll, C. E. Hofmann, and H. A. Atwater. Conjugated polymer/metal nanowire heterostructure plasmonic antennas. *Adv. Mater.*, 22:1223, 2010.

[15] H. A. Atwater and A. Polman. Plasmonics for improved photovoltaic devices. *Nat. Mater.*, 9:205, 2010.

[16] A. Bouhelier, M. Beversluis, A. Hartschuh, and L. Novotny. Near-field second-harmonic generation induced by local field enhancement. *Phys. Rev. Lett.*, 90:013903, 2003.

[17] W. Fan, S. Zhang, N.-C. Panoiu, A. Abdenour, S. Krishna, R. M. Osgood, K. J. Malloy, and S. R. J. Brueck. Second harmonic generation from a nanopatterned isotropic nonlinear material. *Nano Lett.*, 6(5):1027, 2006.

[18] S. Kim, J. Jin, Y.-J. Kim, I.-Y. Park, Kim. Y, and S.-W. Kim. High-harmonic generation by resonant plasmon field enhancement. *Nature*, 453:757, 2008.

[19] M. Danckwerts and L. Novotny. Optical frequency mixing at coupled gold nanoparticles. *Phys. Rev. Lett.*, 98:026104, 2007.

[20] P. Ghenuche, S. Cherukulappurath, T. H. Taminiau, N. F. van Hulst, and R. Quidant. Spectroscopic mode mapping of resonant plasmon nanoantennas. *Phys. Rev. Lett.*, 101:116805, 2008.

[21] M. Castro-Lopez, D. Brinks, R. Sapienza, and N. F. van Hulst. Aluminum for nonlinear plasmonics: Resonance-driven polarized luminescence of Al, Ag, and Au nanoantennas. *Nano Lett.*, 11:4674, 2011.

[22] P. J. Schuck, D. P. Fromm, A. Sundaramurthy, G. S. Kino, and W. E. Moerner. Improving the mismatch between light and nanoscale objects with gold bowtie nanoantennas. *Phys. Rev. Lett.*, 94:017402, 2005.

[23] M. Righini, P. Ghenuche, S. Cherukulappurath, V. Myroshnychenko, F. J. García de Abajo, and R. Quidant. Nano-optical trapping of Rayleigh particles and Escherichia coli bacteria with resonant optical antenna. *Nano Lett.*, 9(10):3378, 2009.

[24] D. E. Chang, J. D. Thompson, H. Park, V. Vuleti, A. S. Zibrov, P. Zoller, and M. D. Lukin. Trapping and manipulation of isolated atoms using nanoscale plasmonic structures. *Phys. Rev. Lett.*, 103:123004, 2009.

[25] N. Liu, M. L. Tang, M. Hentschel, H. Giessen, and A. P. Alivisatos. Nanoantenna-enhanced gas sensing in a single tailored nanofocus. *Nat. Mater.*, 10:631, 2011.

[26] T. S. van Zanten, M. J. Lopez-Bosque, and M. F. Garcia-Parajo. Imaging individual proteins and nanodomains on intact cell membranes with a probe-base optical antenna. *Small*, 6(2):270, 2010.

[27] J. N. Farahani, D. W. Pohl, H.-J. Eisler, and B. Hecht. Single quantum dot coupled to a scanning optical antenna: A tunable superemitter. *Phys. Rev. Lett.*, 95:017402, 2005.

[28] T. H. Taminiau, F. D. Stefani, F. B. Segerink, and N. F. van Hulst. Optical antennas direct single-molecule emission. *Nat. Photonics*, 2:234, 2008.

[29] A. G. Curto, G. Volpe, T. H. Taminiau, M. P. Kreuzer, R. Quidant, and N. F. van Hulst. Unidirectional emission of a quantum dot coupled to a nanoantenna. *Science*, 329:930, 2011.

[30] M. L. Andersen, S. Stobbe, A. Søndberg Sørensen, and P. Lodahl. Strongly modified plasmon-matter interaction with mesoscopic quantum emitters. *Nat. Phys.*, 7:215, 2010.

[31] L. Novotny and N. van Hulst. Antennas for light. *Nat. Photonics*, 5:83, 2011.

[32] J. A. Schuller, E. S. Barnard, W. Cai, Y. C. Jun, J. S. White, and M. L. Brongersma. Plasmonics for extreme light concentration and manipulation. *Nat. Mater.*, 9:193, 2010.

[33] P. Biagioni, J.-S. Huang, and B. Hecht. Nanoantennas for visible and infrared radiation. *Rep. Prog. Phys.*, 75:024402, 2012.

[34] V. Giannini, A. I. Fernández-Domínguez, S. C. Heck, and S. A. Maier. Plasmonic nanoantennas: Fundamentals and their use in controlling the radiative properties of nanoemitters. *Chem. Rev.*, 111:3888, 2011.

[35] P. Bharadwaj, B. Deutsch, and L. Novotny. Optical antennas. *Adv. Opt. Photon.*, 1:438, 2009.

[36] H. G. Frey, F. Keilmann, A. Kriele, and R. Guckenberger. Enhancing the resolution of scanning near-field optical microscopy by a metal tip grown on an aperture probe. *Appl. Phys. Lett.*, 81(26):5030, 2002.

[37] T. H. Taminiau, R. J. Moerland, F. B. Segerink, L. Kuipers, and N. F. van Hulst. $\lambda/4$ resonance of an optical monopole antenna probed by single molecule fluorescence. *Nano Lett.*, 7(1):28, 2007.

[38] M. Schnell, A. García-Etxarri, A. J. Huber, K. Crozier, J. Aizpurua, and R. Hillenbrand. Controlling the near-field oscillations of loaded plasmonic nanoantennas. *Nat. Photonics*, 3:287, 2009.

[39] T. Kosako, Y. Kadoya, and H. F. Hofmann. Directional control of light by a nano-optical yagi-uda antenna. *Nat. Photonics*, 4:312, 2010.

[40] J. Dorfmüller, D. Dregely, M. Esslinger, W. Khunsin, R. Vogelgesang, K. Kern, and H. Giessen. Near-field dynamics of optical Yagi-Uda nanoantennas. *Nano Lett.*, 11:2819, 2011.

[41] P. Mühlschlegel, H.-J. Eisler, O. J. F. Martin, B. Hecht, and D. W. Pohl. Resonant optical antennas. *Science*, 308:1607, 2005.

[42] G. Volpe, G. Volpe, and R. Quidant. Fractal plasmonics: Subdiffraction focusing and broadband spectral response by a Sierpinski nanocarpet. *Opt. Express*, 19(4):3612, 2011.

[43] K. Li, M. I. Stockman, and D. J. Bergman. Enhanced second harmonic generation in a self-similar chain of metal nanospheres. *Phys. Rev. B*, 72:153401, 2005.

[44] J. N. Farahani, H.-J. Eisler, D. W. Pohl, M. Pavius, P. Flückiger, P. Gasser, and B. Hecht. Bow-tie optical antenna probes for single-emitter scanning near-field optical microscopy. *Nanotechnology*, 18:125506, 2007.

[45] A. Kinkhabwala, Z. Yu, S. Fan, Y. Avlasevich, K. Müllen, and W. E. Moerner. Large single-molecule fluorescence enhancements produced by a bowtie nanoantenna. *Nat. Photonics*, 3:654, 2009.

[46] N. A. Hatab, C.-H. Hsueh, A. L. Gaddis, S. T. Retterer, J.-H. Li, G. Eres, Z. Zhang, and B Gu. Free-standing optical gold bowtie nanoantenna with variable gap size for enhanced raman spectroscopy. *Nano Lett.*, 10:4952, 2010.

[47] M. Mivelle, I. A. Ibrahim, F. Baida, G. W. Burr, D. Nedeljkovic, D. Charraut, J.-Y. Rauch, R. Salut, and T. Grosjean. Bowtie nanoaperture as interface between near-fields and a single-mode fiber. *Opt. Express*, 18(15):15964, 2010.

[48] S. Kühn, U. Håkanson, L. Rogobete, and V. Sandoghdar. Enhancement of single-molecule fluorescence using a gold nanoparticle as an optical nanoantenna. *Phys. Rev. Lett.*, 97:017402, 2006.

[49] P. Bharadwaj and L. Novotny. Spectral dependence of single molecule fluorescence enhancement. *Opt. Express*, 15(21):14266, 2007.

[50] H. Aouani, O. Mahboub, N. Bonod, E. Devaux, E. Popov, H. Rigneault, T. W. Ebbesen, and J. Wenger. Bright unidirectional fluorescence emission of molecules in a nanoaperture with plasmonic corrugations. *Nano Lett.*, 11:637, 2011.

[51] H. Guo, T. P. Meyrath, T. Zentgraf, N. Liu, L. Fu, H. Schweizer, and H. Giessen. Optical resonances of bowtie slot antennas and their geometry and material dependence. *Opt. Express*, 16(11):7756, 2008.

[52] T.-D. Onuta, M. Waegele, C. C. DuFort, W. L. Schaich, and B. Dragnea. Optical field enhancement at cusps between adjacent nanoapertures. *Nano Lett.*, 7(3):557, 2007.

[53] T. Grosjean, M. Mivelle, F. Baida, G. W. Burr, and U. C. Fischer. Diabolo nanoantenna for enhancing and confining the magnetic optical field. *Nano Lett.*, 11:1009, 2011.

[54] P. Biagioni, J.-S. Huang, L. Duò, M. Finazzi, and B. Hecht. Cross resonant optical antenna. *Phys. Rev. Lett.*, 102:256801, 2009.

[55] F. De Angelis, G. Das, P. Candeloro, M. Patrini, M. Galli, A. Bek, M. Lazzarino, I. Maksymov, C. Liberale, L. C. Andreani, and E. Di Fabrizio. Nanoscale chemical mapping using three-dimensional adiabatic compression of surface plasmonic polaritions. *Nat. Nanotechnol.*, 5:67, 2010.

[56] F. De Angelis, F. Gentile, F. Mecarini, G. Das, M. Moretti, P. Candeloro, M. L. Coluccio, G. Cojoc, A. Accardo, C. Liberale, R. P. Zaccaria, G. Perozziello, L. Tirinato, A. Tima, G. Cuda, R. Cingolani, and E. Di Fabrizio. Breaking the diffusion limit with superhydrophobic delivery of molecules to plasmonic nanofocusing sers structures. *Nat. Photonics*, 5:682, 2011.

[57] A. Normatov, P. Ginzburg, N. Berkovitch, G. M. Lerman, A. Yanai, U. Levy, and M. Orenstein. Efficient coupling and field enhancement for the nano-scale: Plasmonic needle. *Opt. Express*, 18(13):14079, 2010.

[58] N. Liu, M. Hentschel, T. Weiss, A. P. Alivisatos, and H. Giessen. Three-dimensional plasmon rulers. *Science*, 332:1407, 2011.

[59] D. W. Pohl, S. G. Rodrigo, and L. Novotny. Stacked optical antennas. *Appl. Phys. Lett.*, 98:023111, 2011.

[60] N. Large, M. Abb, J. Aizpurua, and O. L. Muskens. Photoconductively loaded plasmonic nanoantenna as building block for ultracompact optical switches. *Nano Lett.*, 10:1741, 2010.

[61] M. Schnell, P. Alonso-González, L. Arzubiaga, F. Casanova, L. E. Hueso, A. Chuvilin, and R. Hillenbrand. Nanofocusing of mid-infrared energy with tapered transmission lines. *Nat. Photonics*, 5:283, 2011.

[62] Z. Fang, L. Fan, C. Lin, D. Zhang, A. J. Meixner, and X. Zhu. Plasmonic coupling of bow tie antennas with Ag nanowire. *Nano Lett.*, 11:1676, 2011.

[63] J. Wen, P. Banzer, A. Kriesch, D. Ploss, B. Schmauss, and U. Peschel. Experimental cross-polarization detection of coupling far-field light to highly confined plasmonic gap modes via nanoantennas. *Appl. Phys. Lett.*, 98:101109, 2011.

[64] P. Ginzburg, A. Nevet, N. Berkovitch, A. Normatov, G. M. Lerman, A. Yanai, U. Levy, and M. Orenstein. Plasmonic resonance effects for tandem receiving-transmissing nanoantennas. *Nano Lett.*, 11:220, 2011.

[65] J.-S. Huang, J. Kern, P. Geisler, P. Weinmann, M. Kamp, A. Forchel, P. Biagioni, and B. Hecht. Mode imaging and selection in strongly coupled nanoantennas. *Nano Lett.*, 10(6):2105, 2010.

[66] E. Prodan, C. Radloff, N. J. Halas, and P. Nordlander. A hybridization model for the plasmon response of complex nanostructures. *Science*, 302:419, 2003.

[67] Y. Chen, P. Lodahl, and A. F. Koenderink. Dynamically reconfigurable directionality of plasmon-based single photon sources. *Phys. Rev. B*, 82:081402, 2010.

[68] J.-S. Huang, T. Feichtner, P. Biagioni, and B. Hecht. Impedance matching and emission properties of nanoantennas in an optical nanocircuit. *Nano Lett.*, 9(5):1897, 2009.

[69] J.-J. Greffet, M. Laroche, and F. Marquier. Impedance of a nanoantenna and a single quantum emitter. *Phys. Rev. Lett.*, 105:117701, 2010.

[70] R. Toledo-Crow, P. C. Yang, Y. Chen, and M. Vaez-Iravani. Near-field differential scanning optical microscope with atomic force regulation. *Appl. Phys. Lett.*, 60(24):2957, 1992.

[71] E. Betzig, P. L. Finn, and J. S. Weiner. Combined shear force and nearfield scanning optical microscopy. *Appl. Phys. Lett.*, 60(20):2484, 1992.

[72] R. C. Dunn. Near-field scanning optical microscopy. *Chem. Rev.*, 99:2891, 1999.

[73] A. Bouhelier. Field-enhanced scanning near-field optical microscopy. *Microsc. Res. Techniq.*, 69:563, 2006.

[74] L. Novotny and B. Hecht. *Principles of Nano-Optics*. Cambridge University Press, 2006.

[75] Y. Chen and A. Pépin. Nanofabrication: Conventional and nonconventional methods. *Electrophoresis*, 22:187, 2001.

[76] B. D. Gates, Q. Xu, M. Stewart, D. Ryan, C. G. Willson, and G. M. Withesides. New approaches to nanofabrication: Molding, printing and other techniques. *Chem. Rev.*, 105:1171, 2005.

[77] C. Girard, E. Dujardin, G. Baffou, and R. Quidant. Shaping and manipulation of light fields with bottom-up plasmonic structures. *New J. Phys.*, 10:105016, 2008.

[78] M. T. Wenzel, T. Härtling, P. Olk, S. C. Kehr, S. Grafström, S. Winnerl, M. Helm, and L. M. Eng. Gold nanoparticle tips for optical field confinement in infrared scattering near-field optical microscopy. *Opt. Express*, 16(16):12303, 2008.

[79] H. Namatsu, M. Nagase, K. Kurihara, K. Iwadate, and K. Murase. 10 nm silicon lines fabricated in (110) silicon. *Microelectron Eng*, 27:71, 1995.

[80] J. A. Veerman, A. M. Otter, L. Kuipers, and N. F. van Hulst. High definition aperture probes for near-field optical microscopy fabricated by focused ion beam milling. *Appl. Phys. Lett.*, 72(24):3115, 1998.

[81] Y. Wang, W. Srituravanich, C. Sun, and X. Zhang. Plasmonic near-field scanning probe with high transmission. *Nano Lett.*, 8(9):3041, 2008.

[82] C. C. Neacsu, S. Berweger, R. L. Olmon, L. V. Saraf, C. Ropers, and M. B. Raschke. Near-field localization in plasmonic superfocusing: A nanoemitter on a tip. *Nano Lett.*, 10:592, 2010.

[83] T. Pangaribuan, K. Yamada, S. Jiang, H. Ohsawa, and M. Ohtsu. Reproducible fabrication technique of nanometric tip diameter fiber probe for photon scanning tunneling microscope. *Jpn. J. Appl. Phys.*, 31:L1302–L1304, 1992.

[84] N. Essaidi, Y. Chen, V. Kottler, E. Cambril, C. Mayeux, N. Ronarch, and C. Vieu. Fabrication and characterization of optical-fiber nanoprobes for scanning near-field optical microscopy. *Applied Optics*, 37(4):609, 1998.

[85] P. Hoffman, B. Dutoit, and R. Slathé. Comparison of mechanically drawn and protection layer chemically etched optial fiber tips. *Ultramicroscopy*, 61:165, 1995.

[86] M. Garcia-Parajo, T. Tate, and Y. Chen. Gold-coated parabolic tapers for scanning near-field optical microscopy: fabrication and optimisation. *Ultramicroscopy*, 61:155, 1995.

[87] R. L. Williamson and M. J. Miles. Melt-drawn scanning near-field optical microscopy probe profiles. *J. Appl. Phys*, 80(9):4804, 1996.

[88] S. Franssila. *Introduction to Micro Fabrication*. Wiley, 2 edition edition, 2010.

[89] X. Jiao, J. Goeckeritz, S. Blair, and M. Oldham. Localization of near-field resonances in bowtie antennae: influence of adhesion layers. *Plasmonics*, 4(37):50, 2009.

[90] Heykel Aouani, Jerome Wenger, Davy Gerard, Herve Rigneault, Eloise Devaux, Thomas W. Ebbesen, Farhad Mahdavi, Tingjun Xu, and Steve Blair. Crucial role of the adhesion layer on the plasmonic fluorescence enhancement. *ACS Nano*, 3(7):2043–2048, 2009.

[91] A. Mohammadi, V. Sandoghdar, and M. Agio. Gold, copper, silver and aluminum nanoantennas to enhance spontaneous emission. *J. Comput. Theor. Nanos.*, 6(9):7, 2008.

[92] M. Rycenga, C. M. Cobley, J. Zeng, W. Li, C. H. Moran, Q. Zhang, d. Qin, and Y. Xia. Controlling the synthesis and assembly of silver nanostructures for plasmonic applications. *Chem. Rev.*, 111:3669, 2011.

[93] J. Chen, P. Albella, Z. Pirzadeh, P. Alonso-González, F. Huth, S. Bonetti, V. Bonanni, J. Åkerman, J. Nogués, P. Vavassori, A. Dmitriev, J. Aizpurua, and R. Hillenbrand. Plasmonic nickel nanoantennas. *Small*, 7(16):2341, 2011.

[94] G. V. Naik, J. Kim, and A. Boltasseva. Oxides and nitrides as alternative plasmonic materials in the optical range. *Opt. Mater. Express*, 1(6):1090, 2011.

[95] G. V. Naik and A. Boltasseva. Semiconductors for plasmonics and metamaterials. *Phys. Status Solidi RRL*, 4(10):295, 2010.

[96] F. H. L. Koppens, D. E. Chang, and F. J. García de Abajo. Graphene plasmonics: A platform for strong light — matter interactions. *Nano Lett.*, 11:3370, 2011.

[97] L. A. Giannuzzi and F. A. Stevie, editors. *Introduction to focused ion beams: instrumentation, theory, techniques and practice*. Springer, 2010.

[98] A. A. Tseng. Recent developments in nanofabrication using focused ion beams. *Small*, 1(10):924, 2005.

[99] Y. Q. Fu, N. K. A. Bryan, O. N. Shing, and N. P. Hung. Influence of the redeposition effect for focused ion beam 3D micromachining in silicon. *Int. J. Adv. Manuf. Technol.*, 16:877, 2000.

[100] R. Vogelgesang and A. Dmitriev. Real-space imaging of nanoplasmonic resonances. *Analyst*, 135:1175, 2010.

[101] G. T. Boyd, Z. H. Yu, and Y. R. Shen. Photoinduced luminescence from the noble metals and its enhancement on roughened surfaces. *Phys. Rev. B*, 33(12):7923, 1986.

[102] M. R. Beversluis, A. Bouhelier, and L. Novotny. Continuum generation from single gold nanostructures through near-field mediated intraband transitions. *Phys. Rev. B*, 68:115433, 2003.

[103] P. Biagioni, M. Celebrano, M. Savoini, G. Grancini, D. Brida, S. Mátéfi-Tempfli, M. Mátéfi-Tempfli, L. Duò, B. Hecht, G. Cerullo, and M. Finazzi. Dependence of the two-photon photoluminescence yield of gold nanostructures on the laser pulse duration. *Phys. Rev. B*, 80:045411, 2009.

[104] M. Burresi, D. van Oosten, T. Kampfrath, H. Schoenmaker, R. Heideman, A. Leinse, and L. Kuipers. Probing the magnetic field of light at optical frequencies. *Science*, 326:550, 2009.

[105] A. García-Etxarri, I. Romero, F. J. García de Abajo, R. Hillenbrand, and J. Aizpurua. Influence of the tip in near-field imaging of nanoparticle plasmonic modes: Weak and strong coupling regimes. *Phys. Rev. B*, 79:125439, 2009.

[106] B. Deutsch, R. Hillenbrand, and L. Novotny. Visualizing the optical interaction tensor of a gold nanoparticle pair. *Nano Lett.*, 10:652, 2010.

[107] R. Hillenbrand and F. Keilmann. Complex optical constants on a subwavelength scale. *Phys. Rev. Lett.*, 85(14):3029, 2000.

[108] J. M. Gerton, L. A. Wade, G. A. Lessard, Z. Ma, and S. R. Quake. Tip-enhanced fluorescence microscopy at 10 nanometer resolution. *Phys. Rev. Lett.*, 93(18):180801, 2004.

[109] R. Esteban, R. Vogelgesang, J. Dorfmüller, A. Dmitriev, C. Rockstuhl, C. Etrich, and K. Kern. Direct near-field optical imaging of higher order plasmonic resonances. *Nano Lett.*, 8(10):3155, 2008.

[110] A. V. Akimov, A. Mukherjee, C. L. Yu, D. E. Chang, A. S. Zibrov, P. R. Hemmer, H. Park, and M. D. Lukin. Generation of single optical plasmons in metallic nanowires coupled to quantum dots. *Nature*, 450:402, 2007.

[111] R. Kolesov, B. Grotz, G. Balasubramanian, R. J. Stör, A. A. L. Nicolet, P. R. Hemmer, F. Jelezko, and J. Wrachtrup. Wave-particle duality of single surface plasmon polaritons. *Nat. Phys.*, 5:470, 2009.

[112] T. van der Sar, E. C. Heeres, G. M. Dmochowski, G. de Lange, L. Robledo, T. H. Oosterkamp, and R. Hanson. Nanopositioning of a diamond nanocrystal containing a single nitrogen-vacancy defect center. *Appl. Phys. Lett.*, 94:173104, 2009.

[113] S. Schietinger, M. Barth, T. Aichele, and O. Benson. Plasmon-enhanced single photon emission from a nanoassembled metal-diamond hybrid structure at room temperature. *Nano Lett.*, 9(4):1694, 2009.

[114] A. Huck, S. Kumar, A. Shakoor, and U. L. Andersen. Controlled coupling of a single nitrogen-vacancy center to a silver nanowire. *Phys. Rev. Lett.*, 106:096801, 2011.

[115] J. Michaelis, C. Hettich, J. Mlynek, and V. Sandoghdar. Optical microscopy using a single-molecule light source. *Nature*, 405:325, 2000.

[116] M. Frimmer, Y. Chen, and A. F. Koenderink. Scanning emitter lifetime imaging microscopy for spontaneous emission control. *Phys. Rev. Lett.*, 107:123602, 2011.

[117] A. Cuche, O. Mollet, A. Drezet, and S. Huant. Deterministic quantum plasmonics. *Nano Lett.*, 10:4566, 2010.

[118] N. Chevalier, M. J. Nasse, J. C. Woehl, P. Reiss, J. Bleuse, f. Chandezon, and S. Huant. CdSe single-nanoparticle based active tips for near-field optical microscopy. *Nanotechnology*, 16:613, 2005.

[119] L. Aigouy, Y. De Wilde, and M. Mortier. Local optical imaging of nanoholes using a single fluorescent rare-earth-doped glass particle as a probe. *Appl. Phys. Lett.*, 83:147, 2003.

[120] D. V. Isakov, Y. Zhang, L. J. Balk, and J. C. H. Phang. Optical near-field probe with embedded gallium scattering centre. *Appl. Phys. Lett.*, 94:253108, 2009.

[121] Invitrogen Life Technologies.

[122] E. Dulkeith, A. C. Morteani, T. Niedereichholz, T. A. Klar, J. Feldmann, S. A. Levi, F. C. J. M. van Veggel, D. N. Reinhoudt, M. Möller, and D. I. Gittins. Fluorescence quenching of dye molecules near gold nanoparticles: Radiative and nonradiative effects. *Phys. Rev. Lett.*, 89:20, 2002.

[123] S. Kühn, G. Mori, M. Agio, and V. Sandoghdar. Modification of single molecule fluorescence close to a nanostructure: Radiation pattern, spontaneous emission and quenching. *Mol. Phys.*, 106(7):893, 2008.

[124] W. Lukosz and R. E. Kunz. Light emission by magnetic and electric dipoles close to a plane interface. I. total radiated power. *J. Opt. Soc. Am.*, 67(12):1607, 1977.

[125] W. Lukosz and R. E. Kunz. Light emission by magnetic and electric dipoles close to a plane dielectric interface. II. radiation patterns of perpendicular orientated dipoles. *J. Opt. Soc. Am.*, 67(12):1615, 1977.

[126] K. G. Lee, X. W. Chen, H. Eghlidi, P. Kukura, R. Lettow, A. Renn, V. Sandoghdar, and S. Götzinger. A planar dielectric antenna for directional single-photon emission and near-unity collection efficiency. *Nat. Photonics*, 5:166, 2011.

[127] O. Lecarme, T. Pinedo-Rivera, K. Berton, J. Berthier, and D. Peyrade. Plasmonic coupling in nondipolar gold colloidal dimers. *Appl. Phys. Lett.*, 98:083122, 2011.

[128] U. Håkanson, M. Agio, S. Kühn, L. Rogobete, T. Kalkbrenner, and V. Sandoghdar. Coupling of plasmonic nanoparticles to their environments in the context of van der Waals-Casimir interactions. *Phys. Rev. B*, 77:155408, 2008.

[129] C. E. Talley, J. B. Jackson, C. Oubre, N. K. Grady, C. W. Hollars, S. M. Lane, T. R. Huser, P. Nordlander, and N. J. Halas. Surface-enhanced Raman scattering from individual Au nanoparticles and nanoparticle dimer substrates. *Nano Lett.*, 5(8):1569, 2005.

[130] T. Atay, J.-H. Song, and A. V. Nurmikko. Strongly interacting plasmon nanoparticle pairs: From dipole-dipole interaction to conductively coupled regime. *Nano Lett.*, 4(9):1627, 2004.

[131] L. Chuntonov and G. Haran. Trimeric plasmonic molecules: The role of symmetry. *Nano Lett.*, 11:2440, 2011.

[132] K. Li, M. I. Stockman, and D. J. Bergman. Self-similar chain of metal nanospheres as an efficient nanolens. *Phys. Rev. Lett.*, 91(22):227402, 2003.

[133] N. Yamamoto, S. Ohtani, and F. J. García de Abajo. Gap and mie plasmons in individual silver nanospheres near a silver surface. *Nano Lett.*, 11:91, 2011.

[134] S. V. Boriskina and B. M. Reinhard. Spectrally and spatially configurable superlenses for optoplasmonic nanocircuits. *P. Natl. Acad. Sci. USA*, 108(8):3147, 2011.

[135] F. M. Huang, D. Wilding, J. D. Speed, A. E. Russell, P. N. Bartlett, and J. J. Baumberg. Dressing plasmons in particle-in-cavity architectures. *Nano Lett.*, 11(3):1221, 2011.

[136] H. J. Lezec, A. Degiron, E. Devaux, R. A. Linke, L. Martin-Moreno, F. J. Garcia-Vidal, and T. W. Ebbesen. Beaming light from a subwavelength aperture. *Science*, 297:820, 2002.

[137] K. Imura, K. Ueno, H. Misawa, and H. Okamoto. Anomalous light transmission from plasmonic-capped nanoapertures. *Nano Lett.*, 11:960, 2011.

[138] T. W. Ebbesen, H. J. Lezec, H. F. Ghaemi, T. Thio, and P. A. Wolff. Extraordinary optical transmission through sub-wavelength hole arrays. *Nature*, 391:667, 1998.

[139] C. Genet and T. W. Ebbesen. Light in tiny holes. *Nature*, 445:39, 2007.

[140] R. Gordon. Bethe's aperture theory for arrays. *Phys. Rev. A*, 76:053806, 2007.

[141] F. J. García de Abajo, R. Gómez-Medina, and J. J. Sáenz. Full transmission through perfect-conductor subwavelength hole arrays. *Phys. Rev. E*, 72:016608, 2005.

[142] H. J. Lezec and T. Thio. Diffracted evanescent wave model for enhanced and suppressed optical transmission through subwavelength hole arrays. *Opt. Express*, 12(16):3629, 2004.

[143] M. Beruete, M. Sorolla, I. Campillo, J. S. Dolado, L. Martín-Moreno, J. Bravo-Abad, and F. J. García-Vidal. Enhanced millimeter-wave transmission through subwavelength hole arrays. *Opt. Lett.*, 29(21):2500, 2004.

[144] Y. Pang, A. N. Hone, P.P.M. So, and R. Gordon. Total optical transmission through a small hole in a metal waveguide screen. *Opt. Express*, 17(6):4433, 2009.

[145] F. Medina, F. Mesa, and R. Marqués. Extraordinary transmission through arrays of electrically small holes from a circuit theory perspective. *IEEE T. Microw. Theory*, 56(12):3108, 2008.

[146] N. Engheta, A. Salandrino, and A. Alù. Circuit elements at optical frequencies: Nanoinductors, nanocapacitors and nanoresistors. *Phys. Rev. Lett.*, 95:095504, 2005.

[147] M. G. Silveirinha, A. Alù, J. Li, and N. Engheta. Nanoinsulators and nanoconnectors for optical circuits. *J. Appl. Phys*, 103:064305, 2008.

[148] D. M. Pozar. *Microwave Engineering*. Wiley: Hoboken, NJ, 2004.

[149] R. J. Black and L. Gagnon. *Optical Waveguide Modes*. Mc Graw Hill, 2010.

[150] F. Medina, J. A. Ruiz-Cruz, F. Mesa, J. M. Rebollar, J. R. Montejo-Garai, and R. Marqués. Experimental verification of extraordinary transmission without surface plasmons. *Appl. Phys. Lett.*, 95:071102, 2009.

[151] J. H. Kang, J.-H. Choe, D. S. Kim, and Q.-H. Park. Substrate effect on aperture resonances in a thin metal film. *Opt. Express*, 17(18):15652, 2009.

[152] E. ul Haq, Z. Liu, Y. Zhang, S. A. Alang Ahmad, L.-S. Wong, S. P. Armes, J. K. Hobbs, G. J. Leggett, J. Micklefield, C. J. Roberts, and J. M. R. Weaver. Parallel scanning near-field photolithography: The Snomipede. *Nano Lett.*, 10(11):43754380, 2010.

[153] R. Bachelot, C. Ecoffet, D. Deloeil, P. Royer, and D.-J. Lougnot. Integration of micrometer-sized polymer elements at the end of optical fibers by free-radical photopolymerization. *Appl. Optics*, 40(32):5860, 2001.

[154] G. A. Valaskovic, M. Holton, and G. H. Morrison. Parameter control, characterization, and optimization in the fabrication of optical fiber near-field probes. *Applied Optics*, 34(7):1215, 1995.

[155] B. Hecht, B. Sick, U. P. Wild, V. Deckert, R. Zenobi, O. J. F. Martin, and D. W. Pohl. Scanning near-field optical microscopy with aperture probes: Fundamentals and applications. *J. Chem. Phys*, 112(18):7761–7774, 2000.

[156] M. Stähelin, M. A. Bopp, G. Tarrach, A. J. Meixner, and Zschokke-Gränacher. Temperature profile of fiber tips used in scanning near-field optical microscopy. *Appl. Phys. Lett.*, 68(19):2603, 1996.

[157] D. I. Kavaldjiev, R. Toledo-Crow, and M. Vaez-Iravani. On the heating of the fiber tip in a near-field scanning optical microscope. *Appl. Phys. Lett.*, 67(19):2771, 1995.

[158] A. H. La Rosa, B. I. Yakobson, and H. D. Hallen. Origins and effects of thermal processes on near-field optical probes. *Appl. Phys. Lett.*, 67(18):2597, 1995.

[159] F. Renna, D. Cox, and G. Brambilla. Efficient sub-wavelength light confinement using surface plasmon polaritons in tapered fibers. *Opt. Express*, 17(9):7658, 2009.

[160] Y. Avlasevich, S. Müller, P. Erk, and K. Müller. Novel core-expanded Rylenebis(Dicarboximide) dyes bearing Pentacene units: Facile synthesis and photophysical properties. *Chem.-Eur. J.*, 13:6555–6561, 2007.

[161] A. Degiron, H.J. Lezec, N. Yamamoto, and T. W. Ebbesen. Optical transmission properties of a single subwavelength aperture in a real metal. *Opt. Commun.*, 239:61–66, 2004.

[162] L. Neumann, Y. Pang, A. Houyou, M. L. Juan, R. Gordon, and N. F. van Hulst. Extraordinary optical transmission brightens near-field fiber probe. *Nano Lett.*, 11:355–360, 2011.

[163] C. Manzo, T. S. van Zanten, and M. F. Garcia-Parajo. Nanoscale fluorescence correlation spectroscopy on intact living cell membranes with nsom probes. *Biophys. J.*, 100(2):L8, 2011.

[164] J. Renger, R. Quidant, N. van Hulst, and L. Novotny. Surface-enhanced nonlinear four-wave-mixing. *Phys. Rev. Lett.*, 104:046803, 2010.

[165] J. C. Johnson, H. Yan, R. D. Schaller, P. B. Petersen, P. Yang, and R. J. Saykally. Near-field imaging of nonlinear optical mixing in single zinc oxide nanowires. *Nano Lett.*, 2(4):279, 2002.

[166] Sánchez E. J., L. Novotny, and X. S. Xie. Near-field fluorescence microscopy based on two-photon excitation with metal tips. *Phys. Rev. Lett.*, 82(20):4014, 1999.

[167] K. Imura and H. Okamoto. Properties of photoluminescence from single gold nanorods induced by near-field two-photon excitation. *J. Phys. Chem. C*, 113:11756, 2009.

[168] P. Vasa, C. Ropers, R. Pomraenke, and C. Lienau. Ultra-fast nano-optics. *Laser Photonics Rev.*, 3:483–507, 2009.

Acknowledgements

There goes the shawl again.
L. Carroll

This work would have been entirely impossible without the people whose names should but hardly ever appear on a publication. I am very grateful for the support and advice of Luis Enrique, Javier Pérez at ICFO and María Jesús López Bosque at the Parc Científic de Barcelona. Without you, antennas would have simply stayed a beautiful flash of wit. I am equally thankful to Núria Segú, Carlos Dengra and Jonas Padonou for their rapid problem-solving.

There is no research without paperwork. I would like to extend my gratitude to Mery del Mar Gil, Manuela Furkert, Cristina García, Anne Gstöttner and Laia Miralles for their support and patience.

I want to express my appreciation and gratitude to Niek F. van Hulst whose never-ending support and devotion made this thesis possible.

Other tremendous sources of support I would like to mention are Dominique Heinis, Martin Kuttge, Florian Kulzer, Daan Brinks, Thomas van Zanten at ICFO, and Frans Segerink and Jeroen Korterik the University of Twente. Jorick van't Oever's help on the set-up is not to be underestimated. Advising three students from three countries at three different stages in their careers has been a great learning experience. I would like to thank Sabine Auer, Amel Houyou and Jorick van't Oever for their dedication and support and I hope I have been a good adviser to them during this time.

It has been a pleasure exchanging ideas and thoughts on joint projects with Reuven Gordon and Yuanjie Pang at the University of Victoria and Mathieu L. Juan, Frank Koppens, Guenevere Prawiroatmodjo and Michela Badioli at ICFO. I am also indebted to Trifon Trifonov of CRNE, and Jordi Llobet and Xavier Borrise of IMB–CNM.

It was amazing to see ICFO grow during the past years. I thank Lluis Torner for his support and the extra-curricular opportunities to grow and learn.

Many others have contributed to thesis at various stages. I am more than grateful to Srdjan Aćimović, Nicolò Accanto, Yolanda Atienza García, Gaëtan Calbris, André Eckardt, Marta Castro López, Fabio Gatti, Simó Graells i Castellà; Richard Hildner, Jakob Hoogenboom, Danny Krautz,

Mark Kreuzer, Pavan Kumar, Aude Lereu, Carlo Manzo, Luis Martínez Montblanch, Jana Nieder, Armand Niederberger, Johann Osmond, Satish Rao, Pablo Manuel de Roque, Riccardo Sapienza, Anshuman Singh, Fabian Steinlechner, Stephan Teichmann, Klaas-Jan Tielrooij, Koen Thuijs, and Giorgio Volpe.

Last but not least, I like to mention the whole of the ICFO community.